

Spectroelectrochemical study of biomolecules in artificial membrane systems

Vorgelegt von
M.Sc. Biomedizin
Barbara Daiana Gonzalez
Geb. in Buenos Aires, Argentinien

von der Fakultät II – Mathematik und Naturwissenschaften
der Technischen Universität Berlin
zur Erlangung des akademischen Grades

Doktor der Naturwissenschaften
Dr. rer. nat.
genehmigte Dissertation

Promotionsausschuss:

Vorsitzender: Prof. Dr. Nediljko budisa

Berichter: Prof. Dr. Peter Hildebrandt

Berichter: Prof. Dr. Inez Weidinger

Tag der wissenschaftlichen Aussprache: 28.09.2017

Berlin 2018

Abstract

This work presents a spectroelectrochemical approach combining electrochemical impedance spectroscopy (EIS) and surface-enhanced infrared absorption (SEIRA) spectroscopy to characterise the interaction of proteins and peptides with model membranes. The artificial membrane systems are assembled on a nanostructured Au-film, which is deposited on an attenuated total reflectance (ATR) crystal as a prerequisite for the enhancement of the IR signals of the immobilised molecules. The Au-film also serves as working electrode to control and vary the potential across the immobilised membrane model. Here, a nanodisc system was employed to investigate the membrane protein channelrhodopsin II (ChR II), while tethered bilayer lipid membrane (tBLM) systems were used to characterise the antimicrobial peptides enniatin B (EB) and arenicin 1 (A1).

For the first time, the light-induced structural changes of the "slow" C128S mutant of the light-gated ion channel ChR II embedded into nanodisc systems were observed by SEIRA spectroscopy. The nanodisc systems containing zwitterionic lipids and His-tag tails were successfully immobilised using the Ni-NTA (nitrilotriacetic acid) monolayer. The spectral changes were assigned to structural variations of the protein backbone associated to the transition from the dark state to the P390 intermediate. This proof-of-principle study demonstrates that nanodisc represent a promising system to study the retinal protein ChR II.

Characterisation of EB peptide by SEIRA spectroscopy was performed using a 1-Palmitoyl-2-oleoyl-sn-glycero-3-phosphocholine (POPC, zwitterionic lipids) tBLM system. The unprecedented results, provide a comprehensive evaluation of EB incorporation in membrane systems in the presence of monovalent cations, as well as a new understanding of EB:ion complex formation. The spectral features of EB ligand groups in presence of K^+ ion, demonstrated that the K^+ complex significantly differs from the species formed in the presence of Na^+ and Cs^+ ions, which are spectroscopically alike. These findings disagree with previous studies, and contribute to the controversial discussion of EB:ion complex stoichiometry assignment.

Finally, tBLMs containing 1-palmitoyl-2-oleoyl-sn-glycero-3-[phospho-rac-(1-glycerol)] (sodium salt) (POPG) negatively charged lipids were employed for characterising the membrane binding of the cationic peptide A1. The unique structure of A1 and its potential-dependent activity were investigated by SEIRA spectroscopy. The β -sheet folding exhibited high stability in different environments (solid, solution and membrane) and temperatures. The highest activity was recorded at 37° C upon application of negative potentials (-400 mV). Overall, A1 significantly disturbed the lipid membrane in a non-reversible manner.

The EIS and SEIRA spectroscopy results were complemented with UV-vis, ATR-IR, FT-IR transmission spectroscopy, as well as theoretical calculations, allowing a sound structure-function insight. The high reproducibility and stability of the membrane systems, together with the specific results for the target biomolecules, have shown that EIS and SEIRA spectroscopy are powerful tools for the structural and functional study of biomolecules and their interaction with model membranes.

Zusammenfassung

Die vorliegende Arbeit beschreibt einen spektro-elektrochemischen Ansatz, in welchem elektrochemische Impedanzspektroskopie (EIS) und oberflächenverstärkte Infrarotabsorptions-Spektroskopie (*surface-enhanced infrared absorption*, SEIRA) zur Charakterisierung der Interaktion zwischen Proteinen und Peptiden mit Model-Membranen kombiniert wurden. Die künstlichen Membransysteme wurden auf einen nanostrukturierten Au-Film adsorbiert, der auf einem Abgeschwächte Totalreflexion (*attenuated total reflectance*) ATR-Kristall als Voraussetzung für die Verstärkung des Infrarotsignals der immobilisierten Moleküle aufgebracht wurde. Die Au-Schicht dient ebenso als Arbeitselektrode und erlaubt die Kontrolle und Veränderung des Potentials an der immobilisierten Membran. Im Rahmen dieser Arbeit wurde ein Nanodisc-System zur Untersuchung des Membranproteins Kanalrhodopsins II (ChR II) genutzt, während zur Analyse der antimikrobiellen Peptide Enniatin B (EB) und Arenicin 1 (A1) Oberflächen-adsorbierte Lipiddoppelschichtmembransysteme (*tethered bilayer lipid membrane*, tBLM) verwendet wurden.

Die licht-induzierten strukturellen Änderungen der „langsamen“ C128S-Mutante des licht-gesteuerten Ionenkanals ChR II eingebettet in einem Nanodisc-System wurden zum ersten Mal mit SEIRA-Spektroskopie gezeigt. Das Nanodisc-System, bestehend aus zwitterionischen Lipiden, wurde mit einem terminalen His-Tag erfolgreich an eine Nickel-Nitrilotriessigsäure-Monolage (Nit-NTA) immobilisiert. Die spektralen Änderungen ordneten man der strukturellen Unterschiede des Proteinrückrats zu. Diese erfolgen beim Übergang des Dunkelzustandes zum P390 Intermediat. Hierbei wurde gezeigt, das Nanodiscs ein vielversprechendes System zur Untersuchung des Retinalproteins ChR II sind.

Charakterisierung des EB Peptids mittels SEIRA Spektroskopie erfolgte unter der Verwendung von einem 1-Palmitoyl-2-oleoyl-sn-glycero-3-phosphocholine (POPC, zwitterionische Lipide) tBLM System. Die neuartige Erkenntnisse bieten eine umfassende Auswertung des EB Einbaues in Membran-Systeme bei der Anwesenheit von monovalenten Kationen sowie der EB:Ion-Komplexbildung. Die spektralen Merkmale der EB-Ligandengruppen in Anwesenheit eines K⁺-Ion zeigten, dass der K⁺-Komplex Unterschiede im Gegensatz zur Na⁺- und Cs⁺-Spezies aufweist. Diese Ergebnisse widersprechen vorherige Untersuchungen, dadurch tragen sie zur kontroversen Diskussion der stöchiometrischen Zuordnung des EB:Ion-Komplexes.

Abschließend wurden tBLM-Systeme, bestehend aus 1-palmitoyl-2-oleoyl-sn-glycero-3-[phospho-rac-(1-glycerol)] (POPG als Natriumsalz) negativ geladenen Lipide, zur Untersuchung des kationischen Peptids A1 eingesetzt. Die einzigartige A1 Peptidstruktur und deren Potential-Abhängigkeit wurden mittels SEIRA-Spektroskopie untersucht. Die β -Faltblattstruktur zeigte hohe Stabilität in verschiedenen Umgebungen (fester Zustand, Lösung und Membran) und Temperaturen. Die höchste Aktivität wurde bei 37 °C und einem negativen Potential (-400 mV) nachgewiesen. Insgesamt wurde eine irreversible Störung der Membran beobachtet.

Die Ergebnisse der EIS und SEIRA spektroskopischen Untersuchungen wurden mit UV-VIS, ATR-IR und FT-IR Transmission, sowie theoretischen Berechnungen ergänzt, dadurch wurde einen aussagekräftigen Einblick der Struktur-Funktion-Beziehung erreicht. Die gute Reproduzierbarkeit der Experimente und Stabilität des Membransystems haben zusammen mit den getroffenen Aussagen zu den untersuchten Molekülen bewiesen, dass EIS und SEIRA Spektroskopie aussagekräftige Werkzeuge zur strukturellen und funktionellen Betrachtung der Wechselwirkung von Biomolekülen mit Model-Membranen darstellen.

Poster contributions

1. Antimicrobial peptides, Gordon research conference, May 3rd – 8th 2015. Lucca (Italy), *Spectroelectrochemical study of the antimicrobial peptide enniatin B*.
2. School of analytical sciences Adlershof poster session, November 2015. Berlin (Germany), *Spectroelectrochemical study of the antimicrobial peptide enniatin B*. Awarded best poster design.
3. AMP2016-International symposium on antimicrobial peptides, June 6th – 8th 2016. Montpellier (France), *Spectroelectrochemical study of the antimicrobial peptide enniatin B*.
4. IMAP-6th International meeting on antimicrobial peptides, August 31st – September 3rd. Leipzig (Germany), *Structural study of the antimicrobial peptide enniatin B in a biomimetic bilayer membrane system*.

Table of content

Abstract	3
Zusammenfassung	4
Poster contributions.....	5
Table of content	7
Abbreviations	11
1. Motivation	13
2. Introduction.....	17
2.1. Artificial membrane systems.....	17
2.1.1. Cell membranes and artificial membranes.....	17
2.1.1.1. Phospholipids	18
2.1.2. Nanodisc membrane systems	20
2.1.3. Tethered bilayer lipid membrane systems	21
2.2. Membrane proteins	22
2.2.1. Infrared spectroscopy of proteins	24
2.2.2. Channelrhopsin II membrane protein.....	27
2.3. Antimicrobial peptides	29
2.3.1. Enniatin B	32
2.3.2. Arenicin 1	34
2.4. Theory of vibrational spectroscopy	36
2.4.1. Basics of vibrational spectroscopy	37
2.4.1.1. Molecular vibrations and the harmonic oscillator.....	37
2.4.1.2. Normal modes	39
2.4.2. Infrared absorption spectroscopy	41
2.4.3. Fourier transform IR	42
2.4.4. Attenuated total reflectance IR	44
2.4.5. Surface-enhanced IR absorption SEIRA spectroscopy	45
2.5. Theory of electrochemical impedance spectroscopy	47
2.5.1. Basic theory of the electrical impedance	47
2.5.2. Graphical representation of impedance data	49

2.5.3. Graphical evaluation and physical relevance in tBLM systems.....	50
3. Experimental section	52
3.1. Materials	52
3.2. Sample preparation.....	53
3.2.Methods.....	54
4. Results	60
4.1. Channelrhodopsin II in nanodisc systems	60
4.1.1. UV-vis study of ChR II protein	61
4.1.2. FT-IR transmission study of ChR II protein	65
4.1.2.1. Illumination cycles of ChR II protein	66
4.1.3. Spectroelectrochemical study of Ni-NTA monolayers	68
4.1.4. SEIRA study of the ChR II C128S protein in nanodisc systems.....	73
4.1.5 Conclusions	75
4.2. Characterisation study of enniatin B	76
4.2.1. Incorporation of enniatin B into tBLM system	77
4.2.1.1. EIS of POPC membrane systems	77
4.2.1.2. SEIRA spectroscopy of POPC membrane systems	81
4.2.1.3. Membrane incorporation of enniatin B.....	84
4.2.2. Structural study of enniatin B ion complexes in membrane systems	88
4.2.2.1. Enniatin B ion-exchange in membrane systems	88
4.2.2.2. IR spectroscopy of enniatin B	91
4.2.2.3. Theoretical calculations of enniatin B ion complexes	94
4.2.3. Mechanism of membrane incorporation and ion binding	99
4.2.4. Conclusions	104
4.3. Antimicrobial peptide arenicin I	105
4.3.1. IR and Raman spectroscopy of arenicin I	105
4.3.1.1. ATR-IR spectroscopy of solid arenicin I	106
4.3.1.2. FT-Raman spectroscopy of solid arenicin I	108
4.3.1.3. FT-IR transmission of arenicin I in solution	109
4.3.2. SEIRA and EIS study of the POPC/POPG membrane systems	111
4.3.3. Peptide-membrane interaction study by SEIRA	113

4.3.3.1. Arenicin1 interaction with POPC/POPG tHLM system.	113
4.3.3.2. SEIRA spectroscopy of arenicin1 interaction with POPC/POPG tBLM system: temperature dependence	114
4.3.4. Molecular dynamics simulation of arenicin1	117
4.3.5. Conclusions.	120
5. Conclusions	122
Outlook.....	124
Bibliography.....	126
Acknowledgements	138
Appendix	141

Abbreviations

1PrOH	1-Propanol
6MH	6-Mercaptohexanol
A1	Arenicin 1
ACN	Acetonitrile
AMPs	Antimicrobial peptides
ATR	Attenuated total reflectance
Arg	Arginine
BTP	Bis-Tris propane
ChR II	Channelrhodopsin II
ChRs	Channelrhodopsins
CPE	Constant phase element
CsCl	Cesium chloride
Cys	Cysteine
D-Hiv	D-hydroxyisovaleric acid
DMPC	1,2-dimyristoyl-sn-glycero-3-phosphocholine
EB	Enniatin B
EIS	Electrochemical impedance spectroscopy
EM	Electromagnetic
FT	Fourier transform
FT-IR	Fourier transform infrared
HCl	Hydrogen chloride
IR	Infrared
KCl	Potassium chloride
NaCl	Sodium chloride
POPC	1-Palmitoyl-2-oleyl-sn -glycero-3-phosphocholine
POPG	1-palmitoyl-2-oleoyl-sn-glycero-3-phospho-(1'-rac-glycerol) (sodium salt)
SAM	Self-assembled monolayer
SEIRA	Surface-enhanced IR absorption
tBLM	Tethered bilayer lipid membrane
Trp	Tryptophan
Tyr	Tyrosine
Val	N-methyl-L-valine amino acid
WK3SH	Dihydrocholesteryl (2-(2-(2-ethoxy)ethoxy)ethanethiol
UV-vis	Ultraviolet-visible

1. Motivation

The main motivation for this thesis is the increasing demand for a better understanding of the interaction of biomolecules with the cell envelope, and in particular with the plasmatic membrane. This membrane is comprised of lipids, complex proteins and other molecules that contribute to form a barrier for the cell. In this membrane an astonishing number of reactions take place, namely signalling, molecule and cell recognition, chemical reactions, transport, in addition to many others. A characteristic of the cell membrane is that it is considered the first contact-site and entrance for many pathogenic agents. An example is in the symbiotic relationship¹ that multicellular organisms share with microbiota, where a deregulation of the homeostasis of this ecosystem leads to dysfunction or disease in the host organism [1]. The capability of evolution and adaptation of the microbiota is the challenge and motivation for science to constantly innovate techniques to investigate the relationship between biomolecules and membranes. The design of mimetic membrane systems applied to membrane-interacting molecules has been and still is an evolving field, which is of great relevance in the study of physiological disorders and drug mechanisms of action.

With the aim of studying membrane-related processes, the three targets used in this work are chosen based on their implication in novel research fields, such as optogenetics and antimicrobial peptides (AMPs). The membrane proteins channelrhodopsins are microbial rhodopsins that govern the phototaxis of the green algae *Chlamydomonas reinhardtii*, acting as light-sensitive ion-channels. Several studies of wild-type and mutant proteins have shown the possibility of controlling the open and close state of the channel by light. This fact gave rise to the development of the optogenetic techniques, which mainly use Channelrhodopsin II (ChR II) in neural cells studies [2]. On the other hand, the discovery of AMPs in the beginning of the 20th century offered new directions in the development of drugs. The potential of AMPs to target a wide range of diseases, from bacterial and fungi infections to viral, parasitic and cancer disorders, aims to overcome the increasing resistance and adaptation of bacteria to conventional antibiotics. In the context of this work, there is a special interest in membrane-active AMPs, in their structural features and mechanism of action. The cyclic enniatin B (mainly from *Fusarium scripi* fungi) and the distinctive arenicin 1 (from lugworm *Arenicola marina*) AMPs present interesting structural characteristics, which are in the focus of controversial discussions. Even though nowadays, more than thousands of AMPs have been isolated or synthesised, there is a great opportunity for the development of advanced methods offering more detailed information about their selectivity and interaction with membranes.

¹ The microbiota in multicellular organisms is composed mainly of commensal bacteria that do not cause harmful effect to the host.

To date, there are several techniques used in life science that can provide detailed chemical information of biomolecules. However, most of them present restrictions in size, purity or form (solid, crystalline, etc.) of the sample. Vibrational spectroscopy is one of the techniques that have evolved significantly to overcome these drawbacks. The advances in application of non-invasive techniques like Raman and infrared (IR) spectroscopy, allows scientists to investigate building blocks of biomolecules like complex proteins or peptides, as well as the composition of the cell membrane. Due to innovations in IR techniques, the characterisation of many macromolecules in solution, and also solid state was possible. Yet, membrane proteins and related processes represent a challenge for structural and functional analysis, since they demand a membrane environment to avoid denaturation. Membrane-mimetic systems like micelles, vesicles and solid supported bilayers are used to overcome these problems. Albeit to date, most of the membrane-mimetic systems are applied to electrochemical or imaging techniques, the discovery of the surface-enhanced IR absorption (SEIRA) effect increased significantly the sensitivity for structural studies of biological systems, especially those using membrane systems. SEIRA spectroscopy exploits the properties of functionalised nanostructured noble metals, i.e. Au, which amplifies the signal and at the same time, acts as an electrode for electrochemical analysis. In this way, SEIRA is a powerful tool for the study of membrane proteins or peptides in a native-like environment by using supported membrane systems linked to the metal surface. The surface-proximity restriction in SEIRA (short-range enhancement), allows detecting processes close to the surface minimizing the interferences from the bulk solution.

In this work, the main goal is to employ planar and nanodisc membrane systems in an spectroelectrochemical approach combining SEIRA and electrochemical impedance spectroscopy (EIS) for the structural study of the targets mentioned above. The use of EIS allows estimating the quality of the monolayers and membrane-mimetic systems. The challenge of this combined method lies mainly in the development of a stable, robust and reproducible system. In this approach there are many parameters to control simultaneously: membrane fluidity, optimal environment for stability and function of targets (concentration, ionic strength, pH), monolayer ratio for membrane systems, among others. In some cases, an initial optimisation stage was performed to determine the optimal balance between detection of the target spectroscopic features and membrane stability. Whereas the lipids used in this study stand for a small portion of the diverse cell membrane composition, the presented membrane systems serve as a starting point for optimisation towards a more representative membrane mimic.

The first part in this work offers an introduction to the methods and targets, as well as to the theory behind the applied techniques. The results are presented in three sections, one for each target and the corresponding membrane system, which were all investigated by SEIRA and EIS spectroscopy. A nanodisc system is used in the study of a slow mutant of the light-sensitive membrane protein ChR II. A zwitterionic planar membrane system serves as platform for the characterisation of the cyclic enniatin B peptide and its ion complexes. A negatively charged planar membrane system is

applied in the investigation of arenicin 1 peptide and its disturbance of the membrane. A number of vibrational spectroscopic techniques such as IR transmission and UV-vis, together with preliminary theoretical calculations are used to validate or complement the results obtained from the spectroelectrochemical approach. At the end, the final conclusions are presented along with an outlook for each project.

2. Introduction

This section situates the reader into context, for a better understanding of the work presented in this dissertation. The introduction to the systems and targets used in this work, in addition to theoretical background set the basis for comprehension and discussion of the results.

2.1. Artificial membrane systems

The following subsections offer an introduction to cell membranes and its diverse composition, as well as to artificial membrane systems. A description of the phospholipids used in this study, is essential to understand the structures they can adopt and their fascinating behaviour. These fundamentals are basic to get familiar with the two membrane systems introduced at the end of the section.

2.1.1. Cell membranes and artificial membranes

Lipid membranes are essential for the architecture, organization and function of living cells. The cell membrane is involved in processes like signal transduction, electrochemical gradients or ligand-receptor interactions. The composition of cell membranes varies with the type of cell, containing structures from small molecules to complex macrostructures like protein aggregates. In the so called "tree of life" cells are classified into three kingdoms by their evolution in respect with a common progenitor, which allows distinguishing cells organizational levels. The architecture and composition of the cell envelope can differ not only between, but also within the archaebacteria, eubacteria and eukaryotes kingdoms. A classic example is the difference between plants and animals in the eukaryotic group; plant cells have a cell wall layer outside the plasma membrane, while the principal barrier to the environment in the case of animal cells is the plasma membrane [3]. Besides the differences, all cell envelopes have in common that they act as a fort for the cell with communication lines between the external and internal content. Therefore, artificial membrane systems play a key role in the study of membrane interaction with its components and external agents [3] [4]. The characterization of plasma membranes as mainly composed by proteins and phospholipids arranged in bilayer motifs [5], is in constant update with new distinct membrane domains, like lipid rafts in bacteria membranes recently described by Nickels and coworkers [6].

The involvement of membrane domains in numerous mechanisms of disease, and the demanding requirements for the stabilization of its components, have pushed the field of biophysics to develop biomimetic models to study their structure and function.

Artificial membrane systems have evolved significantly since the “fluid mosaic model” (also known as painted membrane) developed by Mueller and coworkers in the early ‘60s of last century [7]. Nowadays, there is a wide range of constructs of diverse complexity and application, going from vesicles and micelles to supported bilayers and nanodiscs [8] [9] [10] [11] [12]. The development of these systems has allowed investigating not only cell membrane assemblies and lipid composition, but also characterizing structure and function of peptides and membrane proteins [13] [14]. This kind of study is especially relevant for membrane proteins, which require a native-like environment for proper conformation and function, as well as for other membrane-related processes. In several cases, membrane components have been used as pharmacological targets for the treatment of various diseases and disorders [15]. The versatile characteristics of supported artificial membrane systems permit its combination with an extensive number of techniques, including vibrational spectroscopy [16] [17]. The work presented here focuses on two models, nanodisc and tethered bilayer lipid membrane (tBLM) systems.

2.1.1.1. Phospholipids

The main lipids in plasma membranes are the phospholipids. The phospholipid structure can be divided into three parts: a hydrophobic tail, a connecting backbone, and a polar head group (see figure 2.1). The medium part has an important effect for the organization of lipids. They form mesophases in aqueous solution by self-assembling in a variety of structures like micelles, bilayers or hexagonal phases, which can be explained by their amphiphilic character [18]. The mobility of lipids depends on their shape, and more importantly on the solid-crystalline phase transition. In biological membranes lipids are found in the crystalline (also called liquid) phase, where lipids have freedom to move. The phase transition or melting temperature (T_m) between the gel and fluid phase is determined by the structure of the lipid. The longer the acyl chain of the lipid the higher the T_m , while a higher degree of unsaturation of the bonds leads to lower T_m [19]. The transfer of molecules through the dynamic assembly of fluid bilayer is highly selective. While water can travel relatively fast ($30\text{--}40\text{ }\mu\text{ms}^{-1}$), the membrane is impermeable to ions like Na^+ or K^+ . Nonetheless, the permeability is influenced by membrane components such as channel proteins or cholesterol molecules. It has been suggested that cholesterol molecules increase the conformational order of the membrane at temperatures above the lipids T_m [20].

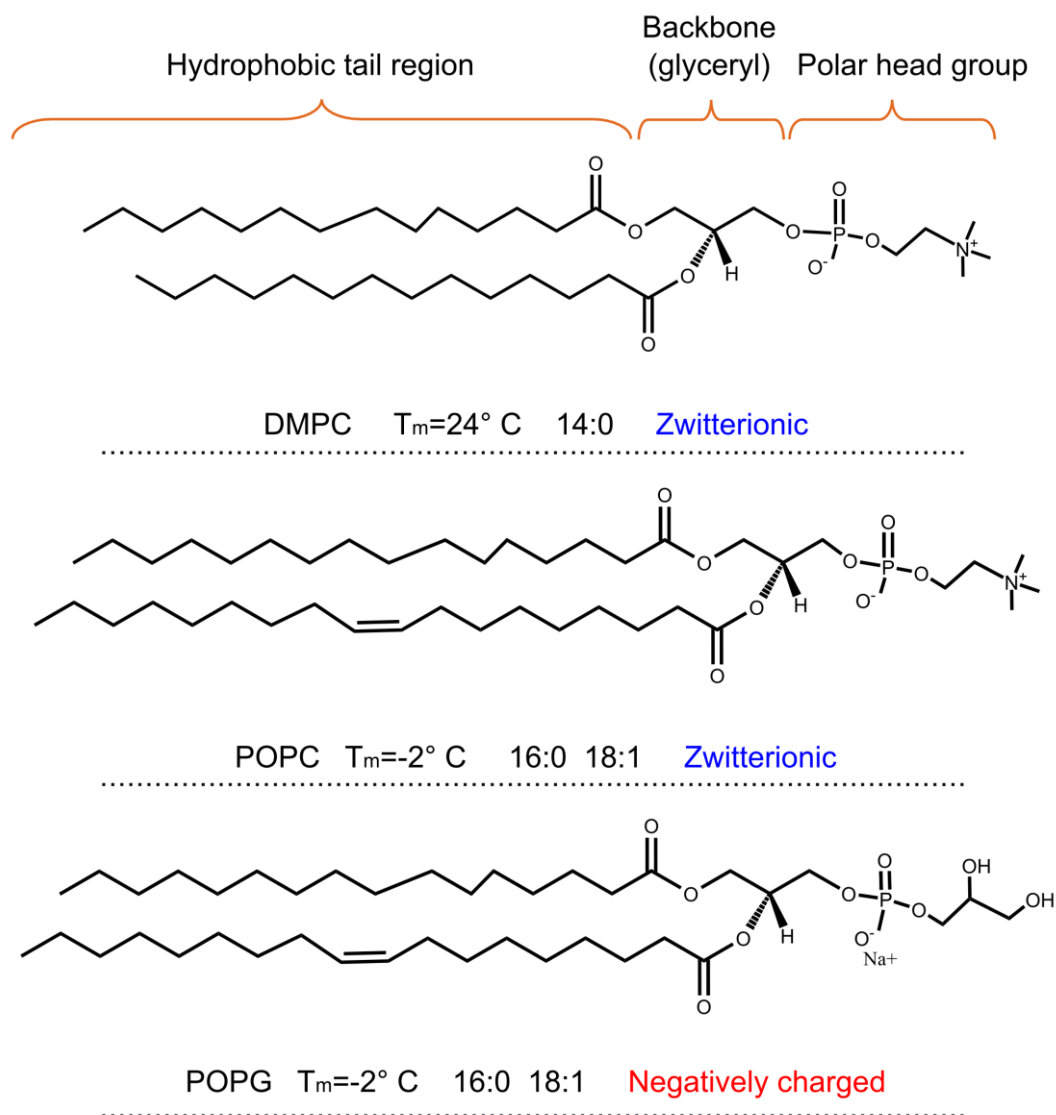


Figure 2.1. Structure of the phospholipids used in this work: DMPC, POPC and POPG. The three parts that define the name of the phospholipid are indicated on the top of the figure. Below each phospholipid there is the respective phase transition temperature (T_m). The unsaturated degree and length of the acyl chains are indicated as n° of carbon atoms:n° of double bonds for each chain, so that 18:1 denotes 18 carbon atoms and one double bond. Additionally, the corresponding charge at neutral pH of the headgroup is shown below each phospholipid.

Phospholipids are named following the designation for their three components. This work describes the construction of membrane systems using the lipids 1,2-Dimyristoyl-sn-glycero-3-phosphocholine (DMPC), 1-Palmitoyl-2-oleoyl-sn-glycero-3-phosphocholine (POPC) and 1-palmitoyl-2-oleoyl-sn-glycero-3-[phospho-rac-(1-glycerol)] (sodium salt) (POPG), as depicted in figure 2.1. The analysis of lipids by infrared (IR) spectroscopy allows identifying the functional groups of the different phospholipids [8] (normal mode theory, *vide infra*). The normal modes of the (CH₂) groups of the acyl chains offer information about the organization of lipids in the bilayer. These modes correspond to the symmetric and asymmetric stretching of (C-H), scissoring, wagging, twisting and

rocking. While the stretching modes are related to the physical state and hydration of the lipids, the deformation modes in addition to the phase-dependence, give information about the organization and interaction of the acyl chains [8] [19]. The stretching modes of the (CH₂) and (CH₃) groups from the lipids are intense in the IR spectrum between 3050 and 2800 cm⁻¹. The carbonyl vibrational modes (C=O) appear between 1800 and 1700 cm⁻¹. The phosphate group in the lipid headgroup contributes to the IR spectrum as well, with the asymmetric and symmetric stretching of the (R-O-P-O-R') modes below 1300 cm⁻¹ [8] [19] [21].

2.1.2. Nanodisc membrane systems

In 2002, Sligar and coworkers introduced a novel membrane system of 10-20 nm in diameter, composed by patches of lipid bilayers encircled by an amphiphilic membrane scaffold protein (MSP) that avoids the spontaneous formation of vesicles [10]. There have been advances in the construction of such models, improving the control in size, composition and functional modifications [22]. Nanodisc systems are used as water-soluble nanocarriers for membrane proteins, providing a native-like environment [12]. The advantage of this kind of model is that the scaffold protein can be modified by a His-tag, allowing a proper immobilization on a metal surface for spectroscopic analysis, while the target protein remains in its natural form (see figure 2.2). In this case, a Ni-NTA (Nickel-nitrilotriacetic acid) monolayer was used as a linker to anchor the nanodisc via the MSP His-tag to a Gold film (Au-film). This monolayer works in

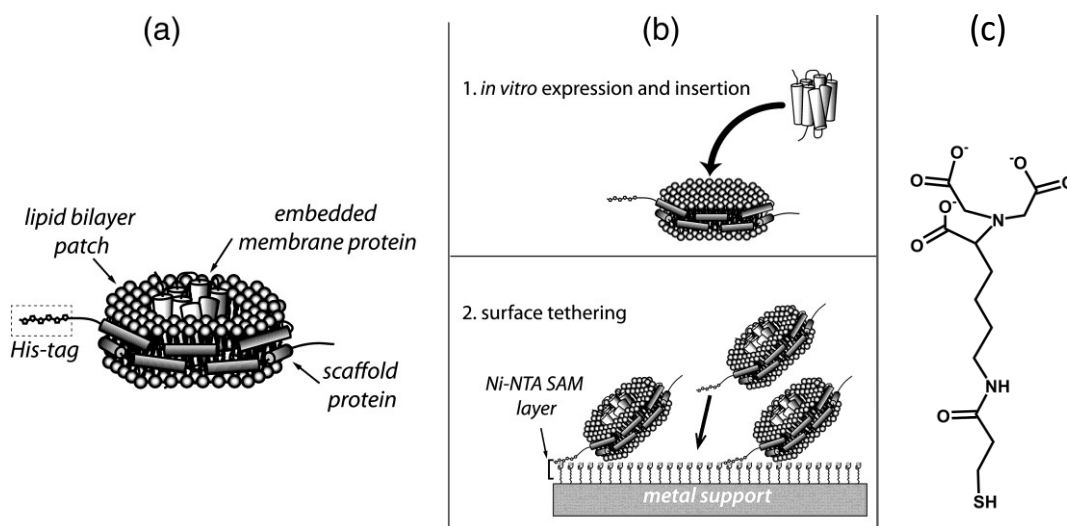


Figure 2.2. Schematic representation of Membrane protein embedded in a nanodisc composed of lipid bilayer and membrane scaffold protein (a). (b) The membrane protein folds into the nanodisc during or after in-vitro expression. Then, the protein/nanodisc is tethered to the Ni-NTA SAM modified surface via the His-tag at the terminus of the scaffold protein. (Reprinted from *Biochimica et Biophysica Acta (BBA)-Biomembranes*, 1828 (10), K. Ataka, *Surface-enhanced infrared absorption spectroscopy (SEIRAS) to probe monolayers of membrane proteins*, 2283-2293, Copyright (2013), with kind permission from Elsevier) [12]. (C) Molecular structure of the NTA molecule used as SAM to functionalise the Au-film.

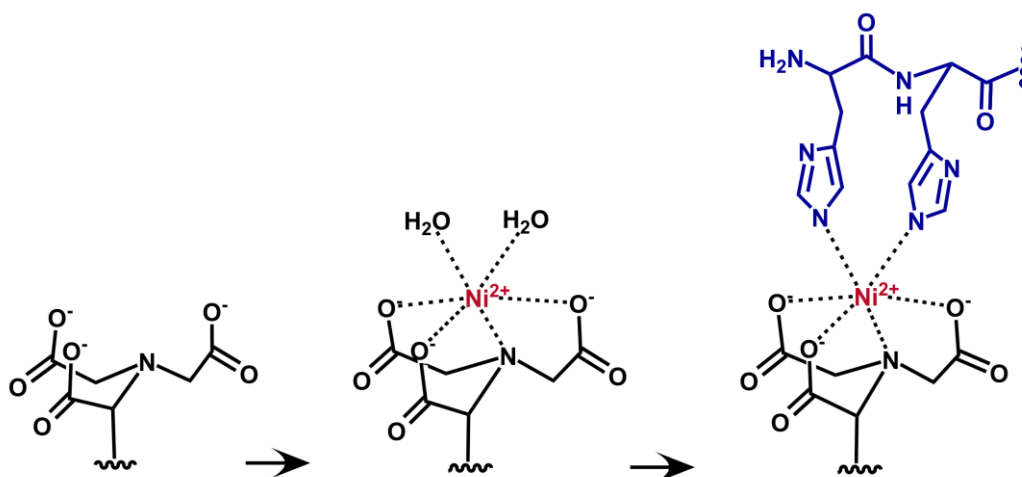


Figure 2.3. Schematic representation of the chelating reaction of the Ni^{2+} ion with NTA molecule and His residues. For matter of simplification, only the head group of NTA is shown in the figure. When Ni^{2+} ion is added to the solution onto the immobilised NTA molecules, it adopts an octahedral coordination geometry. In this first step, NTA carboxylate groups and nitrogen atom occupy four of the six free-spaces of Ni^{2+} ion coordination sphere, leaving the last two to water molecules. The latter are replaced by the imidazole group of His residues when the nanodisc with His-tagged tail is added. Thus, each Ni^{2+} ion acts as a bridge between one NTA molecule and two His residues.

such a way that first, the NTA monolayer is assembled onto the Au-film, followed by the chelation of Ni^{2+} ions by the three carboxylate groups of the NTA molecule (see figure 2.3). The Ni^{2+} ions serve as linkers between the NTA and His residues of the MSP to anchor the nanodisc system. Some of the benefits that nanodisc systems offer compared to other lipid systems are the MSPs, which avoids fusion and controls the size of the assemblies enhancing the stability and solubility in aqueous solution of the nanodisc with the integrated membrane protein [22] [23].

The nanodisc system used in this project was composed of DMPC lipids and MSP1E3D1 as scaffold protein, for the study of the microbial membrane protein channelrhodopsin isoform II (ChR II). Studies of a variety of membrane targets using nanodisc systems combined to different techniques prove the nanodisc versatility and stability. Some examples are the applications in NMR [24] [25], chromatography [26], surface plasmon resonance (SPR) [27] [28] and surface enhanced IR absorption (SEIRA) [14] spectroscopy. Therefore, this is a promising mimetic membrane system for membrane process investigation.

2.1.3. Tethered bilayer lipid membrane systems

Tethered bilayer lipid membrane (tBLM) systems are planar solid-supported constructs that allow anchoring the membrane to a functionalized electrode, a Au-film in this case. This membrane system presents the advantage that it can be built with tethered lipids (see figure 2.4). The tBLM used in this study requires three components and a

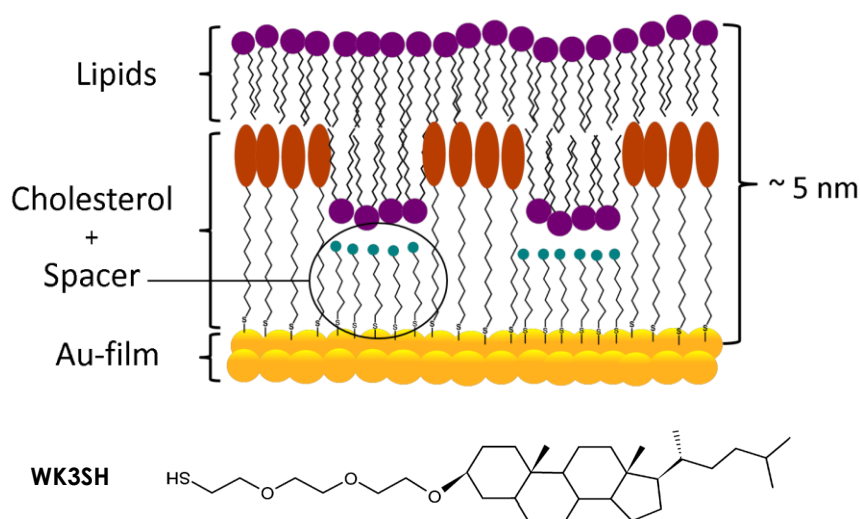


Figure 2.4. Scheme of a tBLM system used in SEIRA spectroscopy. The nanostructured Au-film is functionalized with a mixed SAM that forms islands of WK3SH cholesterol and of 6MH spacer molecules. The phospholipid molecules complete the system by forming areas of lipid bilayer on top of the aqueous reservoir created by 6MH. The thickness of the system is ca. 5 nm. Below, there is the structure of the WK3SH tethered-molecule [29].

two-step process. First, clusters of a hydrophobic part such as cholesterol tethered molecules and of a hydrophilic part are absorbed to form a mixed self-assembled monolayer (SAM) on the Au-film. The hydrophilic part creates an aqueous reservoir between the electrode and the lipid bilayer. Subsequently, lipid vesicles are added, which spontaneously cover the SAM surface forming islands of bilayer lipid membranes [9] [29]. The phase separation of the SAM molecules is the reason for the formation of the lipid bilayer islands. Once the tBLM is stabilized, the system is ready for the study. The molecules that form such a construct should be chosen and tested for each system in order to obtain the conditions that fit best to the target. This project uses WK3SH (synthesized by Wiebalck et al. [29]) as cholesterol tethered molecule, 6-mercaptohexanol (6MH) as spacer, and POPC and POPG for the lipid bilayer.

The WK3SH tethered molecule offers the important advantage of being IR-transparent in the amide region of the spectra ($1800\text{--}1500\text{ cm}^{-1}$), in comparison to other tethered molecules that often interfere with the target biomolecule [29]. The benefits of tBLM systems are the water reservoir beneath the lipids providing a native-like environment, and the wide range of applications in the study of peptides, membrane proteins and ligands [11] [13] [30].

2.2. Membrane proteins

Proteins are biopolymers (macromolecules) composed by a sequence of amino acids, where monomers are linked to each other by a peptide bond (amide bond). In a

peptide bond, a carboxyl group (C=O) of one amino acid is linked to the amino group (N-H) of the succeeding amino acid releasing a water molecule. There are four structure-organizational levels in proteins. The primary structure of a protein is represented by the amino acid sequence, starting from the amino end (N-terminal) to the carboxyl end (C-terminal) [3]. The interactions between amino acids within the protein determine the secondary structure, resulting in a three-dimensional (3D) assembly. The most common secondary structures are α -helix and β -sheet, random coil and turn. The α -helix is a right-handed spiral with a distance of 0.15 nm between two adjacent amino acids, a turn angle of 100° with respect to the centre and with 3.6 amino acids per turn [31]. β -sheets are formed by at least two strands of the polypeptide arranged into pleats. The strands can have a parallel or antiparallel orientation to each other and are connected by inter-strand hydrogen bonds [3]. Proteins may assemble into tertiary structures containing more than one secondary structure (same kind or different) interconnected to each other. In many cases, proteins are organised in aggregates of multiple subunits (homo or heterodimers), which define the quaternary structure. As in secondary and tertiary structures, also in the quaternary arrangement the stabilisation depends on the interaction between the side-chain of amino acids. Some of these interactions may include hydrogen bonds, disulphide-bridges and salt bridges [3] [12].

The adopted secondary structure can determine the family or type, and consequently, the function of a protein. Membrane proteins include a wide array of protein families involved in cellular processes, i.e. metabolites and ion transport (see figure 2.5), cell signalling, ATP synthesis, and many others [22]. Channel proteins are an important kind of membrane proteins, which are responsible for ion-trafficking between the intra- and extracellular medium. The main function of ion channel proteins is gating the ion

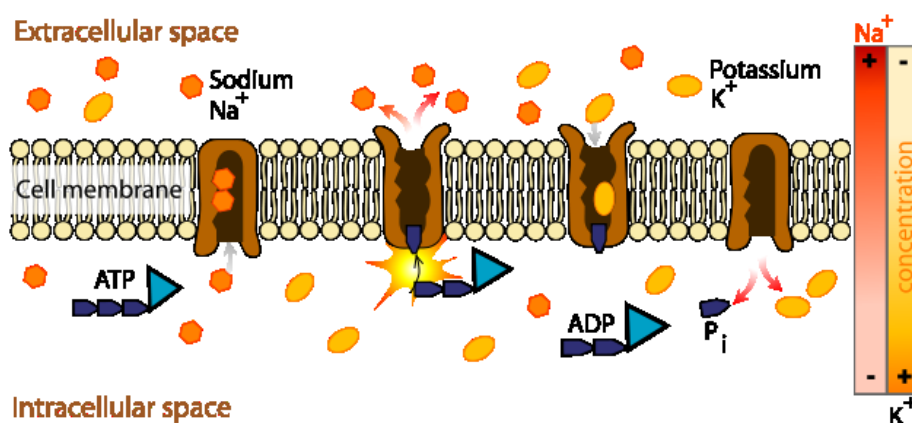


Figure 2.5. The function of the sodium-potassium pump is an example of primary active transport. The two carrier proteins on the left are using ATP (adenosine triphosphate) to move sodium out of the cell against the concentration gradient. The proteins on the right are using secondary active transport to move potassium into the cell. Energy from hydrolysis of ATP is directly coupled to the movement of a specific substance across a membrane independent of any other species. On the right side, the concentration gradients of Na⁺ and K⁺ between the extracellular and intracellular spaces are indicated. (Scheme adapted from *Membrane transport proteins*, Mariana Ruiz Villarreal (2007). With kind permission of Wikimedia Commons). [32].

conductance for signal transduction processes [32]. Depending on the way these proteins are activated they are divided into three classes: ligand-gated channels, voltage-gated channels or mechanosensitive channels [33]. A distinguished and relatively new class are channelrhodopsins, which are microbial membrane proteins that work as light-gated ion channels [33] [34] (*vide infra*).

In this context, the structural study of membrane proteins helps characterising them, offering information about the interactions that make their 3D folding possible. For membrane proteins, a lipid or membrane-like environment is key for its assembly and function [12] [35]. In most cases, these proteins lack the activity without the membrane. This is the main reason why membrane proteins are highly difficult to investigate in solution without a proper native surrounding, and why artificial membrane systems are essential for their study.

2.2.1. Infrared spectroscopy of proteins

The molecular vibrations of the backbone motif of proteins can be characterise by IR spectroscopy. One of the advantages of the technique is that it provides a distinctive signal for the different functional groups. In that way, the vibration of the two main groups in the protein would result in characteristic bands in the IR spectrum. In the secondary structure of proteins, the periodicity of the backbone results in an addition of the representative amide modes (figure 2.6) [36] [37]. The important amide band appearing in IR spectra are amide I and amide II (description below). However, it is also possible to identify characteristic vibrational modes from amino acid side chains, as in the case of tyrosine (Tyr) or tryptophan (Trp) [38] [39]. The analysis of the amide I and II modes, as well as the modes of the amino acid side chains, considering hydrogen bonding and the coupling of the transition dipole moments, can be used for the prediction of the polypeptide structure [39]. The following descriptions of the polypeptide vibrations are based on the work from Krimm and Bandekar (1986) [36] and Barth (2007) [39].

NH stretching (3300 and 3070 cm^{-1}). This mode, also known as amide A, is localised in the NH group and it remains unaffected by the conformation of the polypeptide. It is the first component of the Fermi resonance with first overtone of the amide II in helices. The second component is named amide B, and it is observed as a weak absorption in the region between 3100 to 3050 cm^{-1} .

Amide I (ca. 1650 cm^{-1}). The major contribution to this mode corresponds to the (C=O) stretching (76%), including minor contributions of the out-of-plane CN stretching, (CNN) deformation, and (NH) in-plane bending (responsible for N-deuteration of the backbone) [19]. Since the amide I mode depends on the secondary structure of the protein backbone and is not significantly affected by the side chains, it is one of the most relevant vibrations for structure prediction.

Amide II (ca. 1550 cm^{-1}). This mode is the out-of-phase combination of the in-plane (NH) bending (43%) and the (CN) stretching (14%), with small contribution from the in-plane bending from (CO) (11%), (CC) stretching (9%), and (NC) stretching (8%) [19]. This mode has been less investigated than the amide I.

Amide III (1400-1200 cm^{-1}). This mode is a in-phase combination of the (CN) stretching (66%) and the out-of-plane (NH) bending (34%) [19]. It is sensitive to the side chain structure and it frequently overlaps with other modes between 1400 and 1200 cm^{-1} . In some cases, it can as well contribute to predict the secondary structure of the polypeptide.

One important fact for the study of biomolecules in aqueous solution by IR spectroscopy, is the interference of the broad (OH) bending mode (ca. 1645 cm^{-1}) of water with the amide I and II region [37] [21]. One way to overcome the overlapping of the OH band is using heavy water (D_2O) solutions, which leads to a downshift of the bending mode to ca. 1210 cm^{-1} [19]. Nevertheless, in some cases, performing IR

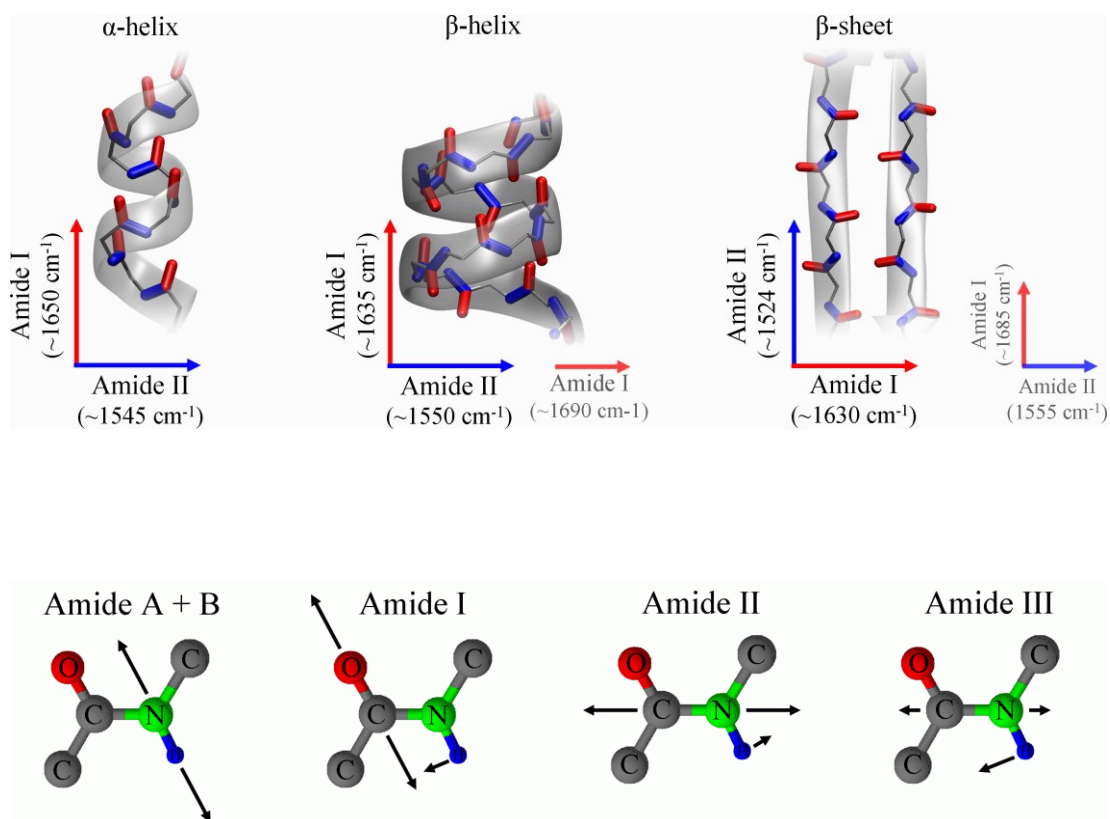


Figure 2.6. Top: α -helix (left), β -helix (middle), and β -sheet (right) with C=O and C-N bondings highlighted in red and blue, respectively. Due to the periodical alignment of these bonds, the total dipole moments of the amide I and amide II of these secondary structure elements are oriented perpendicular to each other as indicated by the arrows. Below: Schematic representation of the vibrational modes of biomolecules. Bottom: Protein backbone (amide) modes. (Adapted with kind permission from Jacek Kozuch (2013), *Structure-Function Relationships of Membrane Proteins - Spectroelectrochemical Investigation of Artificial Membranes*, Technische Universität Berlin, Fakultät II [21].

difference spectroscopy, where the background is subtracted from the protein spectrum, can reduce the contribution of water.

2.2.2. Channelrhodopsin II membrane protein

Channelrhodopsin II (ChR II) membrane protein is a microbial type Rhodopsin that operates as a light-sensitive ion channel. Ion-channel proteins act as gates for ions in the cell membrane. Their function is important since, as other transporters, they regulate the traffic of ions between the inside and outside medium. There is a wide range of processes where ion channel proteins are involved triggering the electrical signal transduction, like it is the case of ChR II [40]. Channelrhodopsins (ChRs) are integral proteins, with seven transmembrane α -helices (see representation in figure 2.7) [41]. ChR I and ChR II proteins were the first ones discovered in the green algae *Chlamydomonas reinhardtii*. Both variants are responsible for the algae's phototaxis, each responding to different light intensity. Nowadays, thirteen ChRs from different algae have been isolated. Upon illumination, ChR II produces an increase of the conductance of monovalent and divalent ions causing the depolarisation of the cell membrane within milliseconds [40] [42]. The channel is highly selective to protons, up to 10^6 times compared to monovalent cations, and it does not diffuse anions [40]. Investigations of the photocurrents of the channel of ChR II suggest a pore diameter of ca. 6.2 Å, where cations travel predominantly in their dehydrated form [43]. The photoisomerisation from all-*trans* to 13-*cis* (C13=C14) of the retinal chromophore covalently bonded to L257 (Lysine in 257 position) forming a protonated Schiff base, induces the opening (or closing) of the channel by conformational and electrostatic changes in the ChR II (retinal isomers shown in figure 2.8) [44]. This means that opening and closure of this kind of ion channels can be controlled by light, which is an exceptional characteristic. Optogenetics techniques, which mainly use ChR II variant, take advantage of this unique feature to control neural circuits with light [45] [46].

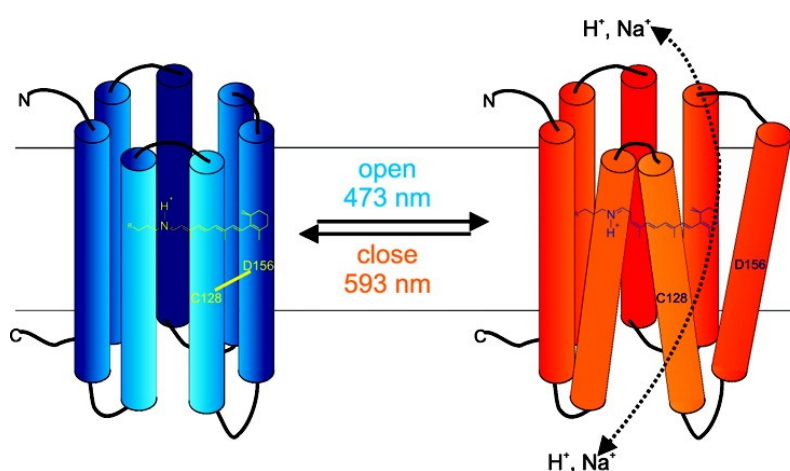


Figure 2.7. Schematic representation of the light-gated ion channel channelrhodopsin II, and its seven transmembrane helices. The hydrogen bond interaction between C128 and D156 is indicated connecting transmembrane helices 3 and 4. The inset shows the environment around the retinal binding pocket. The photoisomerisation of the retinal and consequent open and close reaction are depicted as well. (Reprinted from *Biochemistry*, 49, Bamann C. et al. *Structural guidance of the photocycle of channelrhodopsin-2 by an interhelical bond*, 267-278, Copyright (2009), with kind permission from American Chemical Society) [41].

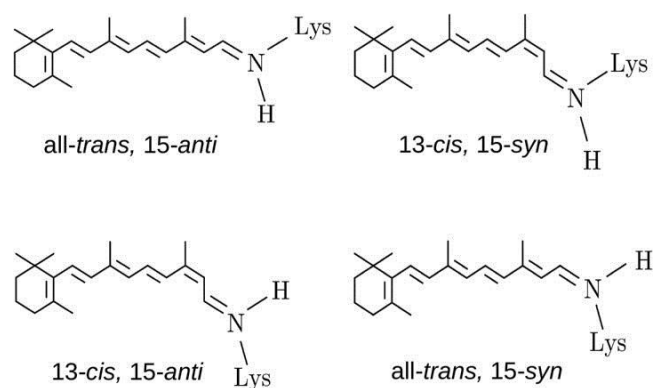


Figure 2.8. Retinal isomers of retinal proteins. In the bacteriorhodopsin dark-adapted state, either all-trans, 15-anti or 13-cis, 15-syn retinal is observed, whereas 13-cis, 15-anti retinal occurs in the M intermediate structure. In bovine rhodopsin, the switch between all-trans, 15-anti and all-trans, 15-syn is capable to switch between the active form and its thermal predecessor. In the case of ChR II, the predominant transitions are between all-trans, 15-anti (dark state) and 13-cis, 15-anti (conductive state). (Adapted and reprinted from The Journal Of Biological Chemistry, 288(15), Ritter E. et al. *Light-Dark Adaptation of Channelrhodopsin C128T Mutant*, 10451–10458, Copyright (2013), with kind permission from The American Society for Biochemistry and Molecular Biology, Inc) [34].

There have been several attempts to describe the structural changes of the transitions involved in the light-cycle of ChR II, however, certain transition states are elusive to detection due to the fast equilibrium between them. After photo-activation the protein runs through intermediate states that eventually result in the relaxation of the system to the dark state. Certain changes during these processes like protein conformation, retinal interactions and protonation states can be observed by vibrational spectroscopy [40]. The main features of the photocycle of ChR II are the activation of the conductance of the channel and the closing induced by blue and green light, respectively. With the objective to slow down the cycle, different mutants were produced for characterisation based on its analogy to the well-known bacteriorhodopsin. In that way, the mutation in the position C128 (Cysteine 128 position) of the ChR II sequence can extend the open state life-time of the channel up to seconds or even minutes (preferably substitutions with Threonine, T; Arginine, A; or Serine, S) [34] [44] [47] [48]. In this work, the C128S variant incorporated in nanodiscs was studied by vibrational spectroscopy. According to Berndt and co-workers, his C128S mutant displays the longest extension of the conducting state lifetime with 106 s versus 11.9 ms for the wild type, and a significant increase of the protein sensitivity to light [48]. These facts make this mutant (C128S) an interesting target to evaluate the application of nanodisc membrane systems for the study of light-sensitive membrane proteins.

2.3. Antimicrobial peptides

Peptides are biomolecules of shorter amino acid chain length than proteins, which as well can adopt secondary structures. In nature, peptides have a wide range of functions participating in cells communication, defence, repairing and death [3].

Antimicrobial peptides (AMPs) are those peptides that are implicated in the cell or organisms defence mechanism. Therefore, the production of AMPs is one of the processes through which cells protect and/or respond to foreign agents and changes in the environment. Ageitos et al. (2016) offered a vast review of the diverse natural sources of AMPs and some synthetic variants [49]. The activity spectrum of AMPs is constantly increasing, with targets like parasites, bacteria, viruses and cancer cells [31]. There are peptides of different length, structure, species and mode of action. Their importance has been rising because of their application as antibiotics substitutes to overcome resistance. The first AMP discovered was gramicidin in 1939, isolated from a *Bacillus* strain and effective against *pneumococci* infection [50]. The first AMP from animal source was defensin from rabbit leukocytes, in 1956 [51]. Tyrothricin is the first AMP for clinical use in humans (1939), composed of a mixture of tyrocidins and gramicidin D produced by *Bacillus brevis* (Gram-positive aerobic spore-forming bacteria) [52]. This discovery paved the way for AMPs to clinical use, and after more than 60 years in use it has shown no microbial resistance [53].

The evolution of certain AMPs across the kingdoms of the phylogenetic tree has shown that peptides from the same family have evolved depending on the environment of the species producing them [54]. Controversial, but yet attractive examples are defensins, for which the origin of this kind of peptides could be traced to a common ancestor of 0.5 billion years old [54]. There are cationic peptides (mostly antibacterial) [55], anionic AMPs, host defense peptides [56], α -helical antimicrobial peptides, and many more that raise the number of discovered and synthesized AMPs to more than 5000 [57]. Due to the diversity in nature, structure and function (activity) of AMPs there is a lack of a normalized classification of these peptides. However, for the benefit of the studies presented in this work, the discussion is reduced to two classifications: by structural features and by activity or mechanism of action.

From the structural point of view, α -helix and β -sheet conformations (see section 2.2. for structural characteristics) are the most common and studied ones, while extended, loop and circular structures are found in fewer cases [31]. As explained for proteins, each assembly has structural features that are possible to assess by IR spectroscopy. In some cases, the amino acid composition may influence the secondary structure of the peptide. It has been suggested that there are certain amino acids that are important for the AMP structural stability and/or activity, i.e. Zou et al. (2007) suggested that the activity of the α -defensin-1 is significantly reduced with the substitution of arginine (Arg) residues for lysines (Lys) [58]. Additionally, the positive net charge of cationic AMPs is essential for the interaction with the negatively charged membrane of bacteria. Some

AMPs may adopt more than one of these motifs, or there are peptides that present one structure in solution and a different one in contact with certain compounds, surfaces or the cell membrane, like the peptide indolicidin [59]. An interesting and less studied group of AMPs are the circular ionophores such as valinomycin, beauvericin and enniatins [60]. The ring structure of enniatin peptides allows them to induce ion-transport through the target membrane, which as well as for valinomycin and beauvericin is believed to be their mode of action [61].

Another way to classify AMPs is by their activity or mechanism of action (see figure 2.9). They have shown antiviral, antibacterial (mostly cationic AMPs), antifungal (mainly polar and neutral amino acids), antiparasitic or anticarcinogenic activity [62]. However, the mechanisms of action may differ from interacting with the pathogen or with the host, modifying the host environment, membrane or gene expression [54]. In this investigation the focus is mainly on membrane-active AMPs. The different lipid environments in microorganisms may be one of the important factors that determine the membrane-binding of AMPs [4]. Most of these peptides are amphipathic, containing both hydrophilic and hydrophobic parts. In the same way as for membrane proteins, the hydrophobic character allows the peptides to interact with the aliphatic chains and allocate within the lipid bilayer. On the contrary, the ionic properties allow interacting with the negatively charged head groups of some lipids, POPG for instance, and/or with the aqueous medium in and outside the membrane [62]. Currently, a few models have been described for membrane active peptides: carpet, aggregate, and barrel-stave are some of the examples shown in figure 2.9. One of the most common mechanisms of action is the pore formation followed by the permeabilization and disruption of the membrane, like it has been suggested for one of the targets of this thesis arenicin isoform 1 (A1) [63]. The amphipathic character of A1 and its net charge of +6, explains the attraction to negatively charged lipids and the damage of the membrane [64]. In general, factors like charge, amphipathicity, hydrophobicity and H-bonding interactions are of important consideration for mechanism of action estimation [65].

Gram-positive and Gram-negative bacteria are the most studied targets of AMPs. Therefore, it is important to briefly describe their envelope composition based mainly on the study offered by Malanovic and Lohner (2015) (see figure 2.10) [4]. The classification into these two groups originates from the staining result of the bacteria cells, which is either positive, if the cells take the stain (purple colour) or negative, if they cannot. Both variants present a plasma lipid bilayer membrane composed of a combination of zwitterionic (higher percentage in Gram-positive) and negatively charged phospholipids (higher percentage in Gram-negative), followed by a stabilising layer of peptidoglycan (PGN). The thickness of the PGN layer is significantly higher for Gram-positive (ca. 40-80 nm) in comparison to the thin layer of Gram-negative (ca. 8 nm). Gram-negative bacteria present an outer lipid bilayer membrane, where the inner layer is mainly composed of phospholipids and the outer layer of lipopolysaccharides (LPS). The cell envelopes of these bacteria are represented in

figure 2.10. This figure also shows the membrane and cell wall of fungi, which is another relevant target of AMPs. The interaction and role of the components of the bacterial envelopes is an open and on-going discussion in the AMP community.

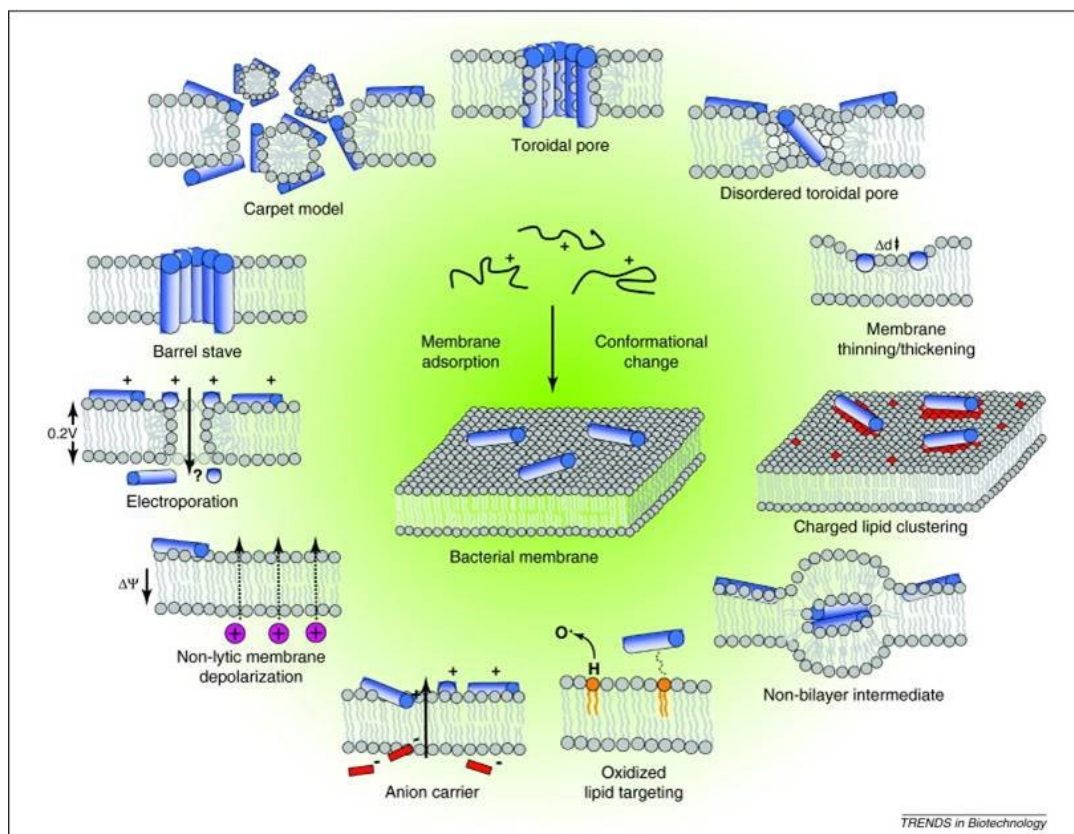


Figure 2.9. Events occurring at the bacterial cytoplasmic membrane following initial antimicrobial peptide (AMP) adsorption. These events are not necessarily exclusive of each other. In the classical models of membrane disruption, the peptides lying on the membrane reach a threshold concentration and insert themselves across the membrane to form either peptide-lined pores in the barrel-stave model, solubilize the membrane into micellar structures in the carpet model, or form peptide-and-lipid-lined pores in the toroidal pore model. In the revised disordered toroidal pore model, pore formation is more stochastic and involves fewer peptides. The thickness of the bilayer can be affected by the presence of the peptides, or the membrane itself can be remodelled to form domains rich in anionic lipids surrounding the peptides. In more specific cases, non-bilayer intermediates in the membrane can be induced; peptide adsorption to the membrane can be enhanced by targeting them to oxidized phospholipids; a peptide may couple with small anions across the bilayer, resulting in their efflux; the membrane potential can be dissipated without other noticeable damage; or conversely, in the molecular electroporation model, the accumulation of peptide on the outer leaflet increases the membrane potential above a threshold that renders the membrane transiently permeable to various molecules including the peptides themselves. (Adapted and reprinted from Trends in Biotechnology, 29 (9), L. T. Nguyen et al. *The expanding scope of antimicrobial peptide structures and their modes of action*, 464-472, Copyright (2011), with kind permission from Elsevier) [62].

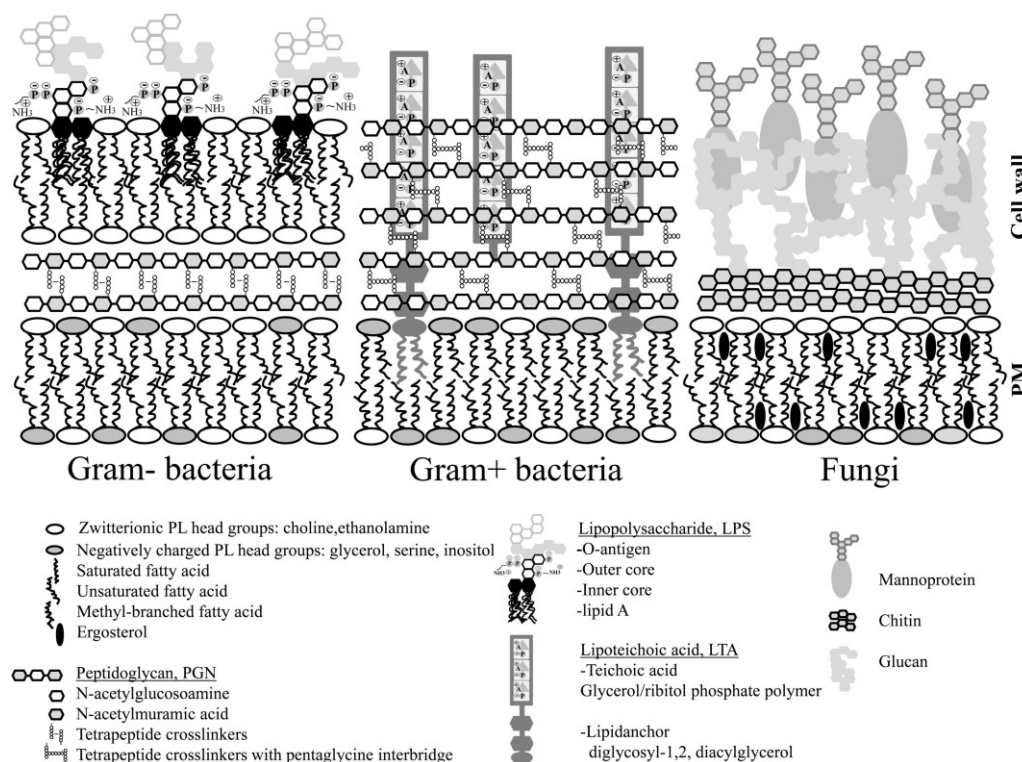


Figure 2.10. Cell envelopes of various microbial families. (Adapted and reprinted from Biochimica et Biophysica Acta (BBA)-Biomembranes, 1858, N. Malanovic and K. Lohner, *Gram-positive bacterial cell envelopes: The impact on the activity of antimicrobial peptides*, 936-946, Copyright (2015), with kind permission from Elsevier) [4].

2.3.1. Enniatin B

For decades, natural and synthetic analogues of enniatins have been studied for their antimicrobial applications. The attractivity of this family of non-ribosomal peptides lies in their structure, which is achieved by alternating D-hydroxy acids and N-methyl-L-amino acids (valine, leucine and isoleucine more common ones), forming a six unit ring. Enniatins are toxins produced by various species of *Fusarium* fungi, and they belong to the group of cyclohexadepsipeptides [61]. The particular N-methylation of the L-amino acid takes place in the module 2 of the enniatin synthetase (ESyn) enzyme, previous to the final cyclization of the peptide [66]. Gaumann et al. (1947) reported the discovery of the first enniatin, enniatin A, found in the fungus *Fusarium orthoceras* var. *enniatinum*, active against bacteria, fungi and plant shoot [67]. Nowadays, there exist approximately 29 variants, plus many others that have been biosynthesized to investigate biochemical applications. The most common ones are enniatin A, A₁, B and B₁. They act against Gram-positive (thick peptidoglycan layer, but without outer membrane) and Gram-negative (with outer membrane and thinner peptidoglycan layer) bacteria, fungi and cancer cells [68]. Laboratories Servier (French company) developed the first drug with enniatins mixture from *Fusarium lateritium* WR as active

agent named fusafungine for oral or nasal administration, which presents antimicrobial activity against numerous microorganisms that cause respiratory infections like the Gram-positive *Staphylococcus aureus* [69] (out-of-market since 03.2016).

Enniatins function as neutral ionophores (ion-carrier without ionisable groups) complexing ions and transporting them through the cell membrane [60]. This means that the “ion” is transported from the extracellular medium-lipid interface, through the membrane, and to the lipid-intracellular medium interface. Therefore, the concentrations of the “ion” at each side of the membrane have a great impact in the equilibrium of the reactions taking place [60]. Their high hydrophobic character makes them membrane-active peptides, considered to be the mechanism of action for enniatins [61]. Enniatin B (EB) variant is produced mainly by the *Fusarium scirpi* fungi. It is composed by *N*-methyl-*L*-valine (Val) amino acid combined with the *D*-hydroxyisovaleric acid (*D*-Hiv) (see figure 2.11). This peptide presents similarities of structure and function with the well-known depsipeptides beauvericin, which contains aromatic *N*-methyl amino acids, and valinomycin, which is twice the size of EB and alternates *L*- and *D*- enantiomers of valine residues with *D*-Hiv and *L*-lactic acid. Enniatins cannot fold into a 3D structure due to the dimension of the ring, but it can form complexes of different stoichiometry (1:1, 2:1 or 3:2, EB:cation) with alkali, earth-alkali and some transition metals in order to induce the ion-transport through the membrane [61] (see figure 2.12). EB variant has shown potential antimicrobial [70], antifungal [71], and anticarcinogenic [72] [73] activity, and against the malaria parasite [70], which makes it an attractive target for the study of peptide-membrane interaction. Besides the lipophilic character of EB, it has also shown to inhibit enzymatic function of calcium-dependent proteins like kinases, by binding and inducing structural changes to the calcium-binding messenger protein calmodulin [74]. Though its wide range of suggested applications, EB toxicity to human normal cells is an open debate [75].

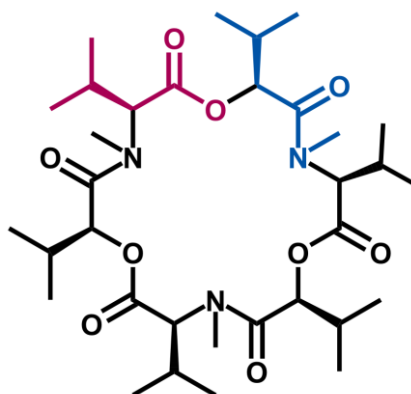


Figure 2.11. Structure of the cyclic AMP enniatin B. The *D*-hydroxyisovaleric acid and *N*-methyl-*L*-valine residues are highlighted in red and blue, respectively. The *N*-methylation of the valine amino acids, binding to the hydroxyl acid and cyclization reactions are carried out in a sequential manner by the enniatin synthetase enzyme.

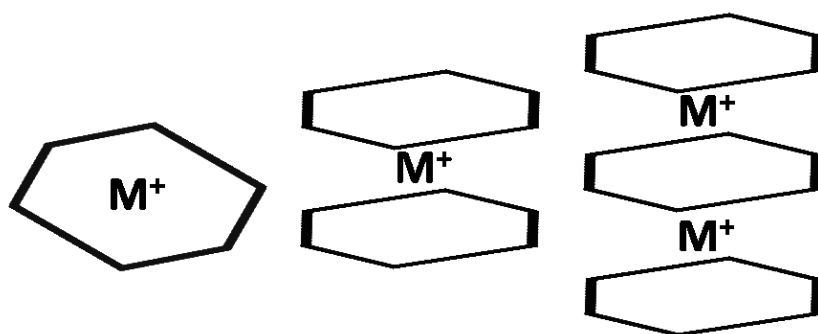


Figure 2.12. Schematic representation of the EB:ion complexes stoichiometry, 1:1, 2:1, 3:2 suggested by literature [61]. The M^+ correspond to monovalent metal ions. Divalent ions can form complexes as well, but were not studied in this work. The hexagons figures represent the EB ring structure.

Even though EB structure has been extensively studied and many complexes have been isolated and characterised in solution, there is scarce evidence about its behaviour inside the lipid membrane. Ovchinnikov and coworkers (1974) offered a detailed study on EB proving its ion complexation capability and predictions for the stoichiometry of EB:ion complexes [61]. The structural predictions from Ovchinnikov were supported by Kamyar et al. 30 years later by performing patch clamp experiments [76]. Zhukhlistova's (2002) X-Ray study of the EB complex with potassium thiocyanate (KNCS) provided a deeper understanding of EB complexones [77]. The ion-selectivity sequence for EB collected from previous studies presented in Pressman's review (1976) about ionophores, reveals a preference of monovalent cations over divalent cations [60]. This is in agreement with the suggestions made by Ovchinnikov (1974) [61] and Kamyar (2004) [76], with an extremely low K^+/Na^+ selectivity compared to beauvericin and valinomycin.

2.3.2. Arenicin 1

Arenicin is a family of AMPs that act against Gram-negative and Gram-positive bacteria, and fungi. To date, there are three variants known as arenicin1 (A1) and arenicin2 (A2), discovered in 2004 by Ovchinnikova et al. [64], and arenicin3 discovered in Denmark by a pharmaceutical firm bond to Novozymes (AdeniumBiotech). These peptides are derived from the marine polychaeta lugworm, *Arenicola marina*. Ovchinnikova and coworkers (2004) claimed that arenicins have not sequence match with any AMP family known to that date [64]. Both isoforms have 21 residues composing a two-stranded antiparallel β -sheet, rich in hydrophobic amino acids and arginines (Arg), and with one disulphide bond between cysteines Cys3 and Cys20 closing the 18-loop providing the peptide of a unique structure with a net charge of +6 [63] (see figure 2.13 for structure). Due to its rather globular arrangement, and controversial behaviour in solution and membrane environment, the isoform 1 (A1) of the arenicin family has presented more challenges to find a comprehensive description. Numerous

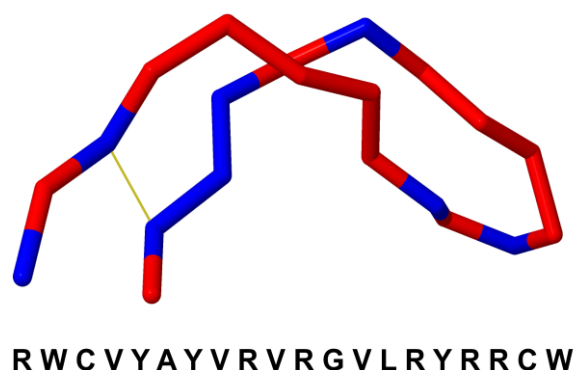


Figure 2.13. 3D representation of the A1 structure (PDB 2JSB [63]). Hydrophobic amino acids are marked in red, while hydrophilic residues are marked in blue. The yellow line connecting the two strands represents the disulphide bridge between Cys3 and Cys20. The one letter code amino acid sequence is shown below the representation denoting: R as Arginine, W as Tryptophan, C as Cysteine, V as Valine, Y as Tyrosine, G as glycine and L as leucine.

studies have already been carried out to elucidate the 3D conformation of A1, proposing different mechanism of interaction with the cell membrane [78] [79], and even conformational changes from solution to lipid bilayer [63]. In initial biological studies, arenicins showed similar antimicrobial activity compared to the strong antibiotic peptide protegrin-1 [64] and antifungal activity [80]. Cho and Lee (2011) suggested that A1 promotes the intracellular production of reactive oxygen species (ROS) and apoptotic reactions [81]. The same authors offered an interesting study of A1 using bacteria mimetic liposomes, where they observed that A1 provokes pronounced leakage in liposomes in comparison to other analogues, estimating a pore formation of at least 3.3 nm radii [78]. They also explained the role of the Arg residues for the A1 antibacterial activity, with emphasis in the Arg11 and Arg19 of the turn and C-terminus, respectively. In summary, A1 activity indicates a critical perturbation of the cell membrane. Andrä and coworkers (2008) suggested that A1 presents higher antimicrobial activity at 4°C and 37°C, and a strong adaptation to high salt concentration environments. Contrary to other authors, they found no significant selectivity of the peptide between zwitterionic and negatively charged lipids [63], which is believed to be the peptide's advantage towards low human cells toxicity [82]. Some of the mechanisms of action suggested for A1 so far are: lipid-microdomains formation, toroidal pores, carpet model, among others. Because of its relatively recent discovery, elusive conformation and interesting lipid interaction, there is room for new hypothesis of modes of action and structure of the antimicrobial peptide A1.

2.4. Theory of vibrational spectroscopy

The theory provided here is mainly based on the book *Vibrational Spectroscopy in Life Science* by Siebert and Hildebrandt (2008), and Dr Jacek Kozuch's dissertation, *Structure-Function Relationships of Membrane Proteins - Spectroelectrochemical Investigation of Artificial Membranes* [37] [21]. This section intends to offer the fundamentals of vibrational spectroscopy, Fourier transform infrared (FT-IR), attenuate total reflectance infrared (ATR-IR) and surface-enhanced infrared absorption (SEIRA) spectroscopy, which were used in the projects presented in this work for the study of biomolecules.

Vibrational spectroscopy probes the interaction of electromagnetic radiation with matter. This interaction causes transitions between the vibrational states of molecules. The roots of this technique arose in 1800, when William Herschel discovered the infrared (IR) radiation. He measured the temperature of the different colors of the rainbow spectrum that the sun-light created by passing through a glass prism, and found the highest temperature in the region beyond the red color, which was not visible. However, IR spectroscopy was not established as a technique after years later, obtaining the first IR spectra from probing matter with light². In 1920, the Indian physicist Sir Chandrasekhara V. Raman discovered the phenomenon of light scattering, later called Raman scattering. The Raman effect causes a change on the wavelength of part of the deflected light due to its interaction with matter. Initially, vibrational spectroscopy was used only for the study of small molecules and inorganic materials. Innovations in interferometers, invention of lasers, and improvements in purification methods for biological samples allowed the application of vibrational spectroscopy in life science.

Its wide application scope (organic and inorganic samples in industry and research)³ and capability to combine with other techniques situates vibrational spectroscopy within the most important techniques to study biomolecules. For instance, it can be combined with time-resolved techniques to study biological processes like biocatalysis or ligand binding [83]. Nowadays, Raman and IR can be used to probe and monitor structure-function relationship of macromolecules with higher resolution, and with lesser limitations in sample form and size than for other techniques. These characteristics are certainly reflected in the use of surface-enhanced Raman (SER) and surface-enhanced IR absorption (SEIRA) spectroscopy, where the metal surface properties are enhanced, acting also as an electrode to probe electrochemical processes.

² It was Herschel's son who 40 years later recorded the first IR spectrum from an alcohol-wetted paper.

³ Vibrational spectroscopy applications: quality control, forensic analysis, art and archaeology, NASA experiments, dynamic and reaction progress analysis, structure elucidation, among many others.

2.4.1. Basics of vibrational spectroscopy

The interaction of electromagnetic radiation with matter provokes transitions between the vibrational states of molecules, which can originate from a resonant absorption of IR radiation ($10\text{-}12500\text{cm}^{-1}$) or from inelastic scattering. If the energy of a photon $h\nu_{IR}$ from the polychromatic light matches the difference between the initial $h\nu_i$ and final $h\nu_f$ vibrational state, it results in IR absorption spectroscopy (eq. 2.1).

$$h\nu_{IR} = h\nu_f - h\nu_i \quad (2.1)$$

Raman spectroscopy uses monochromatic light to induce an inelastic scattering, where the energy of the scattered photon $h\nu_R$ differs from that of the incident light $h\nu_0$ (eq. 2.2).

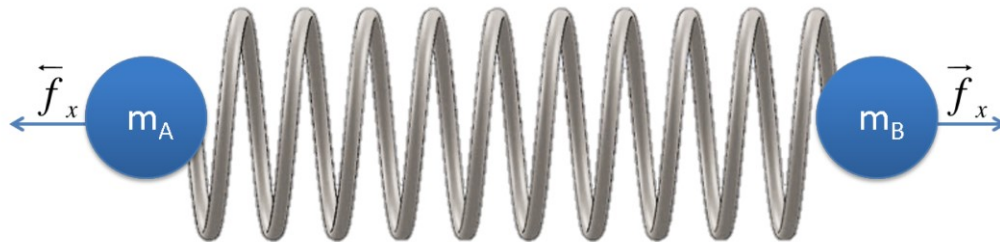
$$h\nu_0 - h\nu_R = h\nu_f - h\nu_i \quad (2.2)$$

The information obtained from both techniques is considered to be complementary, due to the difference in their underlying mechanisms. IR-active vibrations are those where the vibrational mode is accompanied by a change of the dipole moment; Raman-active vibrations require a change of the polarizability. IR and Raman can be represented in similar way for comparison, taking into account that on the ordinate of the spectrum the intensities are measured in different way for IR (absorbed light) or Raman (scattered light). The energy of the vibrational transition represented in wavenumbers ($\tilde{\nu}$ in cm^{-1}) on the abscissas, refers to the frequency of the absorbed light in IR, and to the frequency difference between the exciting and scattered light in Raman.

2.4.1.1. Molecular vibrations and the harmonic oscillator

The vibrations of a diatomic molecule A-B treated as a harmonic oscillator is frequently used to explain the fundamentals of molecular vibrations (see figure 2.14). The harmonic oscillator of two masses m_A and m_B connected by a spring in equilibrium position along the x-axis can be described by Hooke's law (eq. 2.3), where the restoring force F_x counters the displacement Δx provoked by the force constant f (representing the strength of the bond between A and B). Accordingly, the potential energy V and kinetic energy T , which depends on the reduced mass μ (eq. 2.6) and the velocity of their motion $\frac{d\Delta x}{dt}$, result in equations 2.4 and 2.5, respectively. The sum of the first derivatives of V and T must equal zero (eq. 2.7) to obey the conservation of the energy, leading to the Newton's equation of motion (eq. 2.8). This equation can be solved by the cosine function (eq. 2.9), where A , ω and θ are the amplitude, circular frequency (eq. 2.10), and phase, respectively. Thereby, one obtains equation 2.11 from applying Hooke's law to chemical bonds, which indicates that the ω of a harmonic vibration increases with the strength (or rigidity) of the bond, but decreases with the increase of the masses of the atoms involved.

Hooke's law $F_x = -f\Delta x$ (2.3)



$$V = \frac{1}{2} f \Delta x^2$$

Potential energy

(2.4)

$$T = \frac{1}{2} \mu \left(\frac{d\Delta x}{dt} \right)^2$$

Kinetic energy

(2.5)

Figure 2.14. Schematic representation of the harmonic oscillator system used to explain the vibrations of a diatomic molecule A-B, where two masses m_A and m_B are connected by a spring in equilibrium. When displaced from its equilibrium position, it experiences a restoring force, F , proportional to the displacement, x . This phenomenon is described by Hooke's law.

$$\mu = \frac{m_A \cdot m_B}{m_A + m_B} \quad (2.6)$$

$$0 = \frac{dT}{dt} + \frac{dV}{dt} = f\Delta x + \mu \frac{d^2\Delta x}{dt^2} \quad (2.7)$$

$$0 = f\Delta x + \mu \frac{d^2\Delta x}{dt^2} \quad (2.8)$$

$$\Delta x = A \cdot \cos(\omega t + \theta) \quad (2.9)$$

$$\omega = \sqrt{\frac{f}{\mu}} \quad (2.10)$$

$$\tilde{\nu} = \frac{1}{2\pi c} \sqrt{\frac{f}{\mu}} \quad (2.11)$$

2.4.1.2. Normal modes

In a normal mode of a molecule all atoms vibrate in a defined manner with the same frequency, but different amplitudes. The number of normal modes in a molecule corresponds to the vibrational degrees of freedom. A non-linear (linear) molecule with N atoms has $3N - 6$ ($3N - 5$, it can only rotate in two axes) degrees of freedom in a Cartesian coordinate system.

To describe the normal modes of a given molecule, the displacements of all atoms have to be considered. The use of the mass-weighted Cartesian displacement coordinates (eq. 2.13) in the kinetic energy T (eq. 2.12), results in 2.14. The potential energy V involves all possible interactions between all atoms (covalent, electrostatic, van-der-Waals...), resulting in a more complex term that can be expressed as a Taylor series (eq. 2.15).

$$T = \frac{1}{2} \sum_{\alpha=1}^N m_{\alpha} \left[\left(\frac{d\Delta x_{\alpha}}{dt} \right)^2 + \left(\frac{d\Delta y_{\alpha}}{dt} \right)^2 + \left(\frac{d\Delta z_{\alpha}}{dt} \right)^2 \right] \quad (2.12)$$

$$q_i = \sqrt{m_i} \Delta x_i \quad q_{i+1} = \sqrt{m_i} \Delta y_i \quad q_{i+2} = \sqrt{m_i} \Delta z_i \quad (\text{for each atom } \alpha = i) \quad (2.13)$$

$$T = \frac{1}{2} \sum_{\alpha=1}^N \left(\frac{dq_i}{dt} \right)^2 \quad (2.14)$$

$$V = V_0 \sum_{i=0}^{3N} \left(\frac{\partial V}{\partial q_i} \right)_0 q_i + \frac{1}{2} \sum_{i,j=1}^{3N} \left(\frac{\partial^2 V}{\partial q_i \partial q_j} \right)_0 q_{ij} + \dots \quad (2.15)$$

Since we are only interested in changes of V due to the displacements of the atoms, the first (V at equilibrium) and second (infinitesimal changes in q_i do not change V) terms in 2.15 are zero. Moreover, higher order terms can be neglected according to the harmonic approximation, simplifying V expression as expressed in 2.16. Therefore, 2.17 can be obtained after substitution into Newton's equation (eq. 2.8), which is composed by $3N$ linear second order differential equations and its general solution (eq. 2.18).

Thus, one obtains $3N$ solutions for λ corresponding to $3N$ frequencies $\lambda^{\frac{1}{2}}$. Finally, the frequencies of the normal modes are $3N - 6$ ($3N - 5$), since 6 solutions (5 for linear molecule) equal zero as they refer to the translation and rotation of the molecule. The amplitudes of the displacement of each atom A_i for every normal mode can be calculated with the obtained frequencies. As mentioned in the beginning, a normal mode represents an in-phase-oscillation of the entire molecule with a given frequency, but different amplitudes of certain segments of the molecule. As these amplitudes may

differ substantially, these normal modes may be reduced approximately to the part of the molecule with the most pronounced motion, in some cases being ascribed to specific group vibrations or single bonds.

$$V \approx \frac{1}{2} \sum_{i,j=1}^{3N} \left(\frac{\partial^2 q_i}{\partial q_i \partial q_j} \right)_0 q_i q_j = \frac{1}{2} \sum_{i,j=1}^{3N} f_{ij} q_i q_j \quad (2.16)$$

$$0 = \frac{d^2 q_j}{dt^2} + \sum_{i=1}^{3N} f_{ij} q_i \quad (2.17)$$

$$q_i = A_i \cdot \cos(\sqrt{\lambda} t + \theta) \quad (2.18)$$

The mass-weighted Cartesian coordinates can be converted into normal coordinates Q_k (for k normal modes) by the use of an orthogonal transformation 2.19, in order to simplify the description of the probability of vibrational transitions. Choosing the transformation coefficient l_{ik} in such a way that T and V assume the shape of equations 2.14 and 2.16, and the potential energy does not depend on the cross products $Q_k \times Q_{k'} k_0$ ($k \neq k'$) leads to the solution of the Newton equation 2.20.

$$Q_k = \sum_{i=1}^{3N} l_{ik} q_i \quad (2.19)$$

$$Q_k = K_k \cdot \cos(\sqrt{\lambda_k} t + \theta_k) \quad (2.20)$$

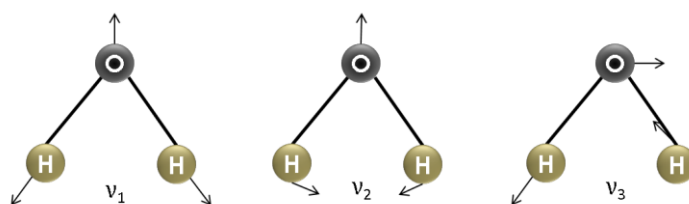


Figure 2.15. Schematic representation of the normal modes of water molecule. The water molecule is composed by one oxygen atom (O, black sphere) covalently bound to two hydrogen atoms (H, golden sphere). The number of normal modes of a non-linear molecule is given by $3N - 6$. Therefore, water exhibits $3 \cdot 3 - 6 = 3$ normal modes. The arrows represent the displacement of the atoms in each normal mode.

2.4.2. Infrared absorption spectroscopy

The IR absorption is shown as the absorbance A (in OD = optical density) by the use of the Lambert-Beer law (eq. 2.21). Here, I and I_{Ref} are the intensity of the IR radiation after passing through a solution with and without the analyte. The resulting absorbance is dependent on the conditions during the experiment reflected by the concentration c and the optical path length d , as well as on the molar absorption coefficient ε including the quantum mechanical probability of the transition between the initial and final vibrational state (eq. 2.1). The latter is given by the transition dipole moment (eq. 2.22), where ψ_f and ψ_i are the wave functions of the final and initial vibrational state and $\hat{\mu}_q$ the operator of the electric dipole moment (eq. 2.23). In 2.23, for each atom α , e_α and q_α refer to the charge and to its distance to the center of gravity of the molecule, respectively. The prerequisites for an IR-active absorption can be identified by expanding the operator of the electric dipole moment $\hat{\mu}_q$ in a Taylor series with respect to the normal coordinates Q_k . For a harmonic oscillator only the linear terms of the Taylor series have to be considered, so that $\hat{\mu}_q$ results in 2.24. Thus, the transition probability transforms into 2.26.

$$A = -\lg\left(\frac{I}{I_{Ref}}\right) = \varepsilon \cdot c \cdot d \quad (2.21)$$

$$[\mu_q]_{if} = \langle \psi_f^* | \hat{\mu}_q | \psi_i \rangle \quad (2.22)$$

$$\hat{\mu}_q = \sum_{\alpha} e_{\alpha} \cdot q_{\alpha} \quad (2.23)$$

$$\hat{\mu}_q = \mu_q^0 + \sum_{k=1}^{3N} \hat{\mu}_q^k \cdot Q_k \quad (2.24)$$

$$\hat{\mu}_q^k = \left(\frac{\partial \mu_q}{\partial Q_k} \right)_0 \quad (2.25)$$

$$[\mu_q]_{if} = \langle \psi_f^* | \hat{\mu}_q | \psi_i \rangle = \mu_q^0 \langle \psi_f^* | \psi_i \rangle + \sum_{k=1}^{3N} \hat{\mu}_q^k \langle \psi_f^* | Q_k | \psi_i \rangle \quad (2.26)$$

Due to the orthogonality of the wavefunctions ψ_f and ψ_i , the first term of equation 2.26 equals zero and, therefore, only a non-zero transition probability (IR-active transition) is achieved when the second term is non-zero. This is given when (i) the electric dipole moment of the molecule changes during the vibrational displacement of the atoms ($\hat{\mu}_q^k \neq 0$), and (ii) the quantum number between the states i and f differ by one within the harmonic approximation ($\langle \psi_f^* | \hat{\mu}_q | \psi_i \rangle \neq 0$). This consideration holds for all three Cartesian coordinates ($q = x, y, z$), so that the absorbance A of unpolarized light of

randomly oriented molecules arises from the sum of the transition probabilities along all three components (eq. 2.27). However, using linear polarized light on an oriented sample allows addressing the individual components of the transition dipole moment $[\mu_q]_{if}$ and, by this, obtaining more detailed information about the studied system.

$$A \propto ([\mu_x]_{if}^2 + [\mu_y]_{if}^2 + [\mu_z]_{if}^2) \quad (2.27)$$

2.4.3. Fourier transform IR

The principle of the Fourier Transform (FT) IR spectroscopy is applied in nearly all of today's IR spectrometers. Due to this approach, the measuring time can be drastically reduced, in contrast to the previous dispersive technique, leading to an improved signal-to-noise ratio.

The Michelson Interferometer is the central building block of an FT-IR spectrometer (figure 2.16), which comprises a beam splitter and two plane mirrors, i.e. a fixed and a movable mirror, oriented perpendicularly to each other. The beam splitter transmits and reflects the incoming polychromatic IR radiation, ideally divided in half, onto the two

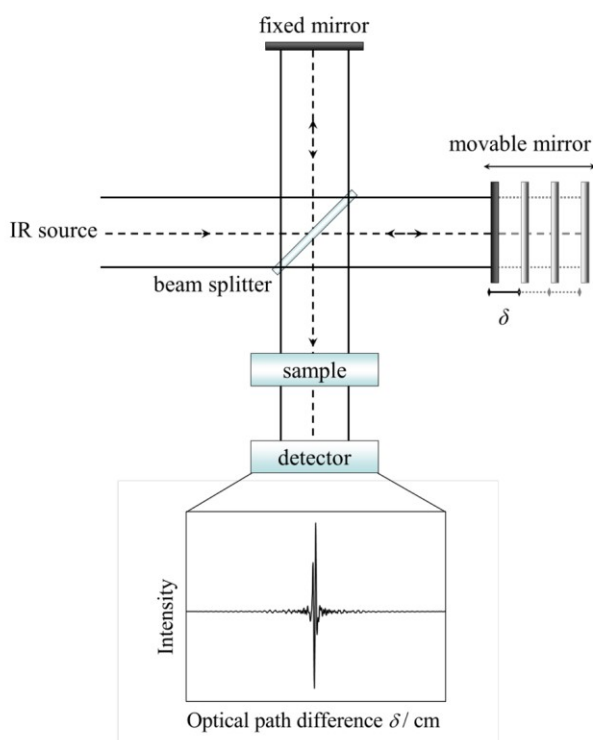


Figure 2.16. Michelson Interferometer: The IR radiation passes a beam splitter where it is divided into two parts and subsequently recombined directed at the sample. The movable mirror varies the optical path difference between the two beams generating an interferogram of the detected IR radiation. (Adapted and reprinted with kind permission from Jacek Kozuch (2013). *Structure-Function Relationships of Membrane Proteins - Spectroelectrochemical Investigation of Artificial Membranes*), Technische Universität Berlin, Fakultät II [21].

mirrors and subsequently recombines both beams directing it at the sample. With an optical path difference of $\delta = 0$, the distance between both mirrors and the beam splitter is equal leading to no phase difference between both beams and, therefore, the outgoing radiation equals the incoming one. Upon displacement of the movable mirror, however, the beams interfere with each other, so that each wavelength λ undergoes alternately constructive ($\delta = 2n \cdot \frac{1}{2}\lambda$) and destructive interference ($\delta = (2n + 1) \cdot \frac{1}{2}\lambda$), and results in a δ -dependent cosinusoidal modulation reflecting the respective wavelength λ . The signal that is accumulated on the detector is a superposition of the cosine functions of all frequencies of the polychromatic IR radiation and is referred to as an interferogram (figure 2.16).

The IR spectrum (frequency domain) is obtained after transforming the optical path length dependent interferogram (time domain) by use of the Fourier transform. This IR spectrum displays the attenuation of the IR radiation depending on the wavenumber (reciprocal wavelength) 2.28.

$$I(\tilde{\nu}) = \int_{-\infty}^{+\infty} I(\delta) \cos(2\pi\tilde{\nu}\delta) d\delta \quad (2.28)$$

This integral assumes an infinite motion of the movable mirror. Since the effective optical path difference is restricted to only a few centimeters, the interferogram has to be multiplied with an appropriate apodization function (i.e. a triangular function) to bring the edges of the interferogram smoothly to zero. With this procedure, artifacts in the spectrum are suppressed, but also the shape of spectral bands is manipulated. The advantages of FT-IR spectroscopy over the dispersive approach are presented in the box below.

- Multiplex or Fellgett advantage. On a FT spectrometer, the signal-to-noise ratio improves by \sqrt{M} for a spectrum comprised of M elements since the total noise is distributed over the entire spectral range, contrary to dispersive spectrometers where the complete noise intensity is recorded at each spectral data point.
- Throughput or Jacquinot advantage. In FT-IR, the implementation of Jacquinot circular apertures (to restrict convergent rays) results in higher signal-to-noise ratio, in comparison to the slits used in dispersive spectrometers.
- Connes advantage. The laser beam in a FT-IR instrument acts as an internal calibration of the mirror position providing a more precise wavenumber of spectral features than in dispersive spectrometers.

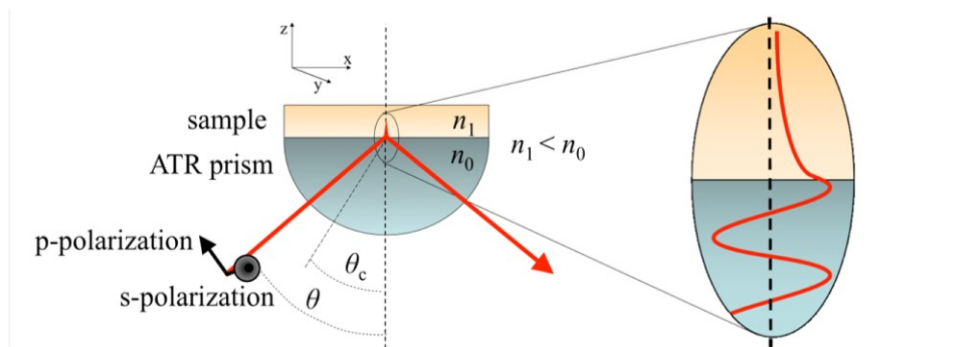


Figure 2.17. Schematic configuration for attenuated total reflectance-infrared (ATR-IR) spectroscopy. The incoming IR beam, composed of a perpendicular (s) and parallel (p) component (in respect to the plane of incidence) of the electromagnetic field, experiences total reflexion at the interface to an optically less dense medium, i.e. the sample, if the incident angle exceeds the critical angle θ_c . (Adapted and reprinted with kind permission from Jacek Kozuch (2013). *Structure-Function Relationships of Membrane Proteins - Spectroelectrochemical Investigation of Artificial Membranes*), Technische Universität Berlin, Fakultät II [21].

2.4.4. Attenuated total reflectance IR

The discovery of the attenuated total reflectance IR (ATR-IR) spectroscopy set the basis of the development of SEIRA. In this work, ATR-IR was used to investigate the structure of peptides in solid state by using a diamond-ATR durascope, which is a single-reflectance ATR with a diamond of ca. 2 mm diameter that is pressed against the sample. Additionally, SEIRA spectroscopy technique was employed in the ATR mode to perform the protein/peptide-membrane interaction experiments.

The phenomenon of total reflectance only takes place at the interface of the internal reflectance element (IRE) to an optically less dense medium at an angle of incidence higher than the critical angle θ_c . Silicon ($n_{Si} = 2.34$), germanium ($n_{Ge} = 4.0$), or zinc selenide ($n_{ZnSe} = 2.4$) are the most common materials for the IRE, due to a higher refractive index than biological systems ($n_1 \sim 1.44$). The propagation of an evanescent wave through the interface into the less dense medium is a by-product of the total reflectance. Interestingly, the amplitude of the evanescent wave decays exponentially in the direction normal to the surface (i.e. in z-direction) eq. 2.29 [84]. In 2.29, d_p represents the penetration depth of the evanescent wave at which the amplitude decayed to ca. 37 % ($\sim e^{-1}$) of its initial value. It depends on the wavelength of the radiation λ , the ratio of the refractive indices n_1/n_0 (of the IRE and the optically rare medium, respectively), and it is inversely proportional to the angle of incidence θ , as expressed in 2.30.

$$E = E_0 \exp\left(-\frac{z}{d_p}\right) \quad (2.29)$$

$$d_p = \frac{\lambda}{2\pi \sqrt{\sin^2\theta - \left(\frac{n_1}{n_0}\right)^2}} \quad (2.30)$$

The d_p is in the range of the wavelength of the incident radiation. For instance, in the case of a Si prism, an incident angle of 60° (as used in this work), and a spectral region of 1000 to 4000 cm⁻¹ (10-2.5 μm) the penetration depth of the evanescent wave is between 2.6 and 0.7 μm, respectively. An absorbing medium placed onto the surface of the IRE can couple with the electric field of the evanescent wave, absorb energy of the radiation and, thus, attenuate the total reflected beam. The parallel (p) and perpendicular (s) components of the incident radiation (in respect to the plane of incidence) causes a polarization of the evanescent wave in the x- and z-directions, as well as in the y-direction [84].

The important advantage of the ATR technique is the possibility to adsorb the sample on the IRE surface and study its structure and dynamics. This means that the supernatant buffer solution can be exchanged very easily to study effects of the experimental conditions (pH, ionic strength etc.), binding of substrates and ligands. Additionally, preferably oriented samples can be adsorbed on the IRE to obtain additional information about the orientation of structural elements, such is the case of membrane proteins.

2.4.5. Surface-enhanced IR absorption SEIRA spectroscopy

Hartstein et al. discovered in 1980 the SEIRA effect, which was observed from contaminant hydrocarbons while measuring aromatic carboxylic acids adsorbed on Ag (silver) and Au films by ATR-IR [85]. The SEIRA effect presents certain mechanistic analogy to surface-enhanced Raman scattering (SERS). Accordingly, one can define SEIRA as a spectroscopic technique that uses a nanostructured metal film, in this case Au, in the interface between the IRE (i.e. a silicon prism) and the sample. The plasmonic resonance of the nanostructured Au results in an increase of the IR signal in 10-100 times [86]. This enhancement is restricted, presenting a steep decay of the signal at approximately 8 nm from the metal surface. Furthermore, there is also an orientation selection rule with a strong enhancement along the normal of the Au surface. The Au-film, which also functions as the working electrode, can be functionalized with a SAM for a wide range of applications, such as oriented proteins, membrane systems, electrochemical reactions or potential dependence of protein or peptides, among many others [11] [14] [29] [87] [88] [89].

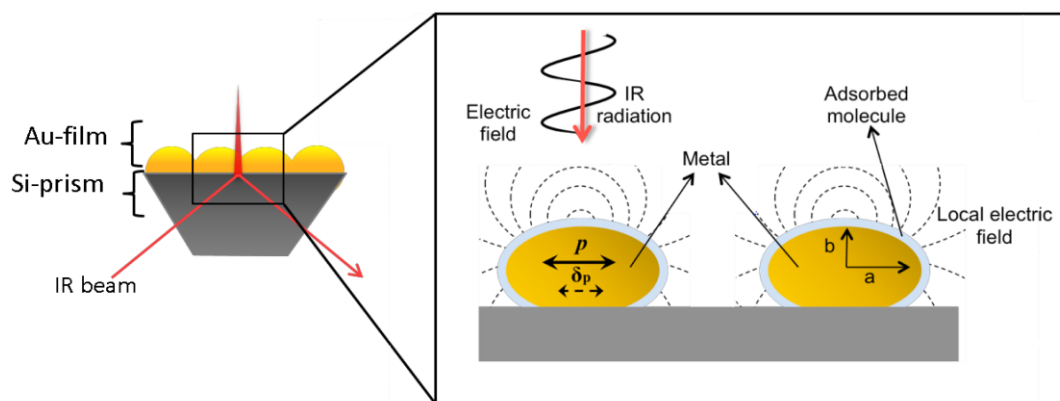


Figure 2.18. Schematic representation of the EM mechanism of the SEIRA effect originating from ellipsoidal metal particles. The electric field component of the incident IR radiation polarizes the metal islands. The dipole P generates an enhanced local electric field around the particles that excites the molecular vibrations of the adsorbed molecules. Furthermore, the molecular vibrations induce an additional dipole δ_p and perturb the optical properties of the metal. (Adapted and reprinted with kind permission from Jacek Kozuch (2013). *Structure-Function Relationships of Membrane Proteins - Spectroelectrochemical Investigation of Artificial Membranes*), Technische Universität Berlin, Fakultät II [21].

The electromagnetic (EM) mechanism is believed to contribute to the enhancement of the IR absorption of the probe molecule, due to similarities to the SERS effect. This enhancement is conditioned by metal islands morphology, which can be represented as ellipsoidal metal particles (see figure 2.18) [90]. The box below offers a brief description of the nature of the enhancement mechanism for the SEIRA effect.

Electromagnetic (EM) mechanism

The incident photon field polarizes the metal particles through excitation of collective electron resonance (localized plasmon modes). The induced dipole p in the particles creates a local EM field around them, which is polarized perpendicularly to the metal surface (surface selection rule, vibrations associated with p changes parallel to the surface are invisible). The interaction of the adsorbed molecules with the created EM field results in the transitions between vibrational states. The field enhancement decays with the distance d to the metal surface, which explains the short-range effective enhancement. The enhancement factor F can be expressed at a distance d and a nanoparticle radius a_0 .

$$F(d) = F(0) \cdot \left(\frac{a_0}{a_0 + d} \right)^6 \quad (2.31)$$

The dielectric function of the metal can be affected by the oscillating dipoles of adsorbed molecules. This perturbation of the optical properties of the metal results in induced dipoles δ_p in the metal particles, causing an effective enhancement of the IR absorption due to the much larger absorptivity of metals.

2.5. Theory of electrochemical impedance spectroscopy

Electrochemical impedance spectroscopy (EIS) is a method that allows measuring the resistance and the capacitance of interfacial layers. These parameters are related to the ability of a system to resist the flow of current and to accumulate electrical energy, respectively. EIS is relevant for characterisation in material science. However, nowadays it is applied in a much broader scope [91], like the study of monolayers and membrane systems [29] [92]. The capacitance C is associated with the area of the electrode A and the distance d :

$$C = \frac{\varepsilon_0 \cdot \varepsilon \cdot A}{d} \quad (2.32)$$

where ε_0 and ε are the constant electrical permittivity in vacuum and the characteristic ability of a material/medium to store electrical energy [21]. The most common way of performing EIS is to apply an alternating voltage of small amplitude to the electrode and record the phase shift and amplitude, or the real and imaginary parts, of the resulting current. By scanning the frequency (in the range of 1 mHz and 1 MHz) a complete spectrum can be measured. EIS can be described as the interaction of the dielectric medium or the analyte with the externally applied and alternating electric field. In this work, EIS is combined with SEIRA with the aim of characterising the SAMs and the tBLM systems employed for the study of the targets.

2.5.1. Basic theory of the electrical impedance

Electrical impedance

$$Z(\omega) = \frac{U(\omega, t)}{I(\omega, t)} \quad (2.33)$$

$$Z(\omega) = \frac{U_0 \sin(\omega t)}{I_0 \sin(\omega t + \theta(\omega))} \quad (2.34)$$

The electrical impedance $Z(\omega)$ is defined as the frequency-dependent resistance [93], expressed as the ratio of the alternating voltage and the resulting current 2.33. This current $I(t) = I_0 \sin(\omega t + \theta(\omega))$, with a phase difference θ can be measured when applying a monochromatic signal $U(t) = U_0 \sin(\omega t)$ with a single frequency of $\nu = 2\pi\omega$. Consequently, 2.33 is transformed into 2.34 [94]. For purely resistive behavior θ is zero, and the responses of capacitive C and inductive L elements are $I(t) =$

$[dU(t)/dt]C$ and $U(t) = [dI(t)/dt]L$, respectively. The analysis of a system with these differential equations can be simplified by the Fourier transform converting into the frequency domain (which is also the variable in an EIS measurement). After the conversion one obtains the voltage $U(\omega) = U_0 \pi$ and current $I(\omega) = I_0 \pi e^{i\omega}$, as well as the solution of the differential equations for a resistive 2.35, capacitive 2.36 and inductive 2.37 behavior ($i = \sqrt{-1}$).

$$Z_R(\omega) = R \quad \text{with} \quad \theta = 0 \quad (2.35)$$

$$Z_C(\omega) = (i\omega C)^{-1} \quad \text{with} \quad \theta = -\frac{\pi}{2} \quad (2.36)$$

$$Z_L(\omega) = i\omega L \quad \text{with} \quad \theta = +\frac{\pi}{2} \quad (2.37)$$

Complex impedance

$$Z(\omega) = R(\omega) + iX(\omega) = \text{Re}(Z(\omega)) + i\text{Im}(Z(\omega)) \quad (2.38)$$

$$\text{Re}(Z) = R = |Z|\cos\theta \quad \text{and} \quad \text{Im}(Z) = X = |Z|\sin\theta \quad (2.39)$$

$$Z(\omega) = |Z|(\omega)e^{-i\theta(\omega)} \quad (2.40)$$

This impedance is a complex quantity (real and imaginary parts) that can be represented as 2.38, where the real part R (in-phase) and the imaginary part X (out-of-phase) are the resistance and the reactance, respectively. The reactance gives information about the capacitive C and the inductive L of the system. The two coordinate values of the Impedance vector plotted in a Cartesian system can be written as 2.39 with the phase angle $\theta = \arctan \frac{X}{R}$ and the magnitude of the impedance $|Z| = \sqrt{R^2 + X^2}$. By using the Euler rule the impedance Z may be rearranged in polar coordinates and expressed as 2.40.

Admittance

The admittance Y (eq. 2.41) is the inverse of the impedance. The real part is the conductance G and the imaginary part the susceptance B . The partial fraction decomposition (eq. 2.39) can be used to calculate them. Usually, Z and Y are expressed by distinguishing between resistive R and capacitive C components in series $Z = R_s(\omega) - iX_s(\omega)$ or in parallel $Y = G_p(\omega) - iB_p(\omega)$. From this approach, the reactance X and the susceptance B result in 2.43.

$$Y = Z^{-1} = G + iB \quad (2.41)$$

$$Y = Z^{-1} = \frac{1}{R + iX} = \frac{R}{R^2 + X^2} + i \frac{-X}{R^2 + X^2} \quad (2.42)$$

$$X_S(\omega) = (\omega C_S(\omega))^{-1} \quad \text{and} \quad B_P(\omega) = \omega C_P(\omega) \quad (2.43)$$

2.5.2. Graphical representation of impedance data

The graphical representations explained in this work are based on the circuit presented in figure 2.19 and the mathematical expressions described above. Here, R_{solution} represents the resistance of the electrolyte, and below are the resistance R and capacitance C of the bilayer and spacer regions. This circuit serves as an approximation of the electrical properties of a functionalised electrode in contact with an electrolyte [93]. In this case, there are three important representations: Nyquist plot, Bode plot and Cole-Cole plot. The latter is the most relevant for the analysis of the systems presented in this work.

The Nyquist plot is the most common representation of the EIS data. It is based on the complex impedance $Z = R - iX$, which plots the imaginary part $\text{Im}(Z(\omega)) = X(\omega)$ versus the real part $\text{Re}(Z(\omega)) = R(\omega)$ as function of the angular frequency $\omega = (2\pi)^{-1}\nu$.

The Bode plot, where the magnitude of the impedance $|Z|$ and the phase difference θ are plotted against the frequency ν , can be divided into three regions. The first and third regions of the spectra correspond to the very high and low frequencies, respectively. Here, the impedance is independent of the frequency and shows pure

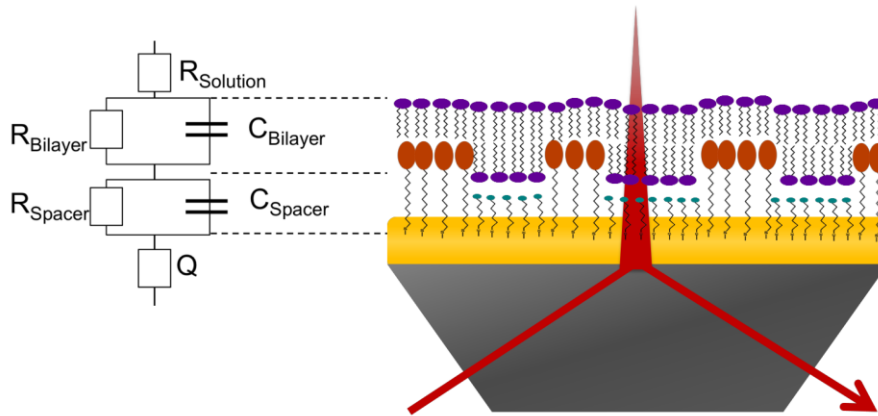


Figure 2.19. Scheme of the system used to study the dielectric properties of the SAMs and tBLM systems. The $R_{\text{bilayer}}-C_{\text{bilayer}}$ element and $R_{\text{spacer}}-C_{\text{spacer}}$ element described the hydrophobic bilayer region and the hydrophilic spacer region, respectively. The system is supported on a Au electrode (by attachment of the SAM) and in contact with the supernatant electrolyte above the bilayer region, adapted from [21].

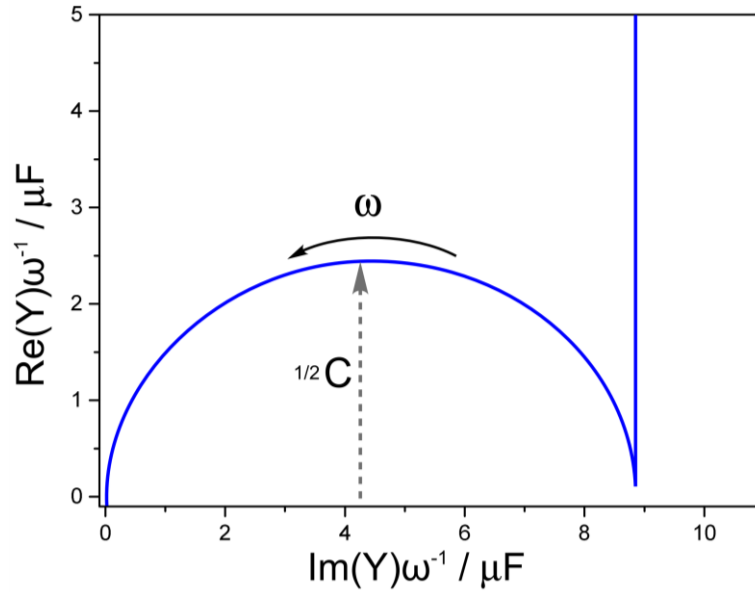


Figure 2.20. Scheme of the system used to study the dielectric properties of the SAMs and tBLM systems. The $R_{\text{bilayer}}-C_{\text{bilayer}}$ element and $R_{\text{spacer}}-C_{\text{spacer}}$ element described the hydrophobic bilayer region and the hydrophilic spacer region, respectively. The system is supported on a Au electrode (by attachment of the SAM) and in contact with the supernatant electrolyte above the bilayer region, adapted from [21].

resistive behavior ($Q = 0$). At high frequencies (first region) appears the low resistance R_{solution} and at low frequencies (third region) the sum of all resistances. In the middle area, the impedance is frequency-dependent due to the presence of $C_{\text{bilayer}}/C_{\text{spacer}}$. According to 2.36, $\theta = -\frac{\pi}{2}$ (by the phase approximation) and $C_{\text{bilayer}}/C_{\text{spacer}}$ is calculated by $C = (\omega|Z|)^{-1}$.

The Cole-Cole plot represents a direct analysis of the capacitances ($C_{\text{bilayer}}/C_{\text{spacer}}$) by reading out the radius of the first semicircle (see figure 2.20), which is an advantage with respect to other representations. In this case, the imaginary and real parts are divided by the angular frequency ω . Due to the direct relation to the C values, this plot was the one used to characterise the properties of the systems studied in this work.

2.5.3. Graphical evaluation and physical relevance in tBLM systems

It is important to mention that the resistance and the capacitance are the physical properties that are used to characterise the membrane system, with the additional component for the resistance of the electrolyte (in the high frequencies due to its low magnitude). However, EIS can be used as well to monitor the capacitance of the electrode, and the properties of the Helmholtz layer or the ionic reservoirs beneath the bilayer. These terms can be neglected upon modeling the system, since these parts are usually not found in the same frequency range as the resistance and capacitance of

the membrane. The presence of defects or pores, however, might intensify the influence of the sub-membrane region of tBLMs [95].

These electrical properties of a system can be obtained manually or by modeling of the studied system [96]. There exist two approaches, the continuum theory [94] and the use of semi-empirical methods. Semi-empirical methods have the advantage of using already established and optimized models for certain properties of the system. In both cases, the system is approximated to an equivalent circuit that provides the mathematical equations for a fit to the data. In this work, a non-linear least squares fitting based on the Levenberg-Marquardt algorithm was applied [97]. The concepts presented in the following blue box were used to describe the systems studied here [98] [99] [94] [100].

Ohmic resistance of a membrane

The hydrophobic core of a lipid bilayer acts as a barrier for ions and other molecules. Therefore, it can be treated as an isolator with the Ohmic resistance R .

Capacitance of a membrane

The membrane can be described as a capacitor C as shown in 2.32. Whereas A depends on the dimensions of the experimental assembly, the thickness d (in a bilayer it is in the range of 4-6 nm) depends on the phospholipid composition. The dielectric constant of the hydrophobic core is $\epsilon_r = 2.1 - 2.8$, and of the hydrophilic head group region (thickness $\sim 0.6 - 1$ nm) is $\epsilon_r = 20$. Neglecting the contribution on the latter term by the dielectric constant of water ($\epsilon_r = 80$) due to the solvation level of the headgroups, the specific capacitance of a membrane with a hydrophobic part of 4 nm is shown in 2.44, which matches the experimental results

$$C_{sp} = \frac{\epsilon_r \epsilon_0}{d} \approx 0.5 - 0.6 \mu F cm^{-2} \quad (2.44)$$

Constant phase element

In the case of a non-ideal capacitive behavior, the capacitance can be replaced by a constant phase element (CPE) that treats the dielectric constant as a complex magnitude on the basis of the Debye theory. The advantage of this approach is a better fit that describes the system more precisely. The resulting impedance is expressed in 2.45, where α is a parameter with the property $0 < \alpha < 1$. At $\alpha = 1$, this approach describes an ideal capacitor and Q equals the capacitance C (see eq. 2.36). All other cases yield the quantity Q with the unit $F s^{\alpha-1}$, which cannot be compared directly with C . Fortunately, both values might be related to each other when the CPE-element lies in parallel to an ohmic resistance (2.45). The term is the frequency at which the imaginary part Im reaches its maximum value.

$$C = Q(\omega_{max}'')^{\alpha-1} \quad (2.45)$$

3. Experimental section

3.1. Materials

Chemicals	Provider
1PrOH	Merck
6MH	Sigma Aldrich
Ag/AgCl reference electrode	World Precision Instruments, Inc.
CHCl ₃	Sigma Aldrich
CsCl	Merck
EtOH	Sigma Aldrich
Extruder	Avestin
HClO ₄	Merck
HF	Sigma Aldrich
MeOH	Sigma Aldrich
NaCl	Sigma Aldrich
NaOAc	Fluka
Na ₂ S ₂ O ₃ •5H ₂ O	Sigma Aldrich
Na ₂ SO ₃ anhydrous	Sigma Aldrich
NaAuCl ₄ •3H ₂ O	Sigma Aldrich
NH ₄ Cl	Sigma Aldrich
NH ₄ F	Sigma Aldrich
NiSO ₄	Sigma Aldrich
Dithiobis(C2-NTA)	Dojindo Laboratories
KCl	Sigma Aldrich
POPC/POPG	Avanti Polar Lipids
Polycarbonate filters (100nm)	Avestin

All chemicals were of highest purity grade available.

Nanodisc samples containing the ChR II C128S mutant and the ChR II C128S mutant samples in solution were provided by Dr. Michael Szczepek from the Institute of Medical

Physics and Biophysics, Charité (Berlin, Germany). The AMP samples of enniatin B and arenicin 1, were provided by Dr. Lennart Richter from the synthetic biotechnology and antibiotics group (Prof. Roderich Süßmuth), Technische Universität Berlin (Berlin, Germany), and by Prof Dr. Thomas Gutsmann group from the Division of Biophysics, Research Center Borstel, Leibniz-Center for Medicine and Biosciences (Borstel, Germany), respectively.

Detailed description of the synthesis and characterization of the tethered molecule WK3SH can be found in the supplementary information of the article by Wiebalck (2016) [29].

3.2. Sample preparation

Buffer preparation

All buffers were prepared using MilliQ water with a resistance of $>18\text{ M}\Omega\text{ cm}$, titrated at required pH with hydrogen chloride (HCl) or sodium hydroxide (NaOH). The pH was determined using a pHSEmeter (brandmodel) with corresponding pH-electrode.

For the Chr2 experiments, a 50 mM sodium acetate (NaOAc) at pH 5.5 and a 100 mM sodium chloride 20 mM BTP pH 8.8 were prepared. And in the case of AMPs, all buffers were prepared with the corresponding chloride salt at 100 mM and 20 mM BTP at pH 7.4.

Nanodisc containing Chr II C128S membrane protein

The nanodisc samples containing the Chr II C128S protein were stored in 50 μL aliquots with a concentration of 50 μM at -80°C . The storage solution was 130mM NaCl 1mM MgCl 10% Glycerol 20mM BTP pH 7.2. The Chr II C128S protein in solution was stored using the same conditions at a concentration of 80 μM . All experiments were performed at 4°C , and a fresh aliquot was thawed prior incubation. The nanodisc samples were diluted to 1 μM for SEIRA experiments and incubated for ca. 2 hours. For the IR transmission experiments the samples were concentrated ca. 3 times. For the UV-vis measurements, samples were diluted with the respective buffer to a concentration of 3 μM . The samples were under red light during incubation, as well as prior and after the illumination process.

Ni-NTA monolayer assembly for nanodisc systems

Aliquots of 10 mM NTA were prepared from a 100 mM stock solution, and kept at -20°C . For each experiment, one aliquot was thawed, diluted with H_2O to 1 mM solution, and incubated overnight onto a fresh prepared Au-film. Then, the excess was washed away by rising with NaOAc 50 mM pH5.5 buffer. Once stable, a solution of 50mM NiSO_4 in NaOAc buffer was added and incubated for 1 hour. The excess was removed with fresh NaOAc buffer. Prior to the nanodisc system immobilisation, the buffer was exchanged to the 100 mM NaCl 20 mM BTP at pH 8.8. The nanodisc samples

with embedded membrane protein were added at a concentration of 1 μM and incubated for 2 hours. The activity of the retinal protein was analysed by UV-vis spectroscopy before performing the SEIRA experiment.

Vesicle Preparation

For the POPC vesicles, 10 μL of a 25 mg mL^{-1} POPC lipid (in chloroform stock solution) and 100 μL chloroform were mixed in a test tube. To prepare the mixed POPC/POPG vesicles, in a test tube were added 8 μL of the 25 mg mL^{-1} POPC lipid, 5 μL of the 10 mg mL^{-1} POPC lipid (in chloroform stock solution) and 100 μL of a 50:50 CHCl_3 :MeOH mix. In both cases, the solution was dried with N_2 stream and set under vacuum overnight. The next day, lipids were re-dissolved with 500 μL of the corresponding 100 mM chloride salt (Na^+ , Cs^+ or K^+ depending on the experiment) 20 mM BTP buffer at pH 7.4. The vesicles were prepared by repeating 3 cycles of 30 s vortexing and 10 min resting in between. Afterwards, the solution was extruded 31 times through a 100 nm pore size filter in order to obtain POPC unilamellar vesicles of 100 nm size.

Antimicrobial peptides

The purified solid of enniatin B peptide was dissolved in EtOH and divided in equal aliquots of a final concentration of 100 μM . The aliquots were dried in a speedvac centrifuge and stored at -20°C . Prior experiment, aliquots were dissolved in 100 mM chloride salt 20 mM BTP buffer pH 7.4 with 2% EtOH. All experiments with enniatin B were carried out at 25°C .

The purified solid of arenicin 1 peptide was dissolved in a 3:1 EtOH NaCl-BTP buffer to a final concentration of 100 μM and stored at -20°C . The experiments with arenicin1 were carried out at three fixed temperatures: 4°C , 25°C and 37°C .

3.2.Methods

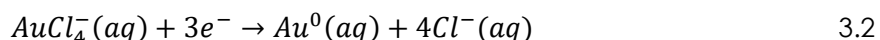
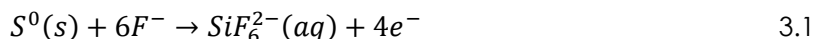
SEIRA cell

The experiments were performed using a homemade spectroelectrochemical SEIRA setup and ATR prism coated with a freshly prepared nanostructured Au-film. This setup was used to perform SEIRA and EIS experiments. It allows the use of a thermostat and electrochemical measurements in a three-electrode configuration as shown in figure 3.1. A trapezoidal Si crystal (L:25 mm, W:20 mm and H:10 mm) was used as ATR prism. The IR signal irradiates the prism in an incident angle of 60° giving a measuring area of 7 mm x 3 mm. The OPUS 5.5 software was employed to evaluate the spectra acquired using a Bruker IFS66v/s FT-IR-spectrometer. The IFS spectrometer is equipped with an ATR setup in the Kretschmann configuration, a photoconductive liquid N_2 -cooled MCTdetector (HgCdTe), and a global as the IR radiation source. The global, the Michelson Interferometer, and the detector were operated under vacuum; solely the sample chamber was purged continuously with nitrogen gas. SEIRA spectra were

recorded between 4000 and 1000 cm⁻¹ with a spectral resolution of 4 cm⁻¹. Each spectrum comprises 400 scans.

Au deposition and electrochemical cleaning

The Si prism was polished with alumina powder (Microgrit WCA-9, grain size ca. 6 µm) and abundantly rinsed with H₂O to obtain a hydrophobic surface. The Au-film was prepared following the electroless deposition procedure [101]. Then, a solution of 400 g/L NH₄F was added to the prism's surface for 2 min. After rinsing with H₂O, the prism was dried and placed in a H₂O bath at 65° C. Meanwhile, the Au solution was prepared with equal volumes of a 2% (w/w) HF solution, a 0.03 M NaAuCl₄•3H₂O solution, and a plating solution containing 0.3 M Na₂SO₃ anhydrous, 0.1 M Na₂S₂O₃•5H₂O and 0.1 M NH₄Cl. Subsequently, the Au solution was deposited onto the prism. The reaction was stopped after 1 min by washing with H₂O. Lastly, the prism with the Au-film was dried with N₂ stream.



For the electrochemical cleaning, the prism was properly assembled into the SEIRA setup. The Au surface was rinsed with H₂O before adding the 0.1 M HClO₄ solution. The reaction was conducted by running 6 oxidation/reduction cycles between 0.1 and 0.4 V, under constant Ar purge to avoid the formation of reactive oxygen species. The area of the Au electrode was calculated by using the area of the single reduction peak at ca. 920 mV obtained during the sixth reduction cycle, and comparing it to the specific charge density of 400 µC cm⁻² [102]. The cyclic voltammetry (CV) measurement was monitored using the GPES software, and a CHI 600E series potentiostat from CH Instruments, Inc with a three-electrode configuration. The Au-film with a real area of ca. 1.65 cm²; geometric area of 0.79 cm² corrected by the roughness factor of 2.1; newly

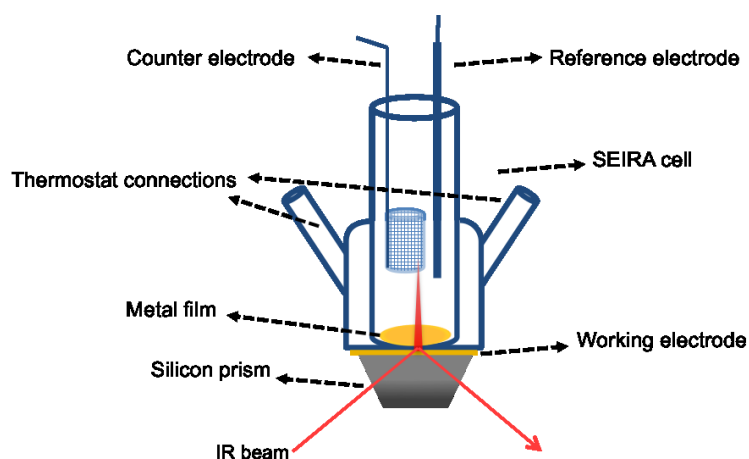


Figure 3.1. Schematic representation of the spectroelectrochemical SEIRA cell. The relevant features are indicated in the figure. The Au metal-film acts as IR signal amplifier and working electrode. The IR beam irradiates the silicon prism with an incident angle of 60° with respect to the surface normal.

determined for each Au-film using the Au-oxide reduction charge density method) is used as working electrode. The Pt-mesh, and Ag/AgCl (3 M KCl) electrode serve as counter, and reference electrodes, respectively (all potentials are referred to the Ag/AgCl electrode).

Tethered bilayer lipid membrane construction

The Au-film was functionalized with a mixed self-assembled monolayer (SAM) of WK3SH/6MH 80:20, which was incubated overnight in a solution of 0.6 mM WK3SH and 0.4 mM 6MH in 1-PrOH. For the bilayer formation, unilamellar POPC or POPC/POPG vesicles were added onto the SAM after rinsing in order with 1-PrOH, H₂O and the corresponding buffer. The lipids were incubated for 2 hours or until a stable difference spectrum was achieved. Then, the SEIRA cell was rinsed abundantly with fresh buffer. Impedance and SEIRA spectra of the SAM and lipids were recorded to characterise the step-wise construction of the tBLM. Detailed information of the construction of such a system can be found in the supplementary information of the article by Wiebalck and coworkers (2016) [29].

Tethered hybrid lipid membrane construction

The tethered hybrid lipid monolayer (tHLM) was built following the same step-wise procedure as for the tBLM, but using a pure WK3SH monolayer instead of the mixed SAM. It was monitored by EIS and SEIRA spectroscopy as well.

Illumination procedure

SEIRA and FT-IR transmission spectroscopy were used to follow the illumination assay of the ChR II protein in the nanodisc system and in solution, using in both case the same procedure. The illumination assay was performed using a blue ($\lambda \sim 460$ nm) LED and a UV ($\lambda \sim 390$ nm) LED. A macro for the OPUS software was designed to repeat 8 cycles of the following process: Dark/ 460 nm/ 390 nm/ Dark. The dark steps were recorded for ca. 30-40 min and the light steps for ca. 10 min.

FT-IR transmission and ATR-IR spectroscopy

Bruker IFS28 and Tensor27 spectrometers were used for these experiments, accumulating 200 scans instead of the 400 in SEIRA experiments. A sandwich-transmission cell with CaF₂ windows was used for the sample preparation. The ChR II and Nanodisc samples were deposited on the sample window by 5 cycles of 2 μ L of sample and drying with N₂ gas stream, distributing the sample homogeneously on the surface. The sample was deposited onto a CaF₂ window with a 2 μ m deepening. Afterwards, a thin layer of silicone grease was applied to seal the cell, before closing with a plain CaF₂ window. The cell was placed into the corresponding holder to perform the experiments. In the case of the AMP samples, 2 μ L of sample were placed onto the deep window and sealed as mentioned before (no drying step). All experiments were performed at room temperature. Additionally, a diamond-ATR durascope setup was used to measure the dried samples of the peptides. The setup can be used in both

spectrometers mentioned above, and consists of a single-reflectance ATR with a diamond of ca. 2 mm diameter that is pressed against the sample.

UV-vis spectroscopy

A Cary 50 Bio spectrophotometer (Varian Inc.) or Cary 4000 UV-vis spectrophotometer (Agilent Technologies) was used to measure stationary or time-resolved (in seconds to minutes) absorption spectra. The ChR II and nanodisc samples of 300 μL (3 μM) were measured in a UV quartz cuvette with a total volume of 500 μL (Blaubrand QS 1.000) and a path length of 1 cm. The absorption spectra were recorded between 200 and 900 nm with a 1 nm resolution.

The buffer solution was measured as the black, and it was used together with the zero-transmission to carry out the standard baseline correction. A similar illumination procedure as the one described in the SEIRA experiments was applied for the UV-vis using the blue ($\lambda \sim 460$ nm) LED and a UV ($\lambda \sim 390$ nm) LED.

The kinetic measurements of the ChR II C128S protein embedded into the nanodisc system were performed following a similar procedure as described by Velazquez (2015) [103]. The intensity was monitored at $\lambda = 480$ nm in the dark, with the 460 nm light on, and with the 460 nm light off for a total time of 40 min. The resulting data was evaluated using the ORIGIN 7 software package or higher (OriginLab, Northampton, MA), and the curves were simulated using exponential decay functions.

Electrochemical impedance spectroscopy

The electrochemical impedance (EIS) measurements were performed using a $\mu\text{Autolab III/FRA2}$ instrument, and controlled with the frequency response analyser software. The Au-film served as the working electrode in a three-electrode configuration with a Pt-mesh as counter electrode and a Ag/AgCl (3 M KCl) reference electrode. EIS spectra were recorded in the frequency range of 0.05 Hz to 100 kHz at a DC potential of 250 mV (vs Ag/AgCl) and amplitude of 25 mV (rms). The same software was used to carry out the fitting of the EIS data using the equivalent circuit described in the theory section.

Potential-dependence assay

The $\mu\text{Autolab III/FRA2}$ instrument and the three-electrode configuration were used to perform the potential-dependent (+ 400 mV to - 400 mV) experiment of the arenicin 1 peptide, which was monitored by SEIRA spectroscopy. The experiment was performed at 25° C and 37° C.

DFT calculations

In the density functional theory (DFT), the total energy E of an electronic system is determined by its electron density r . The total energy is written in terms of the energy of n non-interacting electrons and a term E_{ex} that takes into account the complicated correlated motion of the electrons. Here, DFT is used to find the most stable stoichiometry for a given structure of the EB peptide, and calculate its vibrational

frequencies. The method of calculation used was [BP86 functional with basis sets LanL2DZ for metals and 6-31 g* for N, C, O, H]. Initially, only the dihedral angles of the ring backbone were fixed to 180° during geometry optimization. After this initial optimization, the geometry was optimized without constraints.

The density functional theory (DFT) calculations for the enniatin B complexes were carried out by Dr. Jacek Kozuch, Postdoctoral Researcher at Boxer Lab (Prof. Steven Boxer), Stanford University (California, United States). The FT-Raman measurement of the solid sample of arenicin 1 peptide was kindly performed by Dr. Francisco Velazquez from the Department of Physical Chemistry / Biophysical Chemistry (Prof. Peter Hildebrandt), Technische Universität Berlin (Berlin, Germany). The molecular dynamic (MD) simulations of the arenicin 1 peptide in the POPC/POPG tBLM system were carried out by Ahn Duc Nguyen, Biomolecular Modelling group (Prof. Maria Andrea Mroginski), Technische Universität Berlin (Berlin, Germany)

4. Results

4.1. Channelrhodopsin II in nanodisc systems

In this study, channelrhodopsin II (ChR II) was used as a proof of concept for the nanodisc membrane system. The final goal was to analyse the system by SEIRA spectroscopy. Like other rhodopsins, the ChR II protein has seven transmembrane α -helices, and a retinal chromophore in its active site. The protein used in this work had a mutation in the position 128, where the cysteine residue was substituted by a serine (C128S). The mutation at this position leads to an extension of the channel open state lifetime of 10⁴-fold [40]. Reports of similar mutations showed that the equilibrium between the P390 and P520 states, closed and open channel respectively, can be controlled with blue and green light. As a starting point in the study of the ChR II C128S variant, UV-vis and FT-IR transmission experiments were performed to evaluate the photocycle of this mutant. These two techniques provided the necessary information to set the parameters for the characterisation of the nanodisc system with ChR II C128S by SEIRA spectroscopy.

The microbial rhodopsin ChR II rules the phototaxis of the green algae *Chlamydomonas reinhardtii*, and it is a light-gated cation channel. The potential of channelrhodopsins to control the depolarization of the cell membrane by light is widely used in optogenetics. Optogenetics is a technique based on the control of certain cells, usually neurons, using integrated light sensitive proteins. In view of its importance for biomedical applications, the molecular function of ChR II, including the photocycle and its intermediate states, has been extensively investigated. The present study builds upon previous work by Stehfest et al (2010) [47], by Berndt et al (2011) [48] and by Bruun et al (2015) [42].

In their study, Berndt and co-workers highlighted that the variant C128S presented the longest extension of the conducting state lifetime with 106 s versus 11.9 ms for the wild type. Additionally, this mutant showed up to 300-fold more sensitivity for light. The underlying hypothesis was based on the equilibrium between states, inspired by certain analogies to bacteriorhodopsin. The mutation of bR in the residue Threonine90 of the helix 3 slowed down the photocycle kinetics. This residue is well conserved and corresponds to C128 in ChR II. In both proteins, these amino acids are in close interaction with the retinal chromophore. Thus, it was concluded that the C128S mutant provoked controlled depolarization of the membrane in neurons after 10 ms of blue light (470 nm) illumination, which could be terminated by 50 ms of green light (530 nm). Furthermore, the study by Stehfest brought more clarity on the photocycle adapted by these mutants by focusing in the C128T and determining side reactions depending on

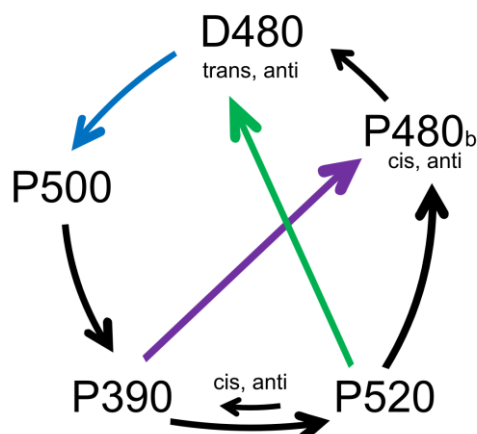


Figure 4.1. Schematic and simplified representation of the ChR II protein photocycle. Each state is named after the respective UV-vis maxima, and the D and P letters indicate dark or photo state, respectively. The blue and green arrows depict the transitions after illumination with blue and green light, and the purple arrow indicates the transition induced by UV light. The black of arrows represent the transition, equilibrium or decay of the different states. The preferential retinal chromophore conformations are indicated as well.

the illumination. The results obtained by Stehfest et al allowed them to postulate an alternative, yet more complex photocycle in comparison to the one described for the wild type. Bruun and coworkers demonstrated that low light intensities provoke equilibrium between two dark-adapted states (D480 and D470) in a ratio 3:1, also known as apparent dark-adapted state (DA_{app}), and they discussed the challenge that this equilibrium represents for the characterisation of the initial dark state (IDA) of ChR II by spectroscopic techniques. The equilibrium explained in Bruun's light-dark adaptation study is represented in a mirror photocycle for each DA state interconnected by the two DA states.

Figure 4.1 shows a simplified representation of the photocycle of C128 mutants of ChR II. The starting point is the D480 (DA) state. After blue light illumination, D480 is photoconverted to the P500 state, which rapidly decays to P390. The P390 state is photoactive, and it is in equilibrium with the open state P520. In this stage, it is possible to take a shortcut by illuminating with green light and transition to P480_b, which can decay back to D480 [47]. There is another shortcut to the P480_b by illumination of the P390 state with UV light. The prevailing conformations of the retinal chromophore in the DA and P390 states are also depicted in the figure.

4.1.1. UV-vis study of ChR II protein

Taking into account the information described above, a light-induced UV-vis spectroscopic analysis was performed with the ChR II C128S in solution (3 μ M). UV-vis allowed defining the different states of this mutant by identifying the maximum absorbance at each step. The DA state was recorded under red light to minimize other photoreactions. Figure 4.2A shows the spectra corresponding to the DA state (black

line), after 460 nm light illumination (blue line) and after 390 nm light illumination (purple line). The DA state has two intrinsic maxima vibronic side bands at 450 nm and 480 nm. The spectrum after blue light illumination (460 nm, blue line) showed one maximum at 390 nm that can be assigned to the P390 state, and residual absorption at 485 nm. The P500 state cannot be observed with this technique, since it does not accumulate [47]. From the difference between DA and P390 spectra, it is possible to see that the conversion is not complete. The transition after illumination with UV light (390 nm, purple line) presented a high conversion of the P390 species to a state with the maximum of absorbance at 485 nm (slightly red-shifted from the DA state), which corresponds to the P480_b state (see figure 4.2A).

Analysing the results obtained for the protein in solution, three distinct states were characterised: D480, P390 and P480_b. According to the recent detailed analysis of the dark state of ChR II [42], in the D480 state, the all-*trans*, *anti* conformation of the deprotonated Schiff base chromophore prevails (ca. 70%) whereas the remaining fraction is in the 13-*cis*, 15-*syn* configuration. Furthermore, the formation of the P390 state, associated with a double bond photoisomerisation and the subsequent deprotonation of the Schiff base linked to a tertiary structure change of the protein, corresponds to a yet closed channel. The last conversion, from P390 to DA state with maximum at 485 nm induced by UV light illumination, represented the return to the dark state via P480_b. Therefore, the studies in this work focused on the section of the photocycle involving the states D480, P500, P390 and P480_b (see figure 4.1).

The very similar illumination procedure was followed for the protein ChR II C128S embedded in the nanodisc system. The corresponding spectra are shown in figure 5.2B. The main differences were the lower intensity (especially in the DA state) and the absence of the 485 nm maximum. Besides that, the phototransitions in the nanodisc

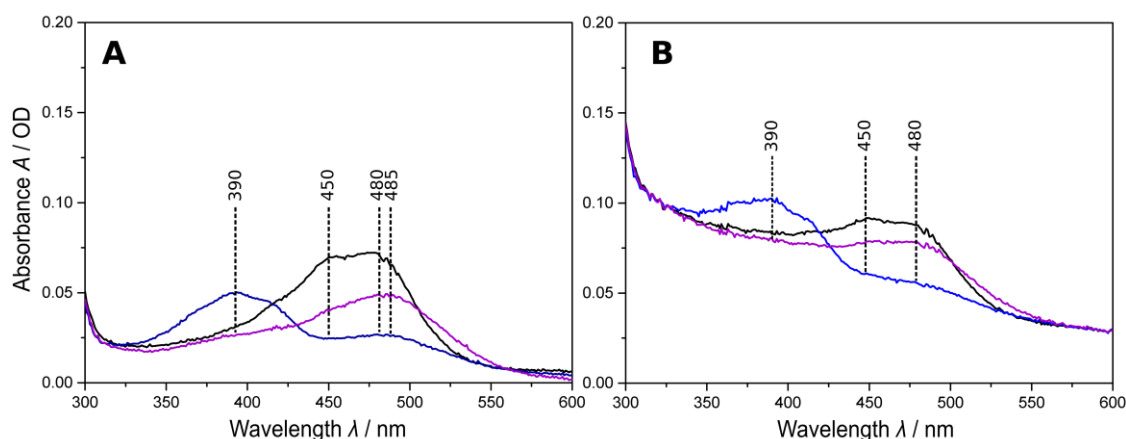


Figure 4.2. UV-vis spectra of ChR II C128S protein in solution **A** and embedded in the nanodisc system **B**. In both cases the samples concentration was of approximately 3 μM . The black line depicts the DA state measured under red light. The blue line represents the spectrum after illumination with 460 nm (blue) for 10 minutes and the purple line, the spectrum after illuminating with 390 nm light (UV) for 10 minutes. The maxima for each spectrum are indicated in the picture.

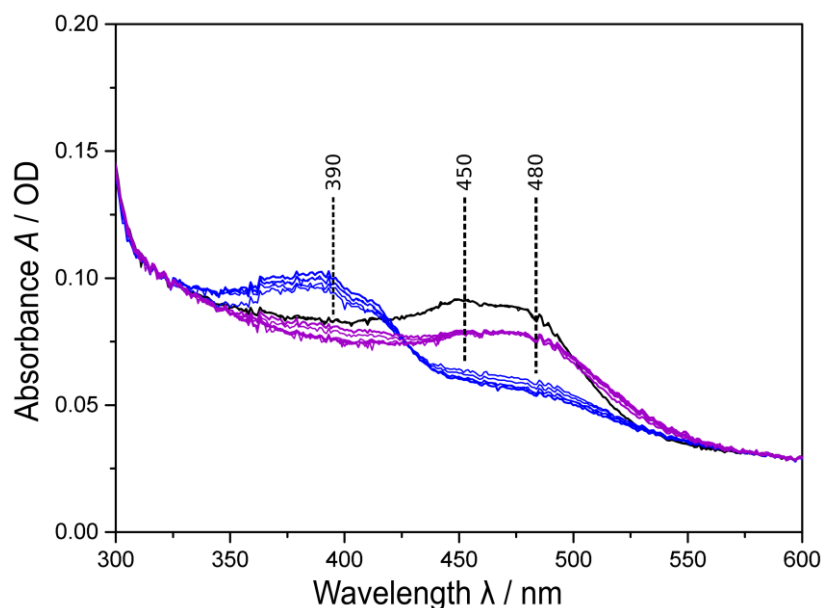


Figure 4.3. UV-vis spectra of the illumination cycles of ChR II C128S protein embedded in the nanodisc system. The black line depicts the spectrum of the DA state; the blue and the purple lines refer to the spectra obtained after illumination with 460 nm and 390 nm (UV), respectively. The maxima of each spectrum are indicated in the picture.

spectra were similar enough to assume that the protein behaves in the same way. The DA state presents two maxima at 450 nm and 480 nm, and a similar transition to the P390 state after illumination with blue light (460 nm). Moreover, the illumination with UV light (390 nm) yielded in the disappearance of the P390 state and the transition to the DA state with a maximum at 480 nm. Overall, these results support the main features of the nanodisc system; it not only offers a native-like environment for the protein, but also allows the organization and orientation of the protein in the membrane.

As mentioned before, the mutant C128S has shown reversible cycles between states controlled by light. Therefore, to evaluate this effect in the section of the photocycle studied here, an analysis on the reversibility of the states was performed with cycles of blue and UV light excitation of the ChR II C128S embedded in nanodisc systems (figure 4.3). The UV-vis spectra showed a higher conversion in the first cycle from the DA to the P390 state compared to the following steps. The reversible character with blue (460 nm) and UV light (390 nm) irradiation proved to convert approximately 60% of the species back and forth. This conversion needs to be higher in order to obtain a reasonable signal-to-noise ratio and to be able to visualise these changes in the IR light-induced difference spectrum. Nevertheless, this information is crucial for the structural characterisation of the different states by SEIRA spectroscopy. The protocol described above was used in the following experiments of the ChR II C128S in solution and embedded in the nanodisc system.

UV-vis spectroscopy: kinetics analysis of ChR II C128S in nanodisc system

Additionally, the UV-vis analysis allowed measuring the kinetics of the light-induced cycling between D480 and P390, monitoring the temporal evolution of the absorption at 480 nm maximum, induced by illumination with 460 nm (blue) light, and the recovery after the illumination.

The results were represented into two graphs, along with fits of exponential functions to the data (figure 4.4). In the first step, the sample was under red-light in the DA state and after one minute the 460 nm light was turned on. Graph A shows two processes. Firstly, there was a rapid transition represented by a steep decay (τ_1), indicating that after 12 ms 40% of the DA state has been converted. The second term of the equation denoted a slower transition with a τ_2 of 1.2 minutes. Figure 5.4B shows the recovery of the species at 480 nm with the blue light off. The recovery was evaluated under red light for approximately 1 hour. The equation for the recovery transition resulted in a τ_1 of 4 minutes.

The kinetic analysis provided important information about the transition time between these states. The results shown here suggest that the P390 state forms almost instantaneously in the beginning of the illumination and, after 3 minutes the curve reaches a plateau. On the contrary, the process of recovery of the dark state is much slower and it needs at least 4 minutes to transition to the dark state. Thus, these times were taken into account for the illumination protocol of the ChR II C128S protein.

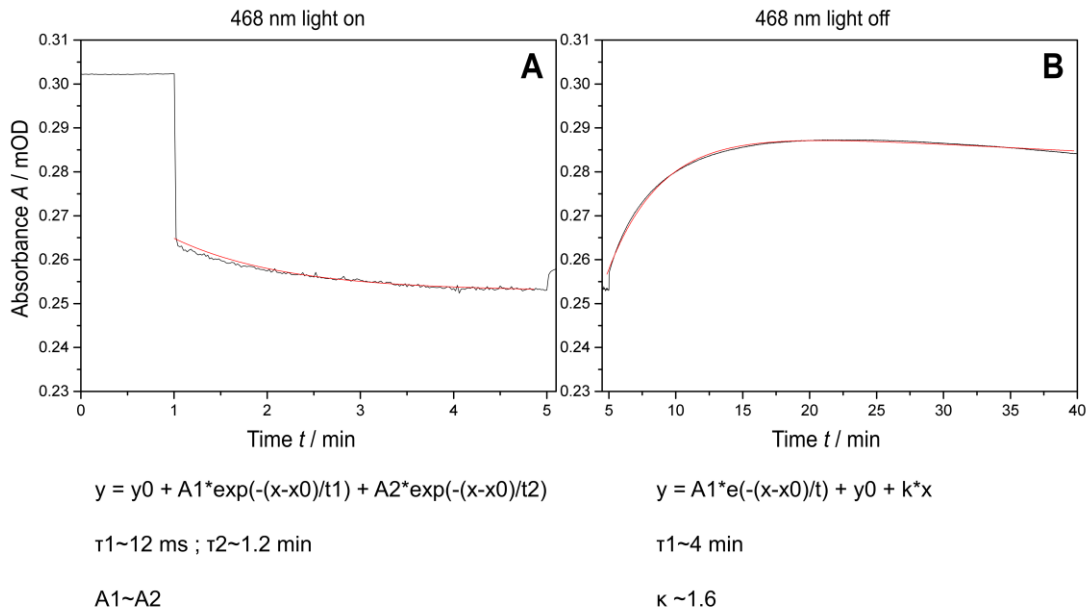


Figure 4.4. Kinetic representation for the evolution of the 480 nm species of the DA state. Graph **A** corresponds to the illumination with the 460 nm light, and graph **B** to the dark recovery phase after the illumination. Underneath each graph there are the respective fitting equations and parameters. The symbol τ represents the mean life time of the state; A and k are the function constants.

4.1.2. FT-IR transmission study of ChR II protein

FT-IR transmission spectroscopy of the ChR II C128S protein was performed in solution and embedded in the nanodisc system. This technique offered structural information of the system, which sets the basis for the SEIRA measurements. As in the UV-vis, the first step was to analyse the protein in solution, and to perform the illumination process described in the previous section. The same experiment was done with the protein embedded in the nanodisc system. Figure 4.5 shows the IR spectra of the ChR II C128S protein in solution (black line) and the protein in the nanodisc system (grey line). These FT-IR difference spectra correspond to the protein in the DA state, using the buffer spectrum as reference. The amide I band (mainly the C=O stretching mode) appeared at 1657 cm^{-1} and the amide II band (N-H bending and C-N stretching modes) at 1550 cm^{-1} . The band positions and the relative area ratio of ca. 3 of the amide I and II confirm the α -helical structure of the protein. The spectrum of the protein in the nanodisc (grey line) showed similar amide I and II bands, though higher intensities. The second derivative of the spectra (not shown) proved that the amide bands appeared at the same position in both cases. The difference in intensity may be attributed to the contribution of the scaffold protein of the nanodisc, which adopts an α -helical structure as well. The band at 1740 cm^{-1} in the grey spectrum corresponds to the CO vibration of the DMPC phospholipids in the nanodisc system. This band is actually an overlap between the ester groups and the carboxylic acid groups of the phospholipids at ca. 1740 cm^{-1} and at ca. 1730 cm^{-1} , respectively. These results indicate that the nanodisc system does not modify the protein secondary structure, maintaining its α -helical organization.

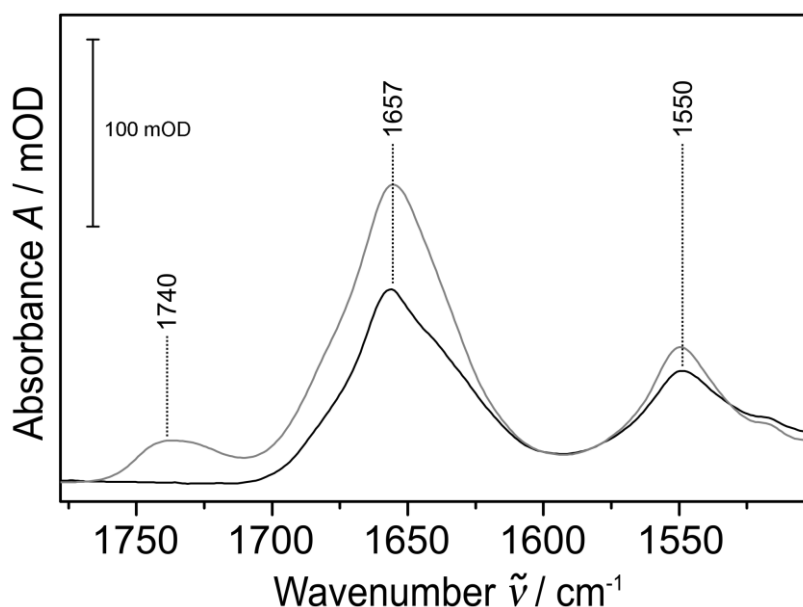


Figure 4.5. FT-IR spectra of the ChR II C128S protein in solution (black line), and embedded in the nanodisc system (grey line). The spectra correspond to the DA state of the protein measured under red light and at room temperature.

4.1.2.1. Illumination cycles of ChR II protein

The illumination protocol was applied to both cases: the protein in solution and the protein embedded in the nanodisc. The protocol was based on three phases that were repeated in five illumination cycles. The first stage was the transition from DA to the P390 state induced by the 460 nm (blue) light. After the formation of the P390 state, the sample was illuminated with UV light, and later it was let to rest under red light to achieve the DA state. From here, the cycle started again with the formation of the P390 state. Figure 4.6 offers a scheme of the illumination protocol to visualise the process. The whole illumination process was followed by FT-IR spectroscopy at room temperature (RT). Figure 4.7 and 4.8 show the spectra for the ChR II C128S protein after blue light and UV light illumination, respectively. The part A of each figure corresponds to the protein in solution, and the part B to the protein embedded in the nanodisc system. Figure 5.7 presents the 460 nm minus DA difference spectra and figure 5.8 the difference spectra between the 390 nm and 460 nm lights. The ChR II C128S mutant presented low reversibility for the evaluated photocycle section, which means that after the third conversion with the 460 nm light the changes were minimal (data not shown).

The first cycle (black line) showed the most significant difference between the spectra in figure 4.7. In this first cycle, the protein in solution showed a more prominent change than the protein in the nanodisc. Besides this, the protein displayed similar light induced

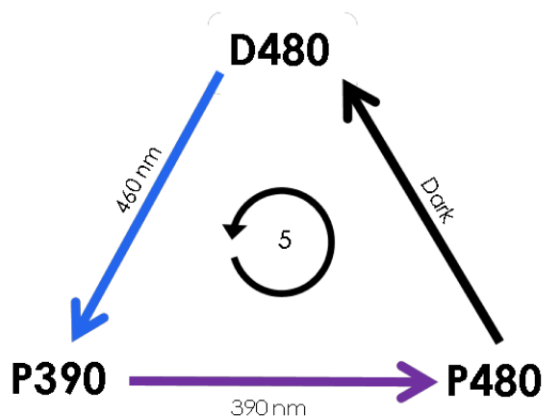


Figure 4.6. Schematic representation of the illumination protocol followed in the IR study of the ChR II C128S protein. D480, P390 and P480 are depicted as the main states involved in this cycle. The first step consisted of the illumination of the sample with the 460 nm blue light, and then with the UV light. Each illumination was performed for approximately ten minutes. Lastly, the protein was let ca. 30min to rest under red light to achieve the DA state before the new illumination cycle starts. There were performed five illumination cycles.

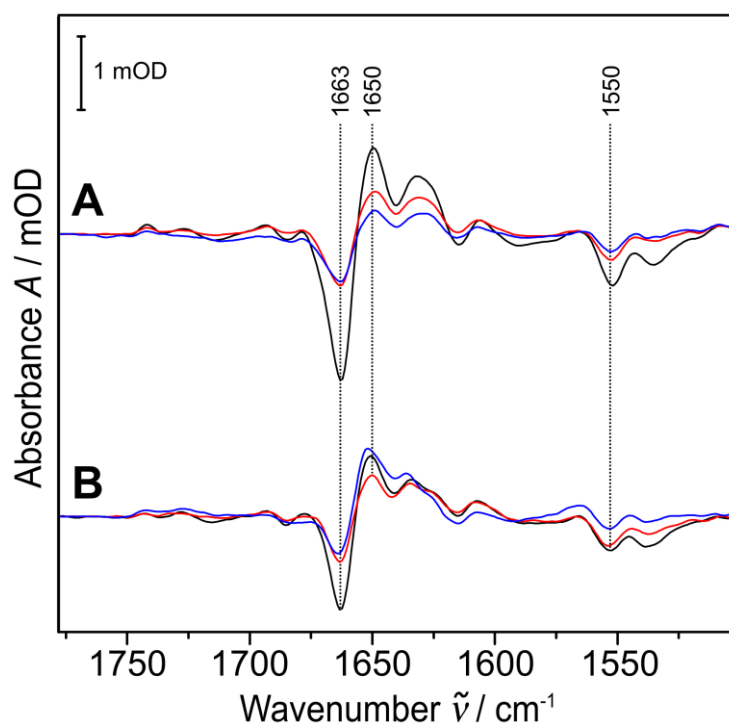


Figure 4.7. FT-IR transmission difference spectra of the ChR II C128S protein photoinduced transition from dark to P390 state after 460 nm (blue light) illumination. The DA state spectrum was used as reference. There are three cycles shown: first in black, second in red and third in blue. **A**: Spectra of the protein in solution. **B**: Spectra of the protein embedded in the nanodisc system.

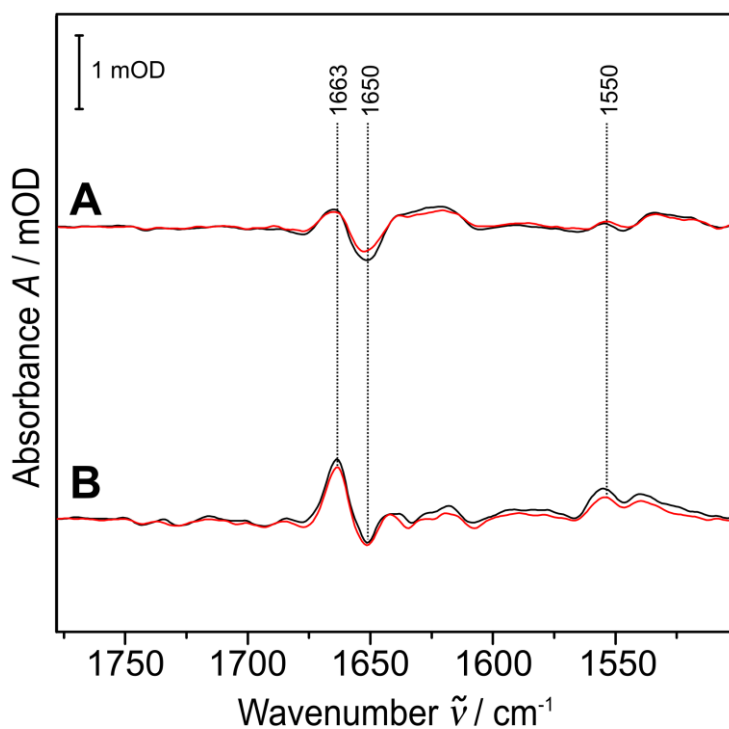


Figure 4.8. FT-IR transmission difference spectra of the ChR II C128S protein photoinduced transition from P390 to P480_b state after 390 nm (UV light) illumination. The P390 state spectrum was used as reference. There are shown two cycles: first in black and second in red. **A**: Spectra of the protein in solution. **B**: Spectra of the protein embedded in the nanodisc system.

structural changes in both cases for this transition step. The spectra revealed the most distinctive bands at (-) 1663 cm^{-1} and (+) 1650 cm^{-1} in the amide I region. There was a small variation in the amide II region at approximately (-) 1550 cm^{-1} . These spectra are characteristic of the P390 state formation, which is related to major structural changes in the protein backbone. This observation is in line with results in the literature with the C128T mutant [34] [47]. In the case of the protein in the nanodisc, the spectra showed the same behaviour than the protein in solution. A tentative explanation for the difference in intensity between the spectra in A and B for the first transition may be a lower percentage of the chromophore in the protein embedded in the nanodisc system.

Overall, the conversion to the P390 state was reproduced with the ChR II C128S mutant using the nanodisc system. This means that the function of the protein is not greatly affected by the nanodisc environment. The decrease in intensity between the black, red and blue spectra suggests a decay of the changes with the number of cycles. This decay, observed as well observed in the UV-vis spectra, limits the detection by IR transmission spectroscopy. This effect might be of stronger influence in SEIRA, which means that the higher the cycle number, the less probable to observe changes in the SEIRA difference spectrum. In figure 4.8, which presents the conversion from the P390 into a DA state, the spectra A showed smaller changes than graph B. Interestingly, comparing A and B, the band at (+) 1663 cm^{-1} is more defined in the spectra of the protein with the nanodisc. The characteristic bands appeared at the same positions as in figure 4.7, but less intense and inversed sign. The decay between cycles was also present in this transition, which allowed observing changes only until the second cycle.

To conclude this section, it was possible to observe analogous structural changes of the protein in solution and embedded in the nanodisc system. Nevertheless, slight differences in intensities were observed between ChR II C128S in solution and integrated in the nanodisc. Similar conclusions were drawn from the UV-vis conversion analysis. This fact might influence the SEIRA experiments in terms of intensity: the lesser intensity of changes between the transitions, the less probable their observation by SEIRA spectroscopy. Even though three cycles were the maximum to distinguish changes in IR transmission, the illumination protocol proved to be effective enough to differentiate the states. Therefore, this protocol using 460 nm (blue) and 390 nm (UV) irradiation was applied to the ChR II C128S protein embedded in the nanodisc analysed by SEIRA spectroscopy.

4.1.3. Spectroelectrochemical study of Ni-NTA monolayers

This subsection presents the comparison of two SAMs for the optimisation of the Ni-NTA monolayer to the anchor His-tagged nanodisc system. The results are presented in three parts. First, there is the SEIRA spectroscopic evaluation of the NTA SAM versus a mixed SAM of NTA and 3MP. The second part shows the EIS analysis of the respective SAMs. And the last part provides the results from the Ni^{2+} coordination of the NTA in the two

SAMs. The information obtained from this subsection allows determining the optimal conditions for the proper assembly and stability of the final system.

SEIRA spectroscopy of NTA monolayers.

The assembly of a proper self-assembled monolayer (SAM) is crucial for the immobilization of His-tagged systems like the nanodisc. Therefore, the first stage of this SEIRA study consisted in the optimization of the SAM. In the literature, it has been shown that the nitrilotriacetic acid (NTA) is the molecule of choice to anchor His-tagged systems. The NTA molecule can resemble a trident fork with eight atoms in its backbone. Despite the high affinity of NTA for this system, a mixed SAM may offer advantages in terms of charge distribution and accessibility [104] [105] [106]. For this reason, two different scenarios were tested: pure NTA SAM and a mixture of NTA with 3-mercaptopropanol (3MP).

The pure NTA SAM spectrum (see figure 4.9) shows an intense band at 1740 cm^{-1} that corresponds to the CO stretching vibration of the protonated carboxylic groups. The bands at 1606 cm^{-1} and 1403 cm^{-1} are assigned to the COO^- stretching vibrations of the asymmetric and symmetric deprotonated carboxylic groups, respectively. The fact that the immobilization was carried out at pH 5.5 may explain the mix of protonated and deprotonated carboxylic species. Another important band appears at 1553 cm^{-1} , which is the C-N stretching vibration coupled to the N-H bending of the carboxamide group (amide II) of NTA. The bands in the lower frequency region are assigned to the C-H bending and rocking of the molecule backbone. The band at 1432 cm^{-1} is an

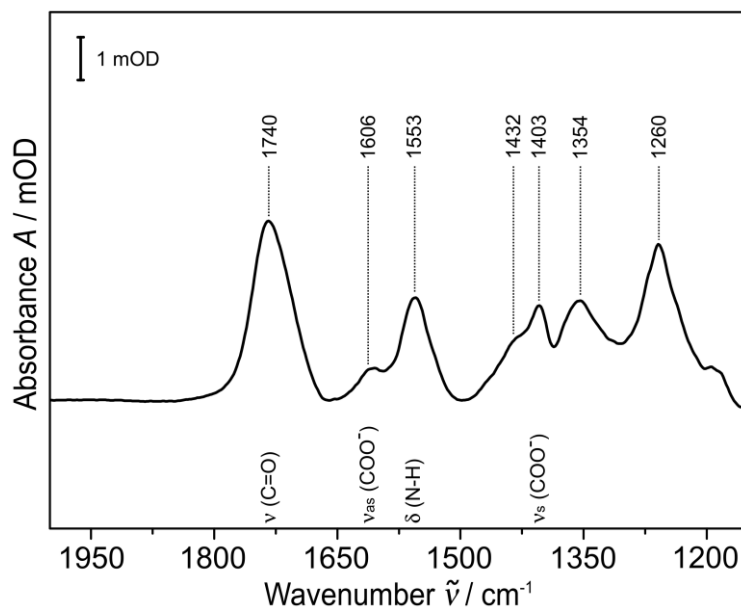


Figure 4.9. SEIRA difference spectrum of the NTA SAM after overnight incubation at 4°C minus the spectrum of the Au-film. The relevant modes of the NTA molecule are depicted in the spectrum as: ν stretching and δ bending. The denominations *s* and *as* correspond to the symmetric and asymmetric vibrations, respectively. The C=O band is assigned to the protonated carboxylic groups, while the COO^- bands correspond to the deprotonated carboxylic groups. The N-H corresponds to the vibration in the carboxamide group of the molecule. The immobilization was carried out at pH 5.5.

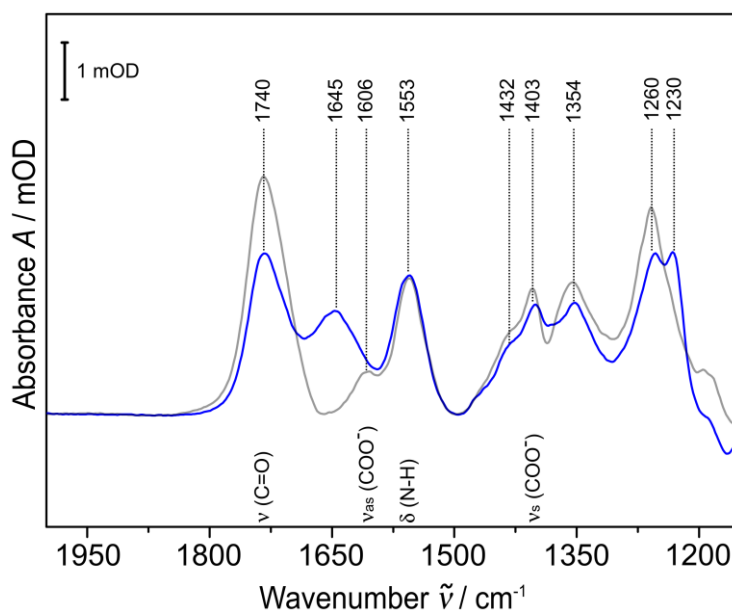


Figure 4.10. SEIRA difference spectrum of the NTA-3MP mixed SAM after overnight incubation at 4° C minus the spectrum of the Au-film. In grey there is the spectrum of the NTA SAM for comparison. The relevant modes of the NTA molecule are depicted in the spectrum as: ν stretching and δ bending. The denominations *s* and *as* correspond to the symmetric and asymmetric vibrations, respectively. The C=O band is assigned to the protonated carboxylic groups, while the COO⁻ bands correspond to the deprotonated carboxylic groups. The N-H corresponds to the vibration in the carboxamide group of the molecule. The immobilization was carried out at pH 5.5.

overlap of the C-H bending and a symmetric stretching of the COO⁻. At 1354 cm⁻¹ there is a broad band corresponding to the hydrogen bond bending of carboxylate groups. Overall, the spectrum displays intense bands and presents minimal changes in intensities after washing off the excess of NTA. The band positions confirm the formation of the NTA SAM on the Au-film surface [87] [107] [83].

The mixed SAM was prepared aiming a ratio of 80:20 of NTA to 3MP. The SEIRA difference spectrum is shown in figure 4.10 (blue spectrum). There are slight changes compared to the pure NTA SAM spectrum. The main difference is the broad band at 1645 cm⁻¹ that overlaps and hides the 1606 cm⁻¹ band of the carboxylate groups from NTA. Water can find its way through when having a mixed SAM, which results in a broad -OH band, at 1645 cm⁻¹. In the spectrum of the pure NTA the important bands are of higher intensity than in the mixed SAM. This can be explained by the lower percentage of NTA molecules contributing to the different vibrational modes.

EIS spectroscopy analysis of NTA monolayers.

EIS spectroscopy was performed to evaluate the SAM-coated electrode. For the analysis of the quality of the SAMs, the data was represented in a Cole-Cole plot. The spectra in Figure 4.11 correspond to the pure NTA, pure 3MP and mixed SAM. All spectra show only one semicircle, which means there is one region defined by the NTA and/or 3MP molecules and another one by the solution on top. The lower capacitance in the NTA spectrum is the result of a thicker layer with a higher resistance. The fact that the mixed SAM spectrum was more similar to the 3MP than to the NTA might point out a

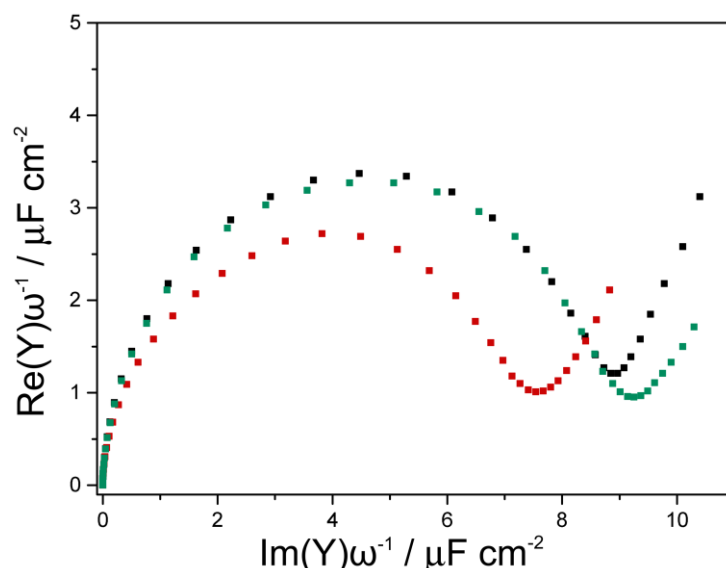


Figure 4.11. EIS spectra of the NTA (red), 3MP (black) and 80:20 NTA:3MP mixed (turquoise) SAMs. The data is presented in a Cole-Cole plot.

poorer quality of the mixed monolayer, since 3MP can introduce defects into the SAM. For the analysis, a $R_{\text{solvent}}(R_{\text{monolayer}} \cdot C_{\text{monolayer}})Q$ circuit was employed. This circuit involves a constant phase element (CPE) used for non-ideal capacitive behaviour (section 2.5.3). The parameters obtained from the fitting are presented in table 4.1.

Table 4.1. EIS information obtained from the fitting of the NTA, 3MP and mixed SAMs data using the equivalent circuit $R_{\text{solvent}}(R_{\text{monolayer}} \cdot C_{\text{monolayer}})Q$.

SAM	R_{solvent} Ω	$R_{\text{monolayer}}$ $k\Omega \text{ cm}^2$	C_{solvent} $\mu\text{F cm}^{-2}$	Q	α
NTA	475	898	15.3	$1.25 \cdot 10^{-4}$	0.60
3MP	722	642	16.8	$1.21 \cdot 10^{-4}$	0.64
NTA-3MP	354	$1.17 \cdot 10^3$	16.9	$2.18 \cdot 10^{-4}$	0.55

The α value gets closer to 0.5 in the mixed SAM than NTA alone. The $\alpha \sim 0.5$ represents the Warburg impedance resulting from the diffusive process of ions within the SAM. A tentative interpretation is that the mixed SAM permits an easier diffusion of water and ions through the monolayer than the pure SAMs. The experiments with NTA showed a higher reproducibility in both SEIRA and EIS.

SEIRA spectroscopy of the Ni-NTA system.

In this sophisticated construction, there is a necessary ingredient to facilitate the immobilization of the nanodisc, the nickel ion (Ni^{2+}). This ion forms a complex with the carboxylate groups and the N-atom of the NTA, and with the N-atoms of the His-tags of the nanodisc. After addition of the nanodisc with the His-tag, the Ni^{2+} experiences a coordination change that stabilizes the system (see figure 3.12 materials and methods).

For this reaction, the Ni^{2+} was incubated for at least two hours to ensure the complexation of the ion with the carboxylate groups of the NTA. The spectrum in figure 4.12 shows the changes of NTA when complexing the Ni^{2+} ion using a pure NTA SAM (black line) and a mixed SAM (blue line). The bands at 1591 cm^{-1} and at 1416 cm^{-1} are characteristic bands that confirm the complexation of the NTA with the Ni^{2+} ion. These bands correspond to the asymmetric and symmetric stretching of the carboxylate groups, respectively. The band at 1740 cm^{-1} assigned to the protonated carboxylic species disappeared. The intense and broad band at 1591 cm^{-1} overlaps with the N-H band at 1553 cm^{-1} . Additionally, the band at 1453 cm^{-1} corresponds to the C-H bending mode.

The spectrum of the mixed SAM complexation of the Ni^{2+} ion is the blue spectrum in figure 4.12. This spectrum shows bands at the same positions as in the pure NTA SAM. The lower NTA percentage on the metal surface corresponds to the lower intensity in the spectrum of the mixed SAM. Even though the mixed SAM spectrum appears more defined, the NTA SAM provided more reproducible spectra. In many cases, there was bulk water leaking through the monolayer of the mixed SAM, resulting in a broad water band at ca. 1650 cm^{-1} . Therefore, the pure NTA SAM was used for the subsequent experiments due to a reduced interference of the water band that overlaps with bands of the target protein, and ensures a higher reproducibility.

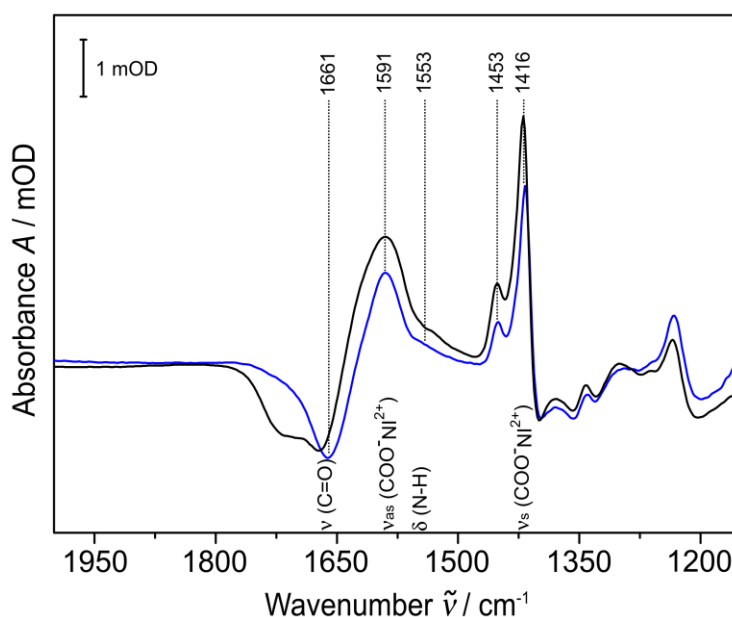


Figure 4.12. SEIRA difference spectra of the NTA complexation with Ni^{2+} ion. The black and blue spectra correspond to the NTA and the mixed SAM, respectively. Both spectra show the characteristic bands of the Ni^{2+} coordinated by the carboxylate groups of the NTA molecule. The relevant modes are depicted in the spectra as: ν stretching and δ bending. The denominations *s* and *as* correspond to the symmetric and asymmetric vibrations, respectively. The C=O band is assigned to the protonated carboxylic groups, and the COO^- bands correspond to the deprotonated carboxylic groups that coordinate the Ni^{2+} ion. The N-H corresponds to the vibration in the carboxamide group of the molecule. The complexation reaction was carried out at pH 5.5.

4.1.4. SEIRA study of the ChR II C128S protein in nanodisc systems

The scaffold protein of the nanodisc has a His-tagged tail that allows binding to the Ni-NTA SAM. After changing to pH 8, the imidazole groups from the His amino acids bind to the Ni^{2+} ions. In this way, the Ni^{2+} ion remains packed between the NTA and the His-tag, anchoring the nanodisc system to the surface. The spectrum measured after the incubation is shown in figure 4.13. The amide I (mainly the C=O stretching of the protein backbone) and amide II (predominantly the N-H bending and C-N stretching) bands confirmed a successful immobilization of the nanodisc system. The amide I appears at 1653 cm^{-1} and the amide II at 1550 cm^{-1} , these bands are characteristic of the α -helix structures. The broad bands might correspond to the contribution of the scaffold protein, which is also an α -helix. The bands between 3000 and 2850 cm^{-1} and at 1740 cm^{-1} are distinctive for the (CH_n) stretching and the CO stretching modes of the lipids, respectively. The asymmetric and symmetric stretching vibrations of the aliphatic chains of the DMPC lipids are observed at 2958 and 2871 cm^{-1} for the $-\text{CH}_3$ and at 2921 and 2852 cm^{-1} for the $-\text{CH}_2$. In figure 4.13, the binding process is illustrated at different time points. The intensity of the spectrum changed only slightly after washing away the excess of nanodisc in solution.

In the SEIRA spectrum, the amide I band is down-shifted compared to the FT-IR transmission measurements (1657 cm^{-1}). The oriented immobilization in SEIRA explains not only this slight-shift in the amide I, but more importantly the difference of the amide I/II band ratio. By area, the amide I/II ratio was 1.18 in SEIRA and 3.74 in FT-IR transmission. The FT-IR transmission measurements offered an orientation average of the bands in solution, while in SEIRA the protein bands and the nanodisc have a restricted orientation due to the immobilization of the system. Zaitseva and co-workers suggested an angle of about 24° between the horizontal plane of the nanodisc and the metal surface, using a Ni-NTA SAM [14]. In an α -helix, the amide I mode is oriented parallel to the helix axis and perpendicular to the amide II mode. As a result, the amide I and II modes are enhanced similarly in SEIRA with an angle of ca. 60° with respect to the normal of the Au surface. Thus, this explains that the ratio between the two bands was close to 1. It is worth noticing the contribution of the scaffold protein in the SEIRA and FT-IR transmission spectra. The bands that correspond to the lipid patch were characterised by SEIRA as well. The CO vibration from the lipid head groups appears at the same position as in the IR transmission experiment.

Overall, the spectrum obtained by SEIRA presents the characterisation of the nanodisc system containing the membrane protein. The secondary structure of the ChR II protein with seven transmembrane α -helices was conserved when incorporated into the nanodisc system. These results show the potential of this membrane system, which allows the identification of its composition and the target protein.

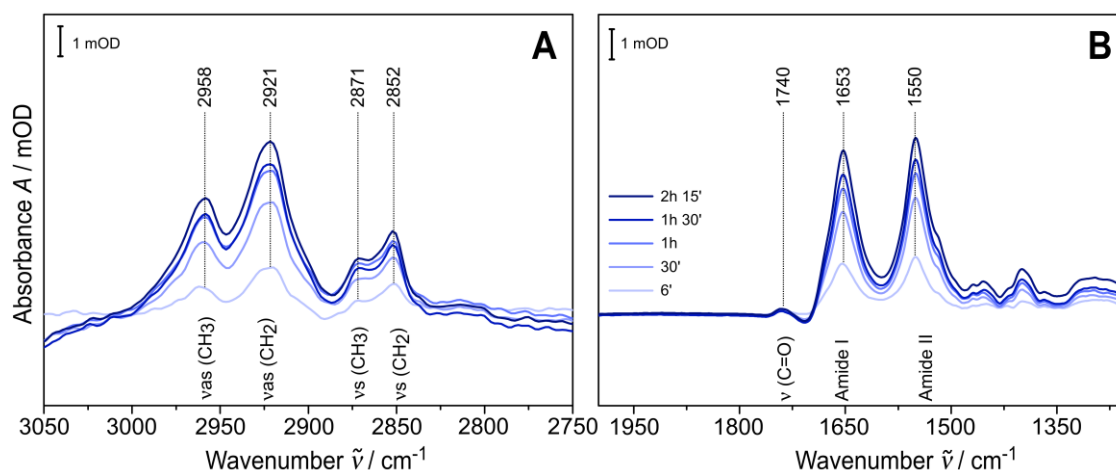


Figure 4.13. SEIRA difference spectra of the immobilization of the ChR II C128S protein embedded in the nanodisc system. The spectrum of the previous step (Ni^{2+} -NTA) was used as reference. **A:** (CH_n) stretching band region, which reveals the contribution of the lipid in the nanodisc. **B:** CO band corresponding to the lipids, as well as the amide I and amide II bands corresponding to the ChR II C128S protein. In both cases, the different shades of blue represent the evolution of the incubation over time. The nanodisc binding reaction was carried out at pH 8.8.

Light-induced SEIRA study of the ChR II C128S protein in nanodisc system

The illumination process was performed following the same protocol applied in the UV-vis and FT-IR transmission measurements. Figure 4.14 shows the changes corresponding to the first transition from the DA to the P390 state probed by SEIRA and FT-IR spectroscopy. The IR transmission spectrum (B) was described in section 4.1.2, using the DA state as reference. In the SEIRA experiments there were five cycles recorded as well, involving the 460 nm, 390 nm, and dark resting period (see figure 5.6). Following this protocol, it was possible to obtain the same changes observed in FT-IR transmission spectroscopy. Even though the intensity of the changes was 100 times lower in the case of SEIRA, the two spectra showed similar band-shape and positions. The first transition in SEIRA presented the most significant changes in the amide I region at $(-)$ 1664 cm^{-1} and $(+)$ 1653 cm^{-1} , which were assigned to the structural changes in the backbone of the retinal protein. The rest of the conversions presented minimal changes that could not be distinguished from the noise.

The short-range restriction in SEIRA spectroscopy, which permits enhancement of the modes close to the surface, may explain the lower intensity of the transition spectrum in SEIRA compared to the transmission results. Even so, the assembly of the nanodisc system containing the membrane protein ChR II C128S was successful, and it was possible to observe the photo-transition of the light-sensitive channel as well.

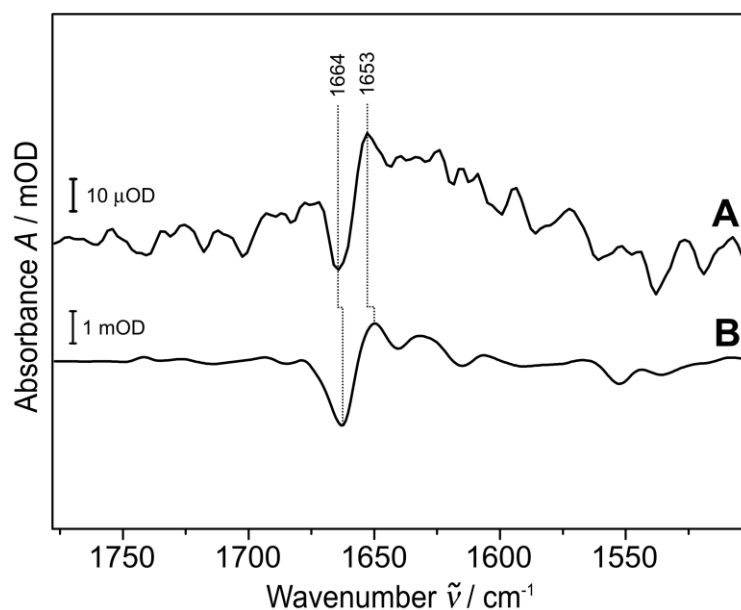


Figure 4.14. **A**: SEIRA difference spectrum of the first illumination transition from DA to P390 state with the 460 nm (blue) light of the ChR II C128S protein embedded into the nanodisc system. **B**: FT-IR transmission spectrum of the same first transition after illumination with the blue (460 nm) light. There was a 100 fold absorbance difference between spectra **A** and **B**.

4.1.5 Conclusions

EIS and SEIRA spectroscopy were used to characterise and optimise the Ni-NTA SAM. This monolayer served to anchor the nanodisc membrane system embedding the ChR II C128S light-sensitive protein. It was possible to observe the transition from the DA to the P390 state of the protein by SEIRA spectroscopy. However, the rest of the reactions involved in the illumination process did not have significant impact in the corresponding spectra. The spectra obtained in both FT-IR and SEIRA experiments were similar to the spectra described in the literature [34] [42] [47]. However, the yield of the reactions seems to decrease with the cycle number, decreasing as well the probability to detect these changes. This decrease is reflected in the intensity of the transition spectra observed by FT-IR transmission and UV-vis, and even more critical in SEIRA.

UV-vis and FT-IR transmission measurements offered supporting information for the interpretation and understanding of the results obtained by SEIRA. UV-vis provided the identification of the different states involved in the portion of the ChR II C128S photocycle analysed here. Moreover, the FT-IR transmission spectroscopy allowed the structural evaluation of the mutant and its photo-induced changes. Both techniques served to evaluate the protein in solution and embedded in the nanodisc membrane system. This comparison demonstrated that the protein structure and function were not greatly affected when inserted in the nanodisc system. These findings confirm the relevance of nanodisc membrane systems to investigate transmembrane proteins by SEIRA spectroscopy. This study sets a base for future improvements for applications of this system to similar targets.

4.2. Characterisation study of enniatin B

This section presents the results of the structural study of the AMP enniatin B (EB) and its interaction with the POPC membrane systems. Enniatins are depsipeptide⁴ produced by various species of *Fusarium* fungi, though *Fusarium Scripi* preferably makes EB. The antimicrobial activity of enniatins has been proven against a wide range of diseases, like cancer and respiratory infections [70]. Even though most of the studies suggest a membrane-active mechanism of action, details are yet not known. The isopropyl residues and methylated amide nitrogens render this cyclodepsipeptide highly hydrophobic, which indicates it can easily diffuse through the cell membrane. Due to its circular shape, EB can form ion complexes with mono and divalent ions creating ion-transporters within lipid bilayers.

Mueller and Rudin (1967) provided the first evidence of the membrane interaction of enniatins and other depsipeptides, by monitoring the increase in conductance through a bimolecular lipid membrane in presence of Na⁺ and K⁺ ion-solutions [108]. Ovchinnikov et al. (1974) offered a model for the conformation as well as stoichiometry of the different ion-complexes [61]. They suggested a difference in the C=O ligands contribution depending on the EB:ion complex stoichiometry. While for the 1:1 and 3:2 ratios both CO and amide I ligands coordinate the ion/s, for the 2:1 ratio the amide I ligands are pointing inwards forming a sandwich with the central ion. Accordingly, and taking into account the ion size, they proposed that Na⁺ and K⁺ form a 2:1 complex and Cs⁺ with bigger radii would form a 3:2 complex. The results obtained from the patch-clamp study by Kamyar et al 30 years later [76], led to a similar conclusion for the complexes stoichiometry extending it to the evaluation with divalent ions and suggesting a cation selectivity order for EB according to K⁺>Ca²⁺≥Na⁺>Mg²⁺>Li⁺. Interestingly and against expectations, IR spectra of EB in absence and presence of different ions show very similar position of the CO and amide absorptions at 1746-1744 cm⁻¹ and 1666-1665 cm⁻¹ [61]. This contrary to results found for beauvericin, valinomycin, and other peptides like gramicidin A [61], and suggests that either these normal modes are insensitive to the interaction with different ions or that only a fraction of EB formed complexes.

The advantage of this project is that it presents a method combining the tBLM system with SEIRA spectroscopy to evaluate the peptide structure in a membrane-mimetic environment. The main goal of this work was to address the following questions: i) Does EB incorporate into membrane systems? Is it an ion carrier? ii) What is the structure and stoichiometry of EB:ion complexes? iii) What is EB binding mechanism to ions and to membranes? The diversity of methods employed here are essential to complement the SEIRA results, and offer valuable information about the EB-membrane and ion interaction. The results are presented with focus on the questions. First, the characterisation of the POPC tBLM system by EIS and SEIRA spectroscopy is shown,

⁴ Depsipeptides are peptides that have one or more amide groups substituted by an ester group.

together with the analysis of the membrane incorporation of EB. Then, the results of the ion-exchange process in tBLMs and theoretical calculations of the respective ion complexes will be presented, as well as a critical discussion of the related findings from literature. Lastly, there will be an evaluation of the kinetics of EB membrane binding and ion-exchange processes, using the data from the SEIRA measurements. This last part offers supplementary information that support the structural models proposed in this work, in addition to an evaluation of EB mobility within the membrane. The collection of conclusions obtained in this study is presented in the summary at the end of the section.

4.2.1. Incorporation of enniatin B into tBLM system

This study shows for the first time the structural characterization of EB by SEIRA spectroscopy using a POPC tBLM system. The beginning of this subsection describes the results of the step-by-step construction of the planar membrane systems. The evaluation of the tBLM system is followed by the independent incubation of EB in presence of three metal ions. From literature [109] it is known that EB can form complexes of different stoichiometry with several mono and divalent ions. Here, the ion complex formation of EB with Na, K and Cs are characterised by SEIRA spectroscopy. All three metals belong to the alkali metals group and form monovalent positive ions. The size of the ion increases when going down in the group, from Na⁺ to K⁺ and then, Cs⁺. This increase in the ion radii is considered one of the features for EB to form either 1:1, 2:1 or 3:2 EB:ion complexes [61]. The independent incubation of the complexes shall be taken in consideration for the discussion offered in the following subsection.

4.2.1.1. EIS of POPC membrane systems

The construction of the tBLM composed of areas of lipid bilayers requires a mixed SAM to anchor the system. The tBLM has advantages in comparison to other membrane systems. The most significant ones are the covalent immobilization of the tBLM on a Au-electrode, which increases its mechanical stability considerably, and at the same time provides space for an aqueous reservoir between the membrane and the electrode. This construct is bound to the surface of the nanostructured Au-film using tether molecules, which allows investigating the system by SEIRA and EIS spectroscopy. The tBLM used in this study contains the WK3SH tethered-cholesterol molecule and POPC zwitterionic lipids, which assures minimal spectral overlap with the EB normal modes of interest.

The first step consisted in optimizing the mixed SAM to form hydrophilic and hydrophobic islands on the Au-film surface. The tethered cholesterol molecule WK3SH formed the hydrophobic parts, and the 6MH formed the hydrophilic parts, which facilitate the formation of the aqueous reservoir beneath the lipids. The SAM was prepared to aim 80% of WK3SH and 20% of 6MH molecules on the surface of the Au according to Wiebalck et al. (2016) [29]. The EIS offers an analysis in terms of quality of the tBLM construct, which in this kind of system can prove whether or not the SAM and

the lipid bilayer are formed. The approach using EIS to evaluate the tBLM system is based on former work developed by Jeuken (2007) [9]. For this project, the capacitance of the system was determined by reading out the diameter of the first semicircle in the Cole-Cole plot (see figure 4.15). The capacitance of the mixed SAM can be expressed as a molar fraction relationship of the capacitances of the pure monolayers. Figure 4.15 top shows the EIS spectra of the WK3SH and 6MH pure monolayers assembled on a nanostructured Au-film. The capacitances determined for each monolayer are $(0.94 \pm 0.13) \mu\text{F cm}^{-2}$ for WK3SH and $(3.51 \pm 0.23) \mu\text{F cm}^{-2}$ for 6MH. Accordingly, the SAM spectrum (black) depicted in figure 4.15 bottom indicates a total capacitance (C_{SAM}) of $(1.28 \pm 0.01) \mu\text{F cm}^{-2}$. Taking into account the capacitances of the pure SAMs, the total capacitance of the system can be represented as follow:

$$C_{\text{SAM}} = X_{\text{WK3SH}}C_{\text{WK3SH}} + X_{\text{6MH}}C_{\text{6MH}} \quad (4.1)$$

where X and C are the respective molar fraction and capacitance for each monolayer. In this equation, it is possible to determine X_{WK3SH} and estimate the surface fraction of the cholesterol-tethered molecule. Thereby, it is possible to control the ratio of both SAM molecules at each experiment. As shown in previous work by our group and Jeuken (2006), the assembly of these molecules on the metal surface leads to a phase separated SAM with islands of WK3SH and islands of 6MH. This phase separation is based on the hydrophobicity of the C6-chain of 6MH and the hydrophilicity of the triethylene glycol linker $[-(\text{CH}_2-\text{CH}_2-\text{O})_3-]$ of WK3SH, so that under selected conditions a cooperative binding behaviour at the Au-electrode is observed [9] [29].

After the addition of the vesicles, the capacitance of the system decreased to $(0.62 \pm 0.03) \mu\text{F cm}^{-2}$ for the POPC tBLM (red spectrum figure 4.15 bottom). The decrease of the capacitance is a marker for the tBLM formation due to an increase of the thickness of layers on the surface of the electrode. This membrane construct is represented by the equivalent circuit $R_{\text{Solvent}}(R_{\text{Spacer}}C_{\text{Spacer}})(R_{\text{bilayer}}C_{\text{bilayer}})Q$ introduced in section 2.5.3. The fitting of this circuit to the data, allowed calculating the physical parameters shown in table 4.2. The C_{system} refers to the C_{SAM} in the case of pure WK3SH, pure 6MH and mixed monolayers, and to C_{tBLM} in the case of the mixed SAM with the lipids. The capacitor Q describes the non-ideal electrical behaviour of the system.

Since this circuit has been well described by Wiebalck et al. (2016) [29], only the parameters relevant for the quality of the different steps are discussed, i.e. the difference in the measured capacitance values respective to each step. This study uses the results as a proof of the proper assembly of the system on the surface of the electrode.

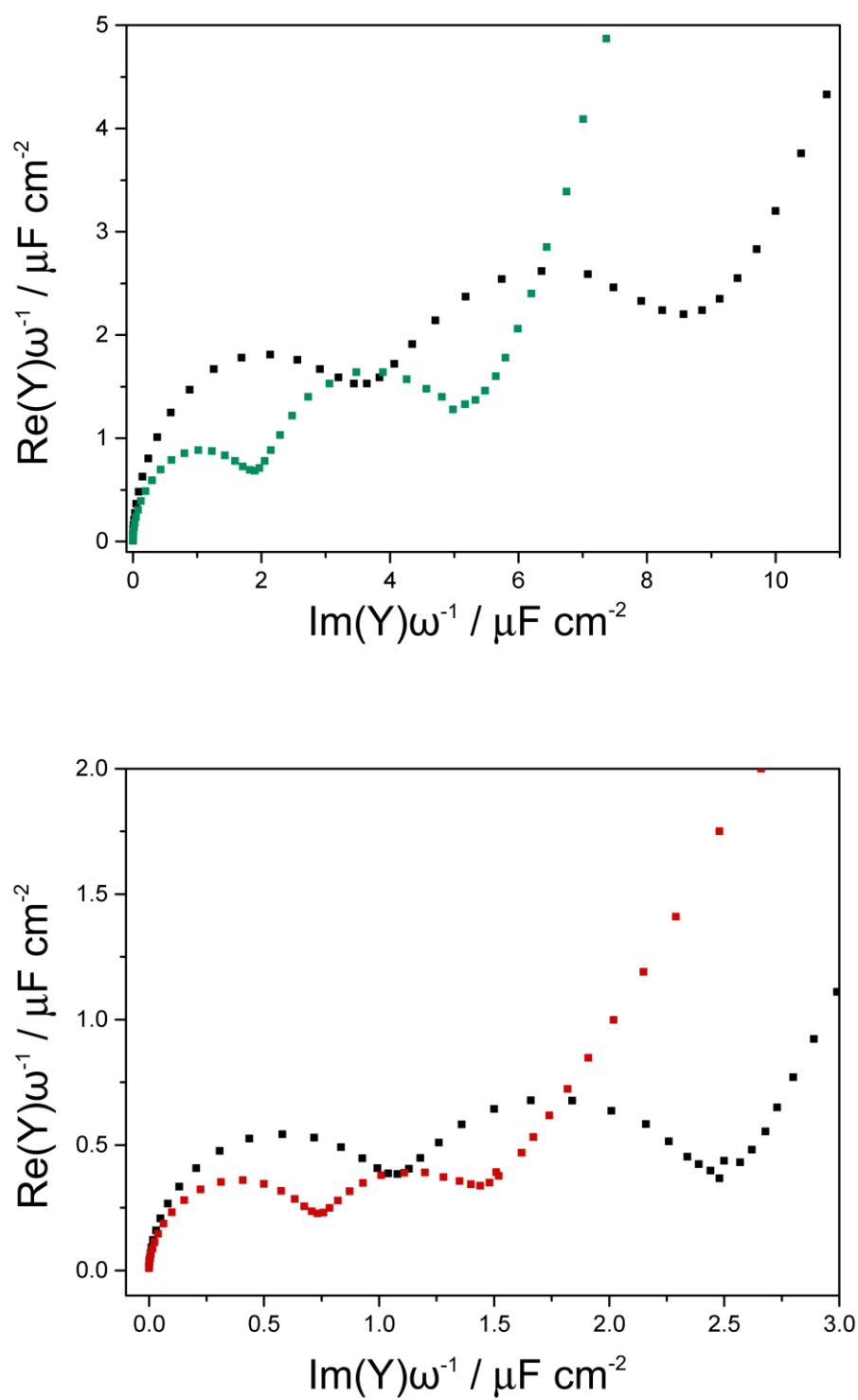


Figure 4.15. Impedance spectra represented in Cole-Cole plots for top: full WK3SH (turquoise) and full 6MH (black) monolayers, and bottom: mixed SAM (black) and tBLM system (red) after addition of the lipid vesicles.

Table 4.2. Results from the EIS analysis obtained by the fitting of the spectra to the equivalent circuit described for the full monolayers, SAM and the tBLM system.

	R_{solvent} Ω	R_{bilayer} $k\Omega \text{ cm}^2$	C_{bilayer} $\mu\text{F cm}^{-2}$	R_{spacer} $k\Omega \text{ cm}^2$	C_{spacer} $\mu\text{F cm}^{-2}$	Q $\mu\text{F s}^{\alpha-1} \text{ cm}^{-2}$	α	C_{system} $\mu\text{F cm}^{-2}$
6MH	184.6	1.34	13.93	192.79	18.81	21.23	0.82	3.51
WK3SH	219.9	5.30	2.35	364.96	4.32	12.99	0.79	0.94
SAM	266.7	2.21	5.03	483.13	6.55	9.97	0.82	1.28
tBLM	170.1	1.57	1.12	389.03	2.34	3.65	0.83	0.62

The POPC tethered hybrid lipid membrane

The tethered hybrid lipid membrane (tHLM) system was built in similar step-wise procedure as the tBLM, but instead of using a mixed SAM it uses a pure WK3SH monolayer. Consequently, the vesicles formed a lipid monolayer on top of the cholesterol SAM.

The impedance spectra of the pure WK3SH SAM (turquoise) and the tHLM (purple) are shown in figure 4.16. The interpretation used for the tBLM applies as well to the tHLM, therefore, the same equivalent circuit is used to obtain the physical parameters that describe the system (see table 4.3). The tHLM shows a capacitance of $(0.70 \pm 0.06) \mu\text{F cm}^{-2}$ slightly higher than the tBLM construct. The small difference between these capacitance values might be assigned to an altered effective dielectric constant and thickness of the tHLM due to the lack of the 6MH islands and the water reservoir. The results of both membrane systems were reproduced several times and are a proof of the robustness of the system.

Table 4.3. Results from the EIS analysis obtained by the fitting of the spectra to the equivalent circuit described for the full WK3SH monolayer and the tHLM system.

	R_{solvent} Ω	R_{spacer} $k\Omega \text{ cm}^2$	C_{spacer} $\mu\text{F cm}^{-2}$	R_{bilayer} $k\Omega \text{ cm}^2$	C_{bilayer} $\mu\text{F cm}^{-2}$	Q $\mu\text{F s}^{\alpha-1} \text{ cm}^{-2}$	α	C_{system} $\mu\text{F cm}^{-2}$
tHLM	218.1	2.24	2.17	729.08	3.24	7.56	0.81	0.70

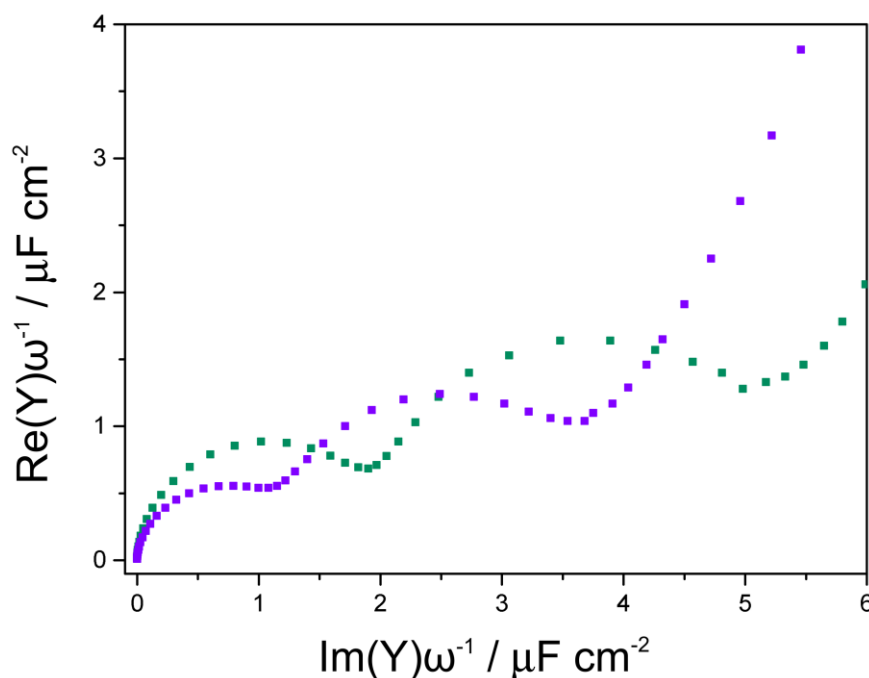


Figure 4.16. Impedance spectra represented in Cole-Cole plots for full WK3SH (turquoise) monolayer and tHLM system after addition of the lipid POPC lipid vesicles (purple).

4.2.1.2. SEIRA spectroscopy of POPC membrane systems

The structure of the POPC tBLM system was characterised by SEIRA difference spectroscopy. The resulting SEIRA spectrum of the mixed SAM formation is shown in figure 4.17, using the spectrum of 1-PrOH as reference. The negative bands correspond to the 1-PrOH removed from the surface, and the positive bands are ascribed to the adsorption of the SAM molecules on the Au surface. The bands at 2960, 2933 and 2875 cm^{-1} have contribution of the $\nu(\text{CH}_n)$ stretching vibrational modes of both molecules. The broad band at 3284 cm^{-1} corresponds to the $\nu(\text{OH})$ stretching from 6MH. The region below 1500 cm^{-1} contains the (CH_n) bending, scissoring and wagging modes, and the $\nu(\text{C-O})$ stretching. The SAM spectrum reveals the most important advantage of using the WK3SH tethered molecule; that is, contrary to other cholesterol tether molecules, such as CPEO3 [11], WK3SH lacks of bands in the amide region (1800 to 1500 cm^{-1}) [29]. Thus, the WK3SH:6MH SAM represents an ideal template for the study of biomolecules. A comprehensive description of the WK3SH:6MH SAM and tBLM can be found in Wiebalck et al. 2016 [29].

The completion of the assembly of the tBLM system was achieved after the addition and spontaneous spreading of the POPC vesicles onto the SAM. The SEIRA difference spectrum after removing the excess of lipids in solution is shown in Figure 4.18, using the SAM spectrum as reference. The spectrum of the lipids shows a negative broad band at ca. 1650 cm^{-1} , which represents the water removed from the surface of the SAM. This

band is assigned to the δ (OH) bending modes of water. The ν (CH_n) stretching modes corresponding to the aliphatic chains (hydrophobic tail) of the lipids are observed in the region between 3006 cm^{-1} and 2854 cm^{-1} . The band at 1737 cm^{-1} represents an overlap of at least two modes, the non-hydrogen bonded and hydrogen-bonded ester carbonyl stretching (ester groups in the head of the phospholipid) at 1743 cm^{-1} and 1733 cm^{-1} , respectively. The latter can offer information about the bilayer-water interface. In the lower region from 1500 cm^{-1} to 1200 cm^{-1} the bands are assigned to the (CH_n) bending, scissoring and wagging. Even though most lipids present similar IR spectrum, they can be distinguished by slight changes in the ν (CH_n) stretching region and the wagging and bending bands. These vibrations give information about the physical state of the fatty acyl chains. In this case, the position of the ν_{as} (CH_2) and ν_{s} (CH_2) stretching vibrations at 2926 cm^{-1} and 2854 cm^{-1} , respectively, indicates a liquid crystalline phase of the acyl chains, which for gel phase would appear at lower frequencies [19]. The phosphate group presents bands between 1240 cm^{-1} and 1000 cm^{-1} with a characteristic strong ν (PO_2^-) asymmetric stretching vibration at 1234 cm^{-1} . Table 4.4 summarizes the molecular vibrational modes corresponding to the POPC phospholipids. These results confirmed the proper formation of the POPC tBLM system on the surface of the Au electrode. The POPC lipids spectrum was highly reproducible in band shape and intensity. Since POPC lipids are present in most of the living membranes, this tBLM can be considered as a standard membrane-mimetic system providing a robust and stable construct.

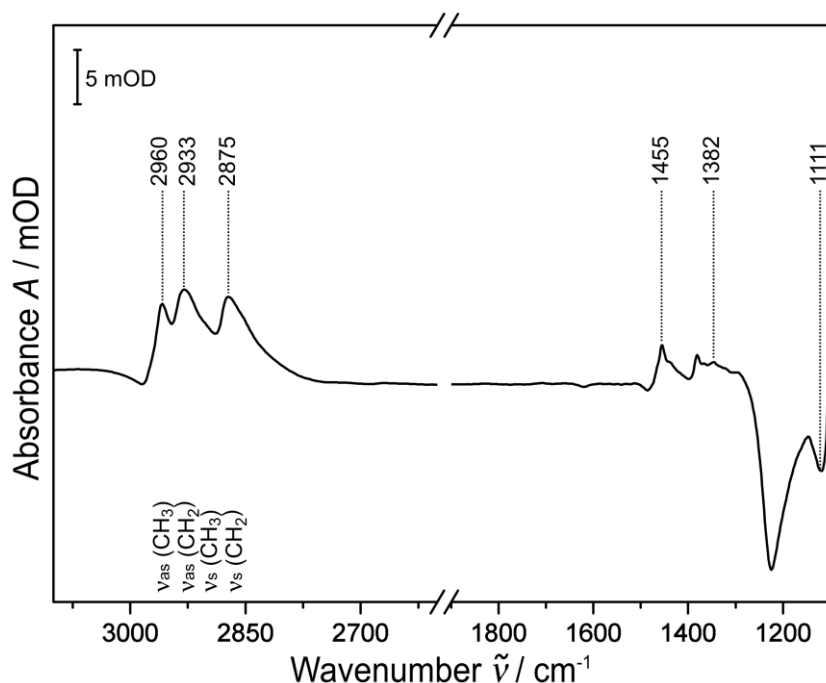


Figure 4.17. SEIRA difference spectrum of the mixed WK3SH-6MH SAM incubated in 1-propanol overnight at 4° C , the solvent spectrum was used as reference.

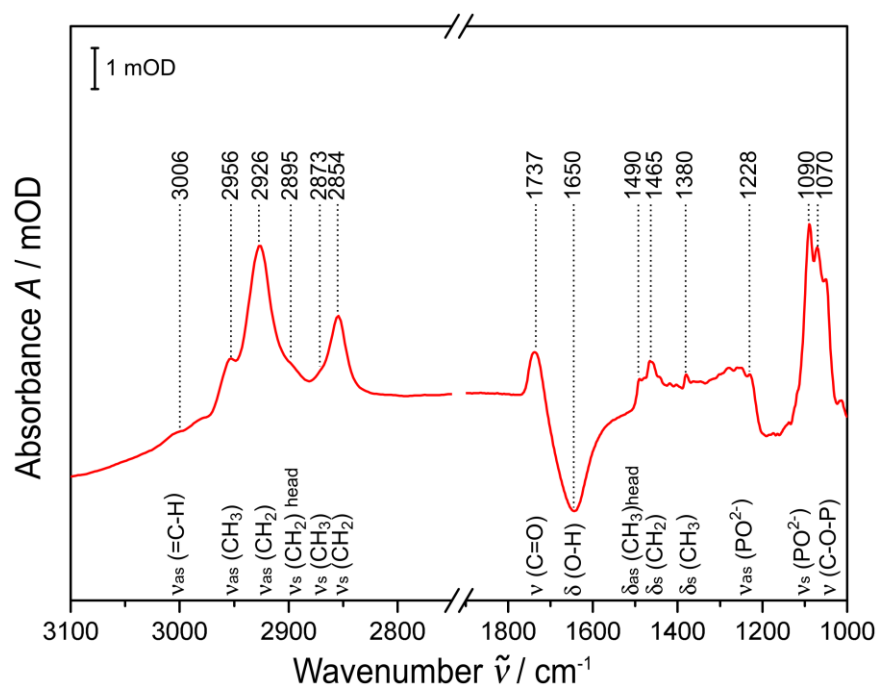


Figure 4.18. SEIRA difference spectrum of the POPC lipid after 2 hours incubation in 100mM NaCl 20mM BTP buffer at pH7.4, using WK3SH-6MH SAM as reference. Measured at 25° C.

Table 4.4. Band assignment for the POPC lipid vibrational modes.

Band position (cm ⁻¹)	Description
3006	CH asymmetric stretching
2956	CH ₃ asymmetric stretching
2926	CH ₂ asymmetric stretching
2895	Head-CH ₂ symmetric stretching
2873	CH ₃ symmetric stretching
2854	CH ₂ symmetric stretching
1743	C=O Ester carbonyl stretching
1737	1730 C=O---H Carboxylic acid-carbonyl stretching
1490	Head-CH ₃ asymmetric bending
1465	CH ₂ symmetric bending
1380	CH ₃ symmetric bending
1228	PO ₂ ⁻ asymmetric stretching
1090	PO ₂ ⁻ symmetric stretching
1070	C-O-P stretching

The SEIRA difference spectra of the POPC tHLM showed similar spectral features as for tBLM with only slight changes in relative intensities (data not shown). Since the lipids are the same as in the tBLM, the assignment of the IR modes shown in table 4.4 is also applicable for the tHLM system.

4.2.1.3. Membrane incorporation of enniatin B

This study presents for the first time a direct spectroscopic observation of EB peptide incorporation into membrane models monitored by SEIRA spectroscopy, since previous IR studies of EB were collected only in organic solvents. To achieve the results shown in figure 4.20 the independent incubation of EB in presence of Na^+ , K^+ and Cs^+ ions was investigated by SEIRA spectroscopy. In all three cases the characteristic spectrum of EB was observed [61] and thus, it suggests a successful incorporation into the POPC membrane system. To assign the characteristic bands of EB peptide, the incubation spectrum with Na^+ ion (grey) shown in figure 4.19 was chosen as an example. The bands at 1747 cm^{-1} and 1660 cm^{-1} correspond to the ester $\nu(\text{CO})$ stretching mode of the D-hydroxyisovaleric acid and to the amide I of the *N*-methyl-L-valine units, respectively. It should be noted that the present amide I normal modes differ from the conventional amide I composition in proteins or peptides due the absence of the H-atom at nitrogen. Therefore, the amide I normal modes of EB are composed of mainly the $\nu(\text{CO})$ stretching and a minor contribution of the amide (CN) bond vibration. The intensity of the peptide bands changed when removing the excess of peptide in

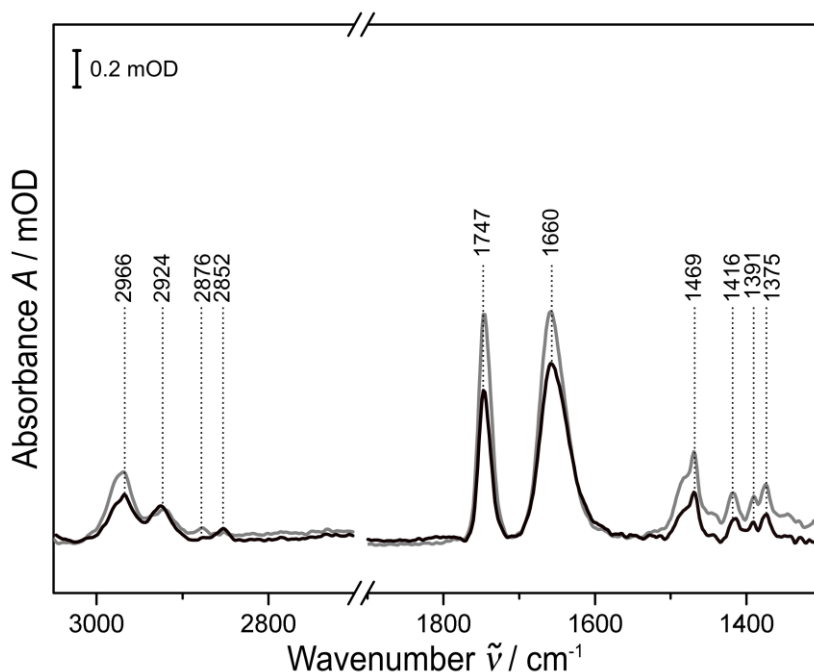


Figure 4.19. SEIRA difference spectra of EB: Na^+ complex incubation in 100mM NaCl 20mM BTP buffer at pH 7.4 (grey) and after washing the peptide excess with buffer (black). Both spectra were measured at 25°C and used the tBLM as reference spectrum.

solution after the incubation (black spectrum). The CO band decreased from 1.23 to 0.81 mOD, and the amide I from 1.24 to 0.95 mOD indicating that EB weakly bound to the membrane surface was removed. The bands in the 2966 cm^{-1} to 2852 cm^{-1} region correspond to $\nu(\text{CH}_n)$ stretching modes mostly from the peptide, as apparent from the shifted position and altered relative intensities in comparison to lipids. While for lipids the $\nu_{\text{as}}(\text{CH}_2)$ at 2926 cm^{-1} presents the most prominent peak due to the large number of CH_2 groups in the acyl chains, the IR spectrum EB is dominated by the $\nu_{\text{as}}(\text{CH}_3)$ at 2966 cm^{-1} due to the isopropyl residues. The broadening of these bands indicates that EB is not located purely within the membrane core, but potentially distributed also to a considerable amount at the membrane head group region. In the lower frequency region there are the (CH) bending and rocking modes are detected at 1469 cm^{-1} , 1416 cm^{-1} , 1391 cm^{-1} and 1375 cm^{-1} . Since these vibrational modes have shown to be unchanged for EB in presence of the different ions, the analysis of the ion-incubation spectra is focused on the region from 1800 to 1500 cm^{-1} . The resulting spectra are shown in figure 4.20A. In this way, the incubation of EB with Na^+ (black spectrum) described above can be compared to spectra in Cs^+ and K^+ buffers. The incubation with Cs^+ ions (blue spectrum) depicts bands in the same position as in the Na^+ spectra, i.e. at 1747 cm^{-1} and 1660 cm^{-1} , but with slightly higher intensities. In the case of the K^+ incubation, in addition to an increase in the intensity an up-shift of 2 cm^{-1} for the CO band and 6 cm^{-1} was observed for the amide I, resulting in band positions at 1749 and 1666 cm^{-1} (see Table 4.5). Interestingly, in the case of Cs^+ and K^+ , the changes after removing the excess of peptide are less pronounced than in the case of Na^+ . The fact that EB was incubated in presence of each type of cation independently from the others allows the assumption that each spectrum corresponds to the respective complexed species, denoted as EB:ion. Furthermore, since EB represents a dynamic system interacting with the membrane core, head group region or bulk solution, an equilibrium between free EB and differently composed EB:ion complexes has to be considered when assigning the spectral features to certain EB:ion complexes. Different conditions can influence this equilibrium, like the affinity to the ion and the concentrations as discuss below. Nonetheless, one can conclude that these results demonstrate the incorporation and interaction of EB:ion complexes with the POPC tBLM membrane system.

Water interference in the SEIRA spectra of enniatin B incubation

The peptide shows broad amide I bands for all three ions, which suggests contribution of the bending mode from water (ca. 1650 cm^{-1}). Even though SEIRA is rather insensitive to contributions from the bulk due to the steep decay of the surface enhancement, such minor contributions may affect this spectral region. To analyse the impact of the water absorption band, the water contribution was removed by subtracting a water reference spectrum from the entire batch of spectra of incubation experiments (> 50 spectra for each experiment) using a similar approach to Palacky et al. (2011) [110] to

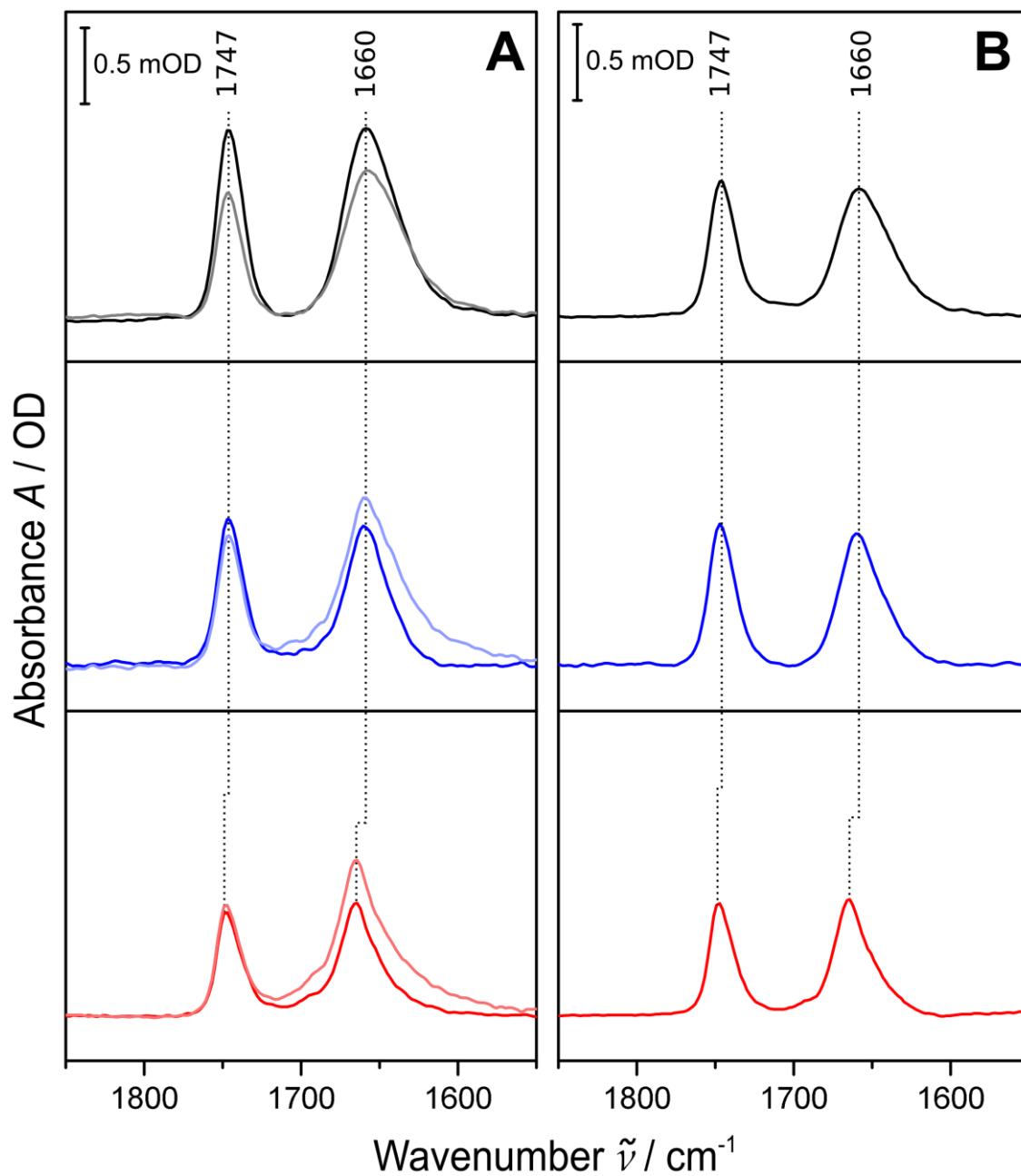


Figure 4.20. **A:** SEIRA difference spectra of EB incubation in POPC tBLM in presence of Na^+ (black and grey), Cs^+ (blue and light blue) and K^+ (red and light red). This independent incubation was carried out in 100mM ion-Cl 20mM BTP buffer at pH 7.4 (dark lines) and after washing the peptide excess with new buffer solution (light lines). All spectra were measured at 25° C and using the tBLM as reference spectrum. **B:** Calculated water-free spectra of the respective ion incubation of EB following the same colour code.

avoid artefacts due to manual subtraction of single spectra (this spectral correction was performed in collaboration with Dr. Jacek Kozuch). Accordingly, the water spectrum was subtracted from the principal components (determined by singular value decomposition; only those components that showed spectral features above the noise level were considered as principal components) of the SEIRA spectra by matching the 3400 cm^{-1} absorption of water and thus removing efficiently the water contribution at 1650 cm^{-1} .

The results from the water subtraction are shown in figure 4.20B. Table 4.5 shows the positions and intensities, as well as the band intensity ratio for the three incubation experiments as raw data and after water removal. The position of the CO and amide I bands are maintained in the water-free spectra of all three ions, so that the spectral positions in the raw spectra can be used as well for the assignment to the EB:ion complexes. Accordingly, the peak positions shown in table 4.5 can be tentatively assigned to the EB:ion complexes formed in membranes with yet unknown stoichiometry. As mentioned above, these positions may not reflect one species in each case but possibly mixtures between free EB and different EB:ion complexes in different locations in the membrane, which will be addressed later in this thesis. In contrast to Ovchinnikov et al. (CO and amide absorptions at 1746-1744 cm^{-1} and 1666-1665 cm^{-1} for every EB:ion complex), the present study shows a distinct difference of the EB: K^+ complex with respect to Na^+ and Cs^+ . This suggests that in organic solvents different species are formed than in membranes or that, based on the coincidence of the spectral positions, a K^+ impurity in the previous experiments led to a main contribution of EB: K^+ in all cases. However, in the present work, the similarity of the spectra in Na^+ and Cs^+ buffers is against the expectation of a Hofmeister-series-like trend ($\text{Na}^+ > \text{K}^+ > \text{Cs}^+$, or vice versa) and allows the assumption that a similar ion-free species is formed in both cases under steady-state conditions. This would be in line with an increased selectivity of EB for an ion complex formation with K^+ .

Table 4.5. SEIRA data collected from the incubation of EB with the tBLM system at different ion-buffer.

	Raw spectra			-H ₂ O spectra		
	CO (cm^{-1})	Amide I (cm^{-1})	CO/amide I	CO (cm^{-1})	Amide I (cm^{-1})	CO/amide I
EBNa⁺	1747	1660		1747	1660	
	0.81	0.95	0.85	0.89	0.84	1.06
EBCs⁺	1747	1660		1747	1660	
	0.85	1.10	0.77	0.93	0.87	1.06
EBK⁺	1749	1666		1749	1666	
	0.72	1.02	0.71	0.73	0.76	0.96

The band ratios of all three complexes changed significantly after the water removal, which reflects the influence of water in the spectra (see table 4.5). It is important to mention at this point that in SEIRA the intensity and ratio of the bands can give information about the distance and the orientation of the vibrational modes in respect to the surface [14] [86]. Since the membrane is anchored to the surface and shows only minor fluctuations at constant electrode potentials, the absolute intensity of the IR bands of EB are directly dependent on its concentration in the membrane. Thus, determining the distance or location of the EB complexes in respect to the surface of the Au film requires the exact knowledge of the number of EB molecules. Therefore, the absolute intensities in the SEIRA spectra will be used as an indicator of the affinity of EB to bind to membranes in the presence of the chosen ions. On the other hand, the orientation can be estimated (or compared) due to the selection rule that implies a major enhancement for the vibrational modes perpendicular to the Au surface. As mentioned above, an ester CO and N-methylated amide groups in its backbone characterise the particular composition of EB. This means that instead of the amide I and II (total dipole moment perpendicular to each other) as for normal amino acid composition, EB spectra shows a CO and amide I band. Moreover, in EB backbone all CO bonds of the esters groups and of the amides point in opposite directions. Due to this and the C₃ symmetry-like structure of EB and its complexes the main component of the effective transition dipole moment of the CO and amide vibrations is oriented along the axis of the EB ring. Therefore, the ratio of both intensities will not provide direct information about the orientation of EB within the membrane in respect to the surface as use for proteins. However, it may represent a specific value for each EB species due to characteristic angles of the CO bonds in respect to the ring axes.

4.2.2. Structural study of ennitain B ion complexes in membrane systems

4.2.2.1. Enniatin B ion-exchange in membrane systems

Continuing with the hypothesis that EB can form complexes with monovalent cations while inducing ion-transport through the membrane, the effect of the three alkali metal ions Na⁺, Cs⁺ and K⁺ was investigated by SEIRA spectroscopy in a sequential manner using the tBLM system. The decision of using K⁺ as the last one is based on the observation that EB might have a higher affinity to this ion like the well-characterised depsipeptide Beauvericin [61]. The resulting spectra of the sequential ion exchange of EB are shown in Figure 4.21A. The EB spectrum in presence of Na⁺ ion was the starting point showing the same band positions as shown for the incubation, CO at 1747 cm⁻¹ and amide I at 1660 cm⁻¹. After exchanging the buffer to Cs⁺ there was no shift of the bands, but the intensity of the CO and amide I bands increased from 0.81 to 1.00 mOD and from 0.95 to 1.33 mOD, respectively. In the case of the EB:K⁺ complex, the spectrum showed major changes reflected by the shifts of both bands, and a

significant increase in intensity. The amide I band with 1.40 mOD appeared at 1666 cm^{-1} , and the CO band shifted by 2 cm^{-1} to 1749 cm^{-1} (1.14 mOD). The shifts of the bands are the same as observed in the independent incubation (*vide supra*), and it can be considered as an important marker to identify the formation of a complex of different stoichiometry. These experiments support the interpretation that EB presents a similar major conformational state of the backbone with Na^+ and Cs^+ , i.e. a major fraction of ion-free EB or/and C=O ligands oriented in similar directions, which in both cases differs from the conformation adopted in presence of K^+ ion. Again, the findings in previous studies in literature differ from the results presented here. The conditions in the tBLM system offer a different environment for the peptide than in other studies. The interaction of the EB with the lipid membrane and with the solution-interface may have a great impact in the stoichiometry and conformation adopted by the ring peptide.

Ion-exchange in monolayer membrane systems

The same experiment described above was performed using a POPC lipid monolayer, defined as tHLM system. The main goal of this analysis is to evaluate the necessity of a lipid bilayer for EB for comparison with the tBLM system. The resulting ion-exchange spectra are shown in figure 4.21B, following the same colour-code for each ion as in the tBLM spectra. It was possible to reproduce the spectral positions and the amide I band-shift when exchanging to the ion solution with K^+ . Interestingly, there is no shift of the CO band, which appears at 1747 cm^{-1} for all three ions. In general, the three spectra in tHLM are of higher intensity than in the tBLM experiment. Moreover, the right shoulder in the amide I band for Na^+ and Cs^+ ions indicates a probable contribution of different species in the spectra. Overall, these findings show that for EB the formation of the ion-complex and/or membrane-interaction are independent from the membrane thickness, ergo EB can be incorporated into mono and bilayer lipid system.

It is important to consider that in the tHLM system there is no aqueous reservoir between the SAM and lipid monolayer. Therefore, the complex may have reduced vertical movement within the membrane, located mostly in the top leaflet of the tHLM (surface-buffer interface) instead.

Ion-complex reversibility

To evaluate the ion-selectivity and reversibility of EB complex formation, the solution was exchanged back to Na^+ after the K^+ complex. The results are presented in figure 4.22. The lower intensity and back shift of the CO and amide I bands when changing from K^+ to Na^+ reflects a low selectivity of EB between this two ions. Additionally, the affinity of the peptide can be analysed directly due to the exchange of one solution to another one without altering the rest of parameters of the system. From the quality of the spectra and the reproducible behaviour of EB with the different ions, it is possible to

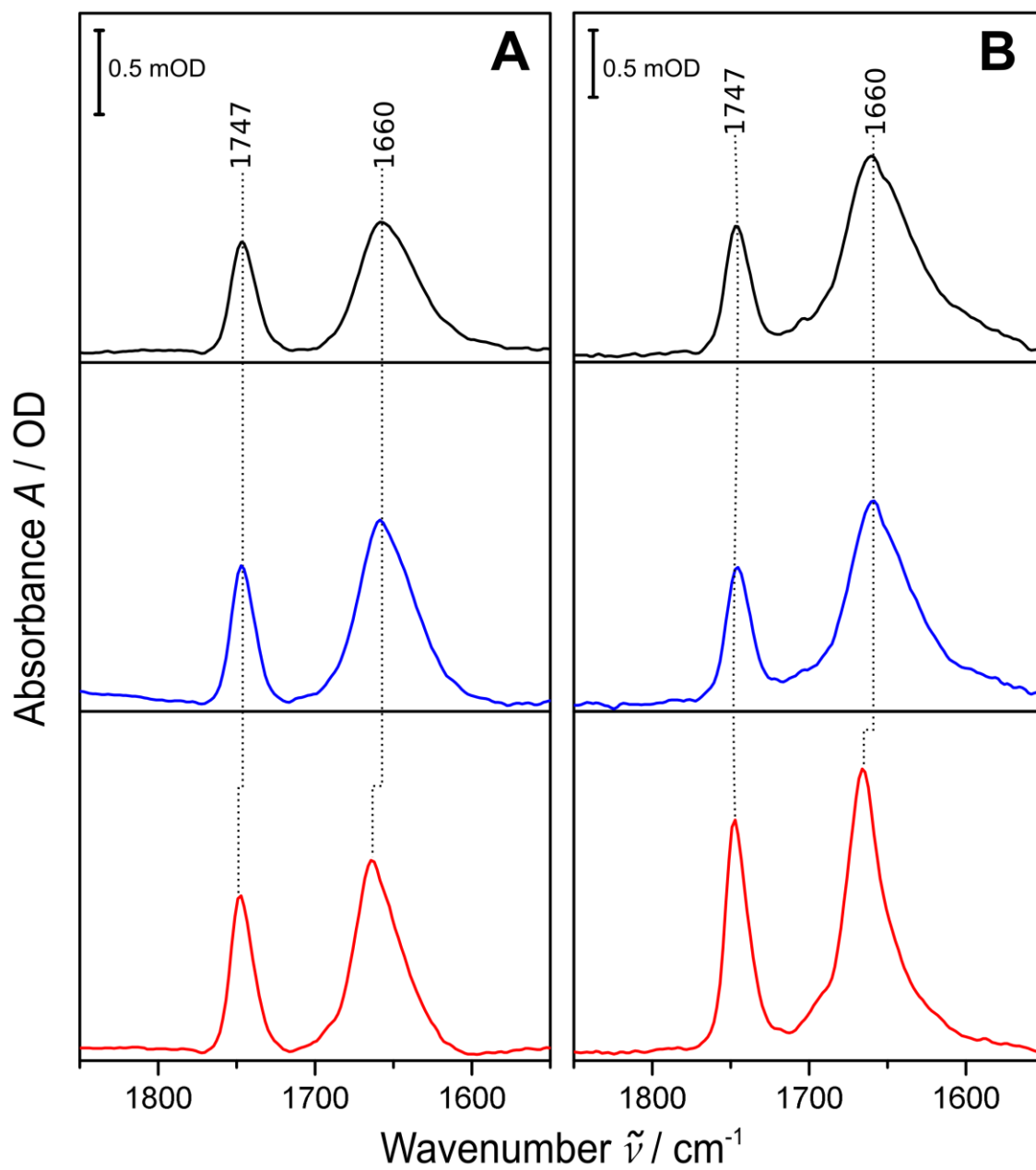


Figure 4.21. SEIRA difference spectra of the ion-exchange performed with the tBLM (A) and tHLM (B) systems. All spectra were measured at 25° C and used the tBLM or tHLM as reference spectrum. For both systems: EB:Na⁺ complex is black, EB:Cs⁺ complex is blue and EB:K⁺ complex is red.

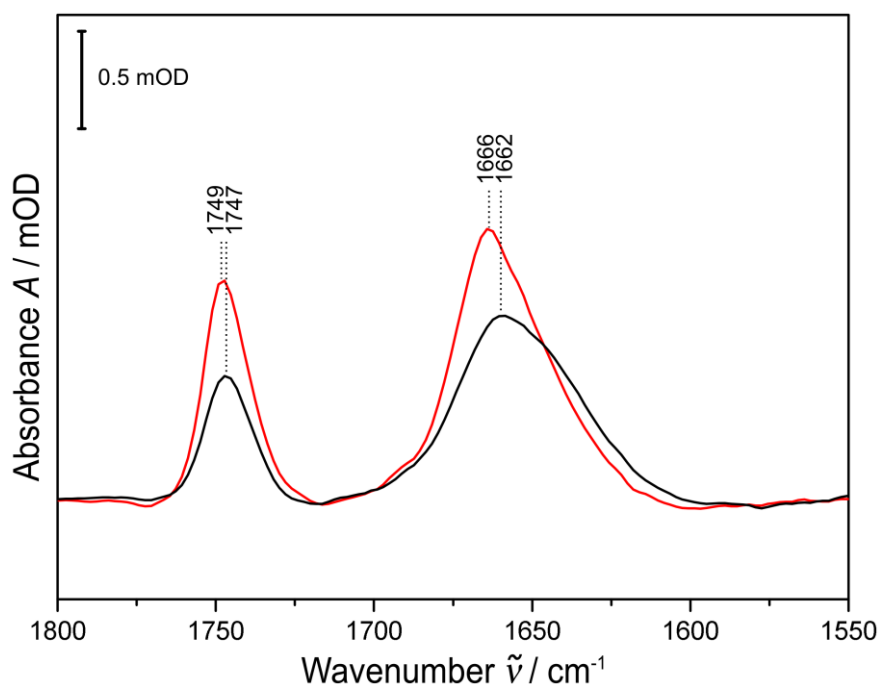


Figure 4.22. SEIRA difference spectra for the ion-exchange reversibility of EB:Na⁺ (black) complex after EB:K⁺ (red). All spectra measured at 25° C.

assume a higher affinity of EB to K⁺ than to the other two ions. Experiments performed at a 10 times lower EB concentration supports this statement, since the absolute intensity of K⁺ spectrum increased notably compared to other ions. The fact that the amide I band in the Na⁺ spectrum appears at 1662 cm⁻¹ instead of 1660 cm⁻¹ (Na⁺ incubation position) reveals the presence of residual EB:K⁺ species, which is another evidence for the higher affinity of EB to K⁺ ion. The very same effects were observed in the experiment performed using the tHLM system (data not shown). Nonetheless, the partial reversibility of the spectral changes of EB in presence of K⁺ and Na⁺ may indicate a preference for K⁺ over Na⁺, but with a much lower selectivity as explained by Pressman (1976) and Kamyar et al (2004). Both studies reported that the affinity of EB towards K⁺ ion is significantly lower than in the case of Valinomycin and therefore, EB shows reduced K⁺/Na⁺ discrimination.

4.2.2.2. IR spectroscopy of enniatin B

IR spectroscopy was performed for the solid and solution state of the EB to structurally analyse the peptide outside the tBLM system. The result of the EB solid-state diamond-ATR-IR spectrum of the lyophilized peptide is shown in figure 4.23. The EB solid-state spectrum shows similar spectral contributions as the EB SEIRA spectrum in figure 4.19, with comparable band shape and positions for the ν (CH_n) stretching modes at 2961, 2930 and 2873 cm⁻¹, as well as the bands in the lower region. The backbone bands appear at 1735 cm⁻¹ (CO) and at 1663 cm⁻¹ (amide I). The solid-state sample lacks the molecular interactions between the peptide and the ions, and of both with

the solution. Therefore, this result allows identifying the characteristic vibrational modes of the EB peptide. The similarity of the spectra from the two techniques also confirms the presence of EB in the tBLM system analysed by SEIRA.

The FT-IR transmission spectra of the EB in ion-free solution and of the respective complexes with Na^+ , K^+ and Cs^+ ions are shown in figure 4.24. The aim of this analysis was to evaluate the peptide behaviour aqueous conditions in absence of the membrane. The second derivative of the spectra was used for the determination of the peak positions of the bands, and in all three cases the CO band appears at ca. 1746 cm^{-1} (except in presence of Cs^+ , see below), which is in line with literature and supports the complexation of ions using the amide O-atoms. The most significant change was observed between the ion-free EB and the K^+ complex with an up-shift of the amide I band from 1656 cm^{-1} to 1665 cm^{-1} , while the CO remains at a similar position. The positions for the spectrum in presence of K^+ ions are in line with the SEIRA spectra and thus confirm the assignment of these spectral positions to the EB: K^+ complex. The very broad bands together with the similar spectral positions in absence of ions and with Na^+ suggest that in both cases the same species is present. Thus, this indicates that in Na^+ presence most of EB remains in its uncomplexed form. These results support the interpretation of higher affinity of the peptide for the K^+ ion as described above. For K^+ ion, the peak positions reveal similarities to the spectra detected in tBLM, and suggest that both in solution and tBLMs EB forms a EB: K^+ complex as a major component. In the case of Na^+ ion, the main fraction contributing to the spectra appears to be the ion-free EB. The difference in the absolute positions of peaks in tBLMs and in solution can be explained based on the polarity of the different media.

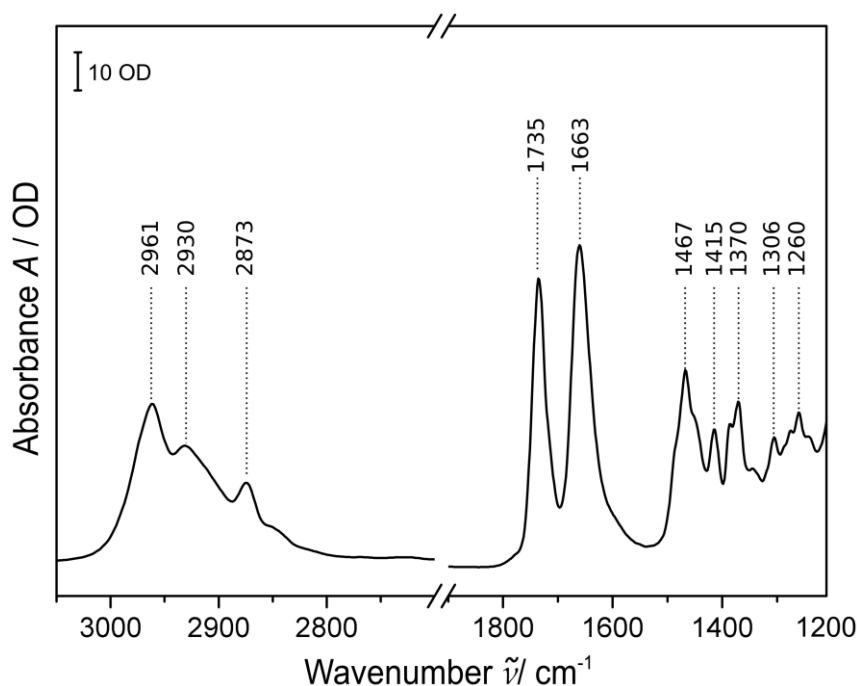


Figure 4.23. ATR-diamond IR spectrum of the dried EB peptide measured at 25°C .

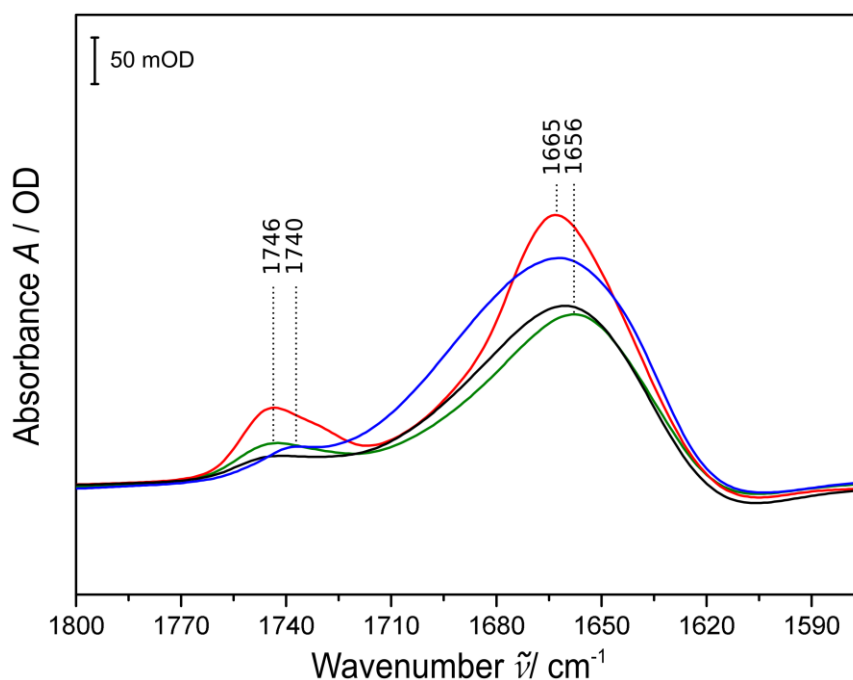


Figure 4.24. FT-IR transmission difference spectra of the EB peptide alone (green), in presence of Na^+ (black), in presence of Cs^+ (blue), and in presence of K^+ (red). All spectra were measured at 25° C, in an ion-buffer and ethanol mixed solution, and using the solution spectra as background.

In the present study, the intention was to measure the peptide in conditions as close as possible to the SEIRA experiments. For this reason, the IR transmission spectra of the EB in solution were recorded using a mixture of the corresponding buffer with a low percentage of EtOH. Most of the studies described in literature, use organic solvents like acetonitrile (ACN) due to the hydrophobicity of the peptide. The work used as reference for enniatins characterization is the work offered by Ovchinnikov et al. in 1974 [61], which presents a detailed analysis of this peptides with focus on EB and its complexes. Table 4.6 shows the comparison of the two studies. The authors analysed the crystalline samples of EB peptide and the dissolved complexes with different ions in ACN by IR spectroscopy. With attention on the backbone-bands region of the solid state, the CO is shown at 1744 cm^{-1} and the amide I at 1670 cm^{-1} with a shoulder at ca. 1657 cm^{-1} . Unfortunately, these authors used a different method for the investigation of the solid peptide (KBr pellets of crystalline EB), which complicates a direct comparison of the spectra. On the other hand, the band positions of the complexes in ACN show more similarities to the spectra measured in IR transmission and SEIRA. The Na^+ complex shows a broad amide I band, and there is an up-shift of this band for the K^+ complex, even though is only 1 cm^{-1} in ACN compared to the 8 cm^{-1} in buffer-EtOH. As mentioned before, this supports the previous interpretation that EB did not form distinct complexes with the chosen ions in ACN. The changes for the ester CO mode were minimal as well as in our study.

Table 4.6. IR spectroscopy data comparison of the backbone vibrational modes of EB in this project vs Ovchinnikov 1974.

	SEIRA (Buffer)		IR transmission (Buffer-EtOH)		Ovchinnikov 1974 (ACN)	
	ν CO cm ⁻¹	ν amide I cm ⁻¹	ν CO cm ⁻¹	ν amide I cm ⁻¹	ν CO cm ⁻¹	ν amide I cm ⁻¹
EB	-	-	1746	1656	1744	1666
EB:Na ⁺	1747	1660	1747	1656	1746	1665
EB:K ⁺	1748	1666	1746	1665	1744	1666
EB:Cs ⁺	1747	1660	1740	1659	1645	1666

4.2.2.3. Theoretical calculations of enniatin B ion complexes

Using DFT calculation⁵ it was attempted to provide a direct assignment of the SEIRA spectra to certain EB:ion species with a specific stoichiometry. Initially, only the dihedral angles of the ring backbone were fixed to 180° during geometry optimization. After this initial optimization, the geometry was optimized without constraints. The starting point was the crystal structure described in [77], which provides the positions of the atoms of the EB peptide. These conditions were first applied to EB:Na⁺ 1:1, EB:Na⁺ 2:1, EB:K⁺ 1:1, and EB:K⁺ 2:1. Figure 4.25 shows the most favourable structures obtained from the DFT analysis of EB and its ion complexes. In the case of the EB:Na⁺ complex, the 1:1 stoichiometry was most favourable, since in the 2:1 complex one of the rings dissociates after several optimization cycles and the calculation does not converge. This is in contrary to literature where a ratio 2:1 was suggested for Na⁺ ion [76]. For the EB:K⁺ complex, a 2:1 coordination resulted the most suitable structure, which is in line with the proposed ratio in previous studies [61] [76]. In the 1:1 arrangement, the K⁺ ion gets displaced to yield a structure in which solely the amide CO groups coordinate the ion in an “open-faced-sandwich-like” manner. This structure would not screen the charge of K⁺ ion and thus, is not appropriate for accommodation of the ion in the membrane. A similar process is observed for the 1:1 EB:Cs⁺ complex, which can be excluded as a possible ratio in membrane. However, in literature it was suggested that Cs⁺ forms either 2:1 or 3:2 complexes. In the 3:2 stoichiometry, Cs⁺ can theoretically be complexed via different combinations of amides and esters of two EB molecules as shows the representation in figure 4.26.

⁵ Dr. Jacek Kozuch provided the DFT calculation for the enniatin B:ion complexes structures, and the respective calculated spectra.

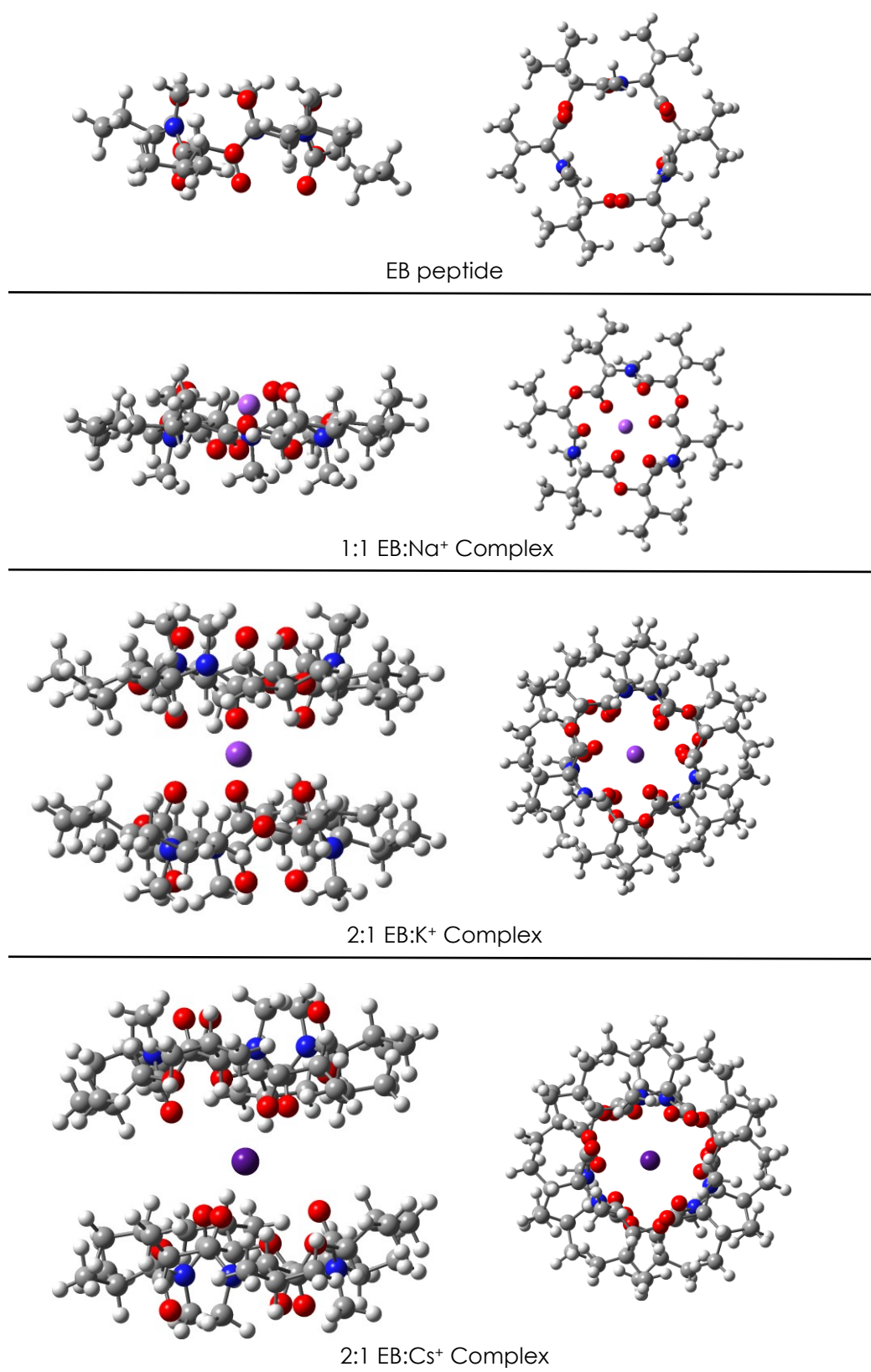


Figure 4.25. 3D representation of the most stable structures resulted from the DFT calculations of EB (top) and the respective ion complexes with Na⁺ (second top), K⁺ (second from bottom) and Cs⁺ (bottom). The figures on the left are the side images, and the right figures are the top images of the corresponding structures. Atoms are depicted as spheres and the covalent bounds as grey lines. The central ion is shown in purple colour, oxygen atoms in red, nitrogen atoms in blue, carbon atoms in grey, and hydrogen atoms in white.

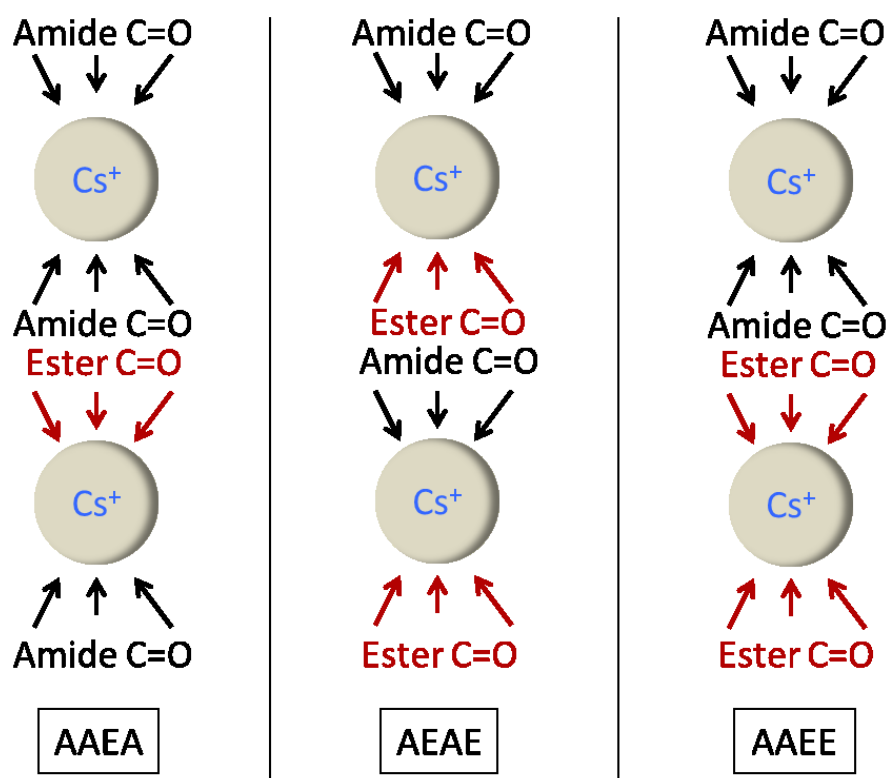


Figure 4.26. Schematic representation of the amide/ester ligand combination for the 3:2 conformation of the EB:Cs⁺ complex. The arrows indicate CO ligand-ion coordination. The amide ligands are depicted in black, while the ester ligands are in red. The cream-colour spheres represented the Cs⁺ ion. The codes indicating the ligand combinations are shown below each representation.

Among these possibilities, the 3:2-AAEA-complex was the most probable 3:2-structure in a hydrophobic environment (n-pentadecane = membrane core), with a difference to the other two combinations by 72.7 kJ/mol or 88.2 kJ/mol (see table 4.7). Taking into account a theoretical reaction 4.1, a energy difference of $\Delta G = -11.4$ kJ/mol is obtained demonstrating that the 2:1 complex is predicted to be the preferable complex with Cs⁺ within the hydrophobic core of a membrane. These findings for Cs⁺ ion complex disagree to the 1:1 stoichiometry ("open-faced-sandwich-like" complex as the 1:1 with K⁺ explained above) suggested in the DFT study of EB:Cs⁺ by Makrlík et al. (2014).

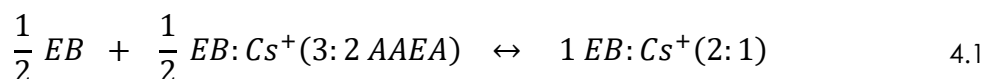


Table 4.7. Sum of electronic and thermal Free Energies for the calculated complexes of EB with Cs⁺ ion and EB alone. The unit "H" stand for Hartree/Particle, where 1H = 2.6254995 MJ/mol.

Calculated structure	Free Energies
EB32Cs_AAEA	- 6436.792218 H
EB32Cs_AEAE	- 6436.764545 H
EB32Cs_AAEE	- 6436.758624 H
EB21Cs	- 4284.600798 H
EB	- 2132.400694 H

The calculated spectra of the most favourable species, i.e. EB, EB:Na⁺-1:1, EB:K⁺-2:1, and EB:Cs⁺-2:1, are compared in figure 4.27 to the IR spectrum of dried EB and the SEIRA spectra of EB in the tBLM system in presence of the different ions. The spectra of the complexes resulted from the constraints-free calculations of the structures in n-pentadecane as hydrophobic solvent to mimic the membrane core environment using a polarisable continuum model. For the dried EB structure, DFT spectra were calculated in n-pentadecane and in water environment as well. To analyse the band composition of the experimental spectra, a fitting of both peptide bands in the SEIRA spectra was carried out after removing the water contribution. The red and blue spectra correspond to the Lorentzian and Gaussian functions, respectively. All four spectra evaluated here show two components. The band positions for each spectrum are indicated in table 4.8, along with the DFT calculated frequencies. In principle, one can assume that the pair of Lorentzian bands refers to a very homogeneous environment (hydrophobic membrane core), while the Gaussian-shaped bands describe a heterogeneous environment involving different interactions, i.e. the head group region where H-bonds, ionic interactions and other specific interactions are possible. Excluding EB:Na⁺ 1:1 complex, the relative intensities of the Lorentzians (SEIRA spectra) resemble very well the CO/amide I ratio obtained from the DFT calculations. In the case of the IR spectrum of dried EB, it appears to contain a mixture of dried (Lorentzian, red) and hydrated (Gaussian, blue) peptide. The Lorentzian components of dried EB at 1713 and 1664 cm⁻¹ look much alike to the DFT spectrum in the hydrophilic water environment of the polarisable continuum model, which suggest an polar environment due to the presence of water molecules or a crystalline fraction, in which dipole moments are oriented in parallel. The similarities between Na⁺ and Cs⁺ ions are reflected in the Lorentzian component of the amide I of the respective SEIRA spectra, appearing in both cases at 1662 cm⁻¹. In the DFT spectra a different trend is observed for the EB:ion complexes with an increasing frequency from Na⁺ over K⁺ to Cs⁺. This contradicts with the trend of the Lorentzian fit and of the overall band positions in the SEIRA spectra, where positions for Na⁺ and Cs⁺ are similar and the EB:K⁺ complex is blue-shifted.

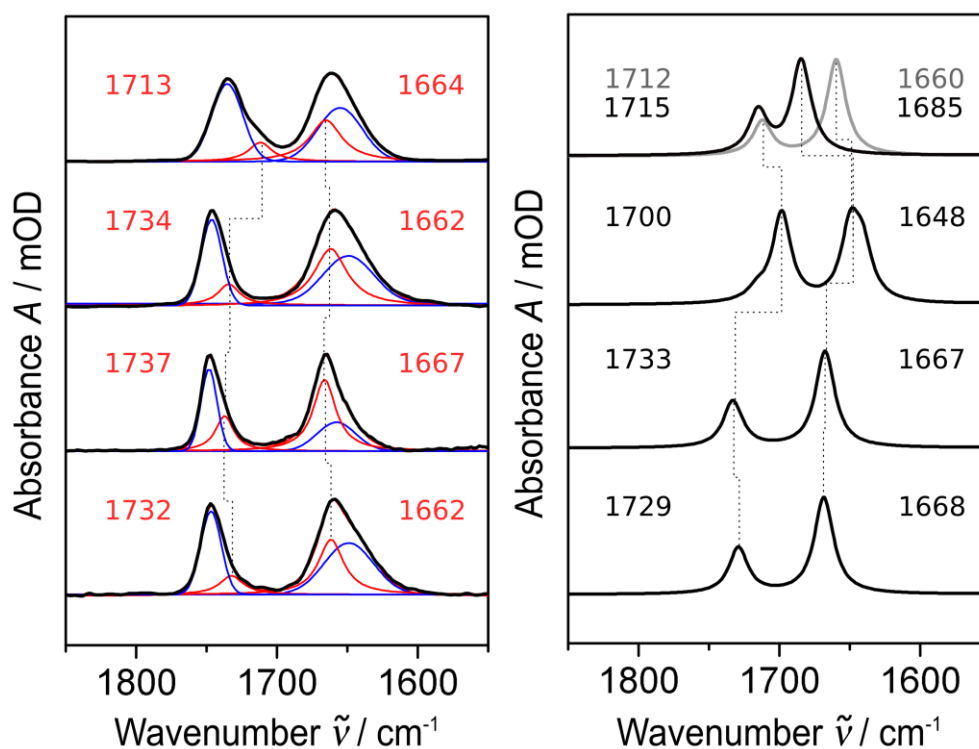


Figure 4.27. Band fitting (left spectra) using Lorentzian (red) and Gaussian (blue) functions of the FT-IR spectrum of dried EB (top) and the SEIRA incubation spectra of EB with Na^+ , K^+ and Cs^+ (bottom). The positions corresponding to the CO and amide I bands are shown in red colour. The DFT calculated spectra (right side) of the most stable structures for EB (top) and EB complexes with Na^+ , K^+ and Cs^+ (bottom) in a hydrophobic environment (membrane-core) are shown in black. The positions corresponding to the CO and amide I bands are shown in black colour as well. The grey spectra and positions shown for dried EB correspond to the peptide in a polar environment.

Table 4.8. Peptide band (CO and amide I) comparison between experimental, component analysis and DFT spectra. The G and L letters corresponds to Gaussian and Lorentzian functions, respectively. The nP refers to the conditions within the membrane and H_2O to solution-membrane interface.

	CO band (cm^{-1})		Amide I band (cm^{-1})		
EB dry	1735		1663		ATR—IR
	1735 _G	1712 _L	1666 _L	1656 _G	Fitting
	1715 _{nP}	1712 _{H₂O}	1684 _{nP}	1660 _{H₂O}	DFT
EB:Na^+	1747		1660		SEIRA
	1746 _G	1733 _L	1662 _L	1648 _G	Fitting
	1698 _{nP}	1694 _{H₂O}	1648 _{nP}	1633 _{H₂O}	DFT
EB:K^+	1749		1666		SEIRA
	1748 _G	1737 _L	1666 _L	1656 _G	Fitting
	1733 _{nP}	1722 _{H₂O}	1668 _{nP}	1650 _{H₂O}	DFT
EB:Cs^+	1747		1660		SEIRA
	1747 _G	1732 _L	1662 _L	1648 _G	Fitting
	1729 _{nP}	1717 _H	1669 _{nP}	1653 _H	DFT

The most important outcome from this multifaceted analysis is the assignment of the 2:1 stoichiometry to the EB:K⁺ complex, which is supported by SEIRA and DFT results. For Na⁺ and Cs⁺ SEIRA and DFT spectra showed less conclusive assignments. The most favourable structures for Na⁺ and Cs⁺ ion complexes of EB in a membrane core-mimic environment were 1:1 and 2:1, respectively. The assignments presented here for these ions contradict the suggestions in previous literature.

4.2.3. Mechanism of membrane incorporation and ion binding

To follow the membrane binding kinetics of the peptide and analyse the mechanism of incorporation, EB was incubated during 70 minutes with the tBLM system for each ion and monitored by SEIRA. The intensities of the CO and amide I bands are represented as a function of time in Figure 4.28 (top). The sigmoidal curve indicates an “auto-catalytic” insertion of EB into the lipid bilayer. A suggested two-step binding process, neglecting the back reactions⁶, is shown in figure 4.29. In the first step, multimeric species of EB interact with the membrane (P_{PreAd}) and convert into monomers on the surface (P_{Ad}). This step consists of two reactions expressed in reaction 4.2, the association to the membrane, and reaction 4.3, the dissociation of the multimer species into monomers. The second step of this membrane-binding process is represented by reactions 4.4, a slow incorporation of one complex into the core of the membrane, and 4.5, the auto-catalytic reaction where more EB complexes are inserted into the membrane (P_{Mem}).

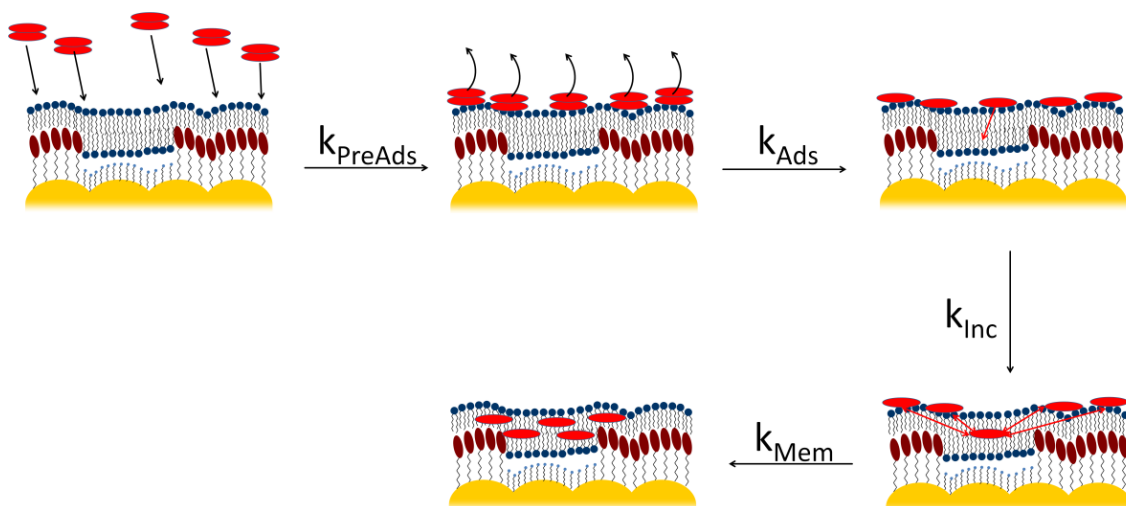
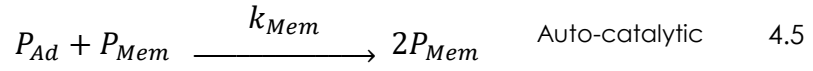
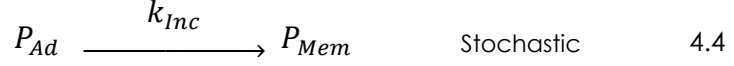
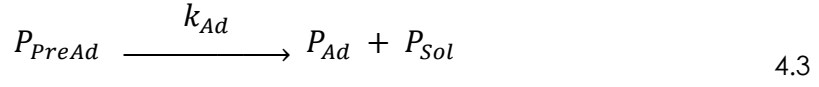


Figure 4.29. Schematic representation of the reaction for the Peptide-membrane binding kinetics process. The reaction constant for each step is indicated on the arrows as the K of the respective species, being so: PreAds the pre-adsorbed multimers; Ads the species adsorbed on the membrane surface; Inc the random incorporation of species; and Mem the species incorporated in the membrane as a result of the auto-catalytic process.

⁶ The kinetic equations to fit the binding kinetics spectra of the systems were developed in collaboration with Dr. Jacek Kozuch.



The adsorption of the aggregated species, given by n_{PreAd} , (reaction 4.2) can be described by Langmuir-type adsorption. In this way, this reaction is a second-order reaction considering the peptide in solution (P_{Sol}) and the free binding places in the membrane surface (see eq. 4.6). Once bound to the surface the peptide aggregates begin to dissociate into monomers. The first term in 4.6 refers to the decrease of the concentration of the peptide in solution due to the adsorption, and the second term represents the increase of the concentration due to the dissociation into peptide monomers. The contrary effect is represented in equation 4.7, since (P_{PreAd}) corresponds to the multimeric species, which concentration decreases (second term eq. 4.7) with its decomposition into monomers.

$$\begin{aligned} \frac{dP_{Sol}}{dt} = & -k_{PreAd} \cdot P_{Sol} \cdot \left(P_{Ad,max} \left(1 - x_{6MH} \frac{P_{Mem}}{P_{Mem,max}} \right) - P_{Ad} - \frac{P_{PreAd}}{n_{PreAd}} \right) \\ & + k_{Ad} \cdot (n_{PreAd} - 1) \cdot P_{PreAd} \end{aligned} \quad (4.6)$$

$$\begin{aligned} \frac{dP_{PreAd}}{dt} = & +k_{PreAd} \cdot P_{Sol} \cdot \left(P_{Ad,max} \left(1 - x_{6MH} \frac{P_{Mem}}{P_{Mem,max}} \right) - P_{Ad} - \frac{P_{PreAd}}{n_{PreAd}} \right) \\ & - k_{Ad} \cdot n_{PreAd} \cdot P_{PreAd} \end{aligned} \quad (4.7)$$

The second step treated as an auto-catalytic incorporation (reaction 4.5) requires a slow random insertion of single EB molecules defined as a stochastic incorporation (reaction 4.4). The stochastic step is represented in equation 4.8, described as a Langmuir-like process, which takes into account only the free-spaces in the lipid bilayer. The concentration of (P_{Ad}) depends on three processes. It increases due to the formation of the monomeric species, decreases due to the stochastic process, and decreases with auto-catalytic insertion into the membrane core.

$$\begin{aligned} \frac{dP_{Ad}}{dt} = & +k_{Ad} \cdot P_{PreAd} \\ & -k_{Inc} \cdot P_{Ad} \cdot (P_{Mem,max} - P_{Mem}) \\ & -k_{Mem} \cdot P_{Mem} \cdot (P_{Mem,max} - P_{Mem}) \cdot P_{Ad} \end{aligned} \quad (4.8)$$

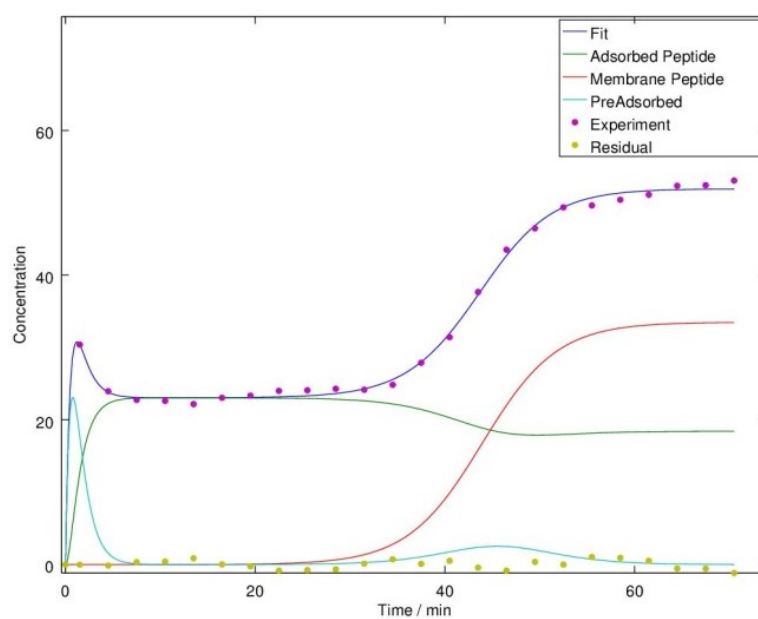
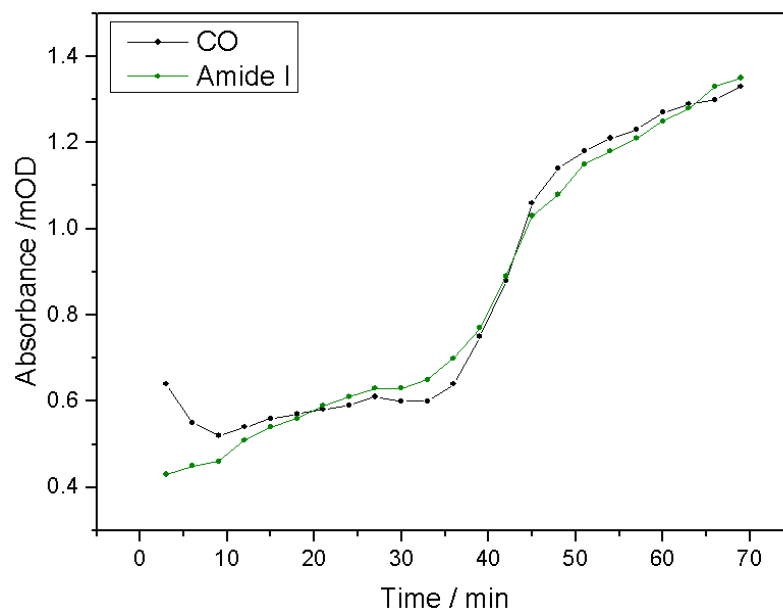


Figure 4.28. Kinetic representation of the SEIRA absorbance (mOD) of the CO and amide I bands (purple dots) against time (min) during the EB:Na⁺ complex incubation in 100mM NaCl 20mM BTP pH7.4 buffer at 25° C. In purple line there is the fit curve. The green line corresponds to the adsorbed-peptide, the red line to the peptide in the membrane, and the light blue line to the pre-adsorbed species. The yellow dots represent the residuals of the fitting.

The auto-catalytic incorporation is described as a Prout-Tompkins kinetics, expressed in the first term of equation 4.9. This stage is concentration-dependent, since it is necessary for the adsorbed EB on the surface (P_{Ad}) to establish contact with the already incorporated species (P_{Mem}) for insertion into the membrane.

$$\begin{aligned} \frac{dP_{Mem}}{dt} = & +k_{Mem} \cdot P_{Mem} \cdot (P_{Mem,max} - P_{Mem}) \cdot P_{Ad} \\ & +k_{Inc} \cdot P_{Ad} \cdot (P_{Mem,max} - P_{Mem}) \end{aligned} \quad (4.9)$$

The differential equations provided a very good fit to the CO band (experimental data) of the Na^+ complex, shown in bottom of figure 4.28 (purple line). The red line demonstrates the SEIRA intensity of membrane-incorporated EB, and the light blue and green refer to the (P_{PreAd}) and (P_{Ad}) species, respectively. These results indicate that the proposed mechanism for the membrane-binding process is consistent with the experimental data. To achieve a good fit to the data, the previously described water-correction had to be performed beforehand. The fact that the fit yielded the observed good result supports the suitability of water-correction in the case of EB.

The same analysis of data was applied to the amide I band of the $EB:Na^+$ complex, as well to the incubation of the $EB:K^+$ complex. The analysis of the incubation of both complexes is presented in a comparative manner in figure 4.30 (red lines). The light green line represents the interfacially adsorbed aggregates (P_{PreAd}); the dark green line the interfacially (P_{Ad}) "monomer/complexes"; and the blue line the incorporated species (P_{Mem}). The two complexes differ significantly in their binding kinetics in which Na^+ shows an "auto-catalytic" process whereas for K^+ membrane binding is significantly accelerated. These results support the suggestion of different stoichiometry for these two ions, 1:1 for Na^+ and 2:1 for K^+ , since different ion-coordination might lead to different kinetics. Another interesting observation is that in both cases the band ratio maintains constant during the incubation time. Comparing to the SEIRA results in the independent incubation of the ion complexes, Na^+ complex shows pronounced changes in band ratio after incubation (0.52 to 0.85) whereas the band ratio for the K^+ complex is preserved (0.72 to 0.71). A tentative interpretation might be that this is a result from the different interaction between EB rings in the interfacially space and those being incorporated into the membrane core for the Na^+ complex compare to the K^+ complex. In the case of Cs^+ the kinetics could not be fit to the presented model, which may suggest an even slower incorporation into the tBLM.

The intensity evolution of the peptide bands during the ion-exchange experiment is presented in figure 4.31 together with the band ratio analysis, both as a function of time. Interestingly, when exchanging the ions from Na^+ , to Cs^+ and then to K^+ , there is a decrease in the intensity of both bands in the beginning followed by an increase over time. On the other hand, the inverse happens during the evolution of the band ratios, which show a fast increase accompanied by a quick decrease and stable value in

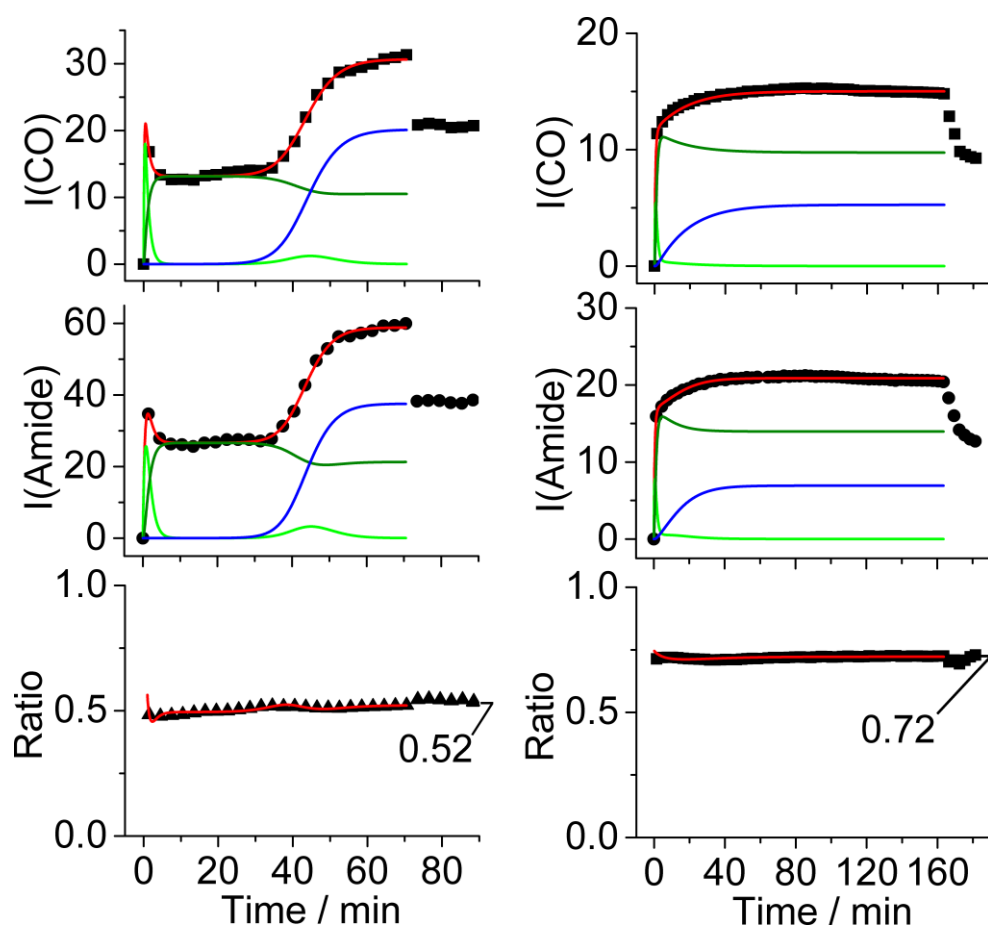


Figure 4.30. Kinetic representation of the SEIRA absorbance (mOD) of the CO and amide I bands (black dots) against time (min) during the EB:Na⁺ and EBK⁺ complex incubation at 25° C. In red line there is the fit curve. The dark green line corresponds to the adsorbed-peptide, the blue line to the peptide in the membrane, and the light green line to the pre-adsorbed species. The bottom representations are the band ratio for each complex.

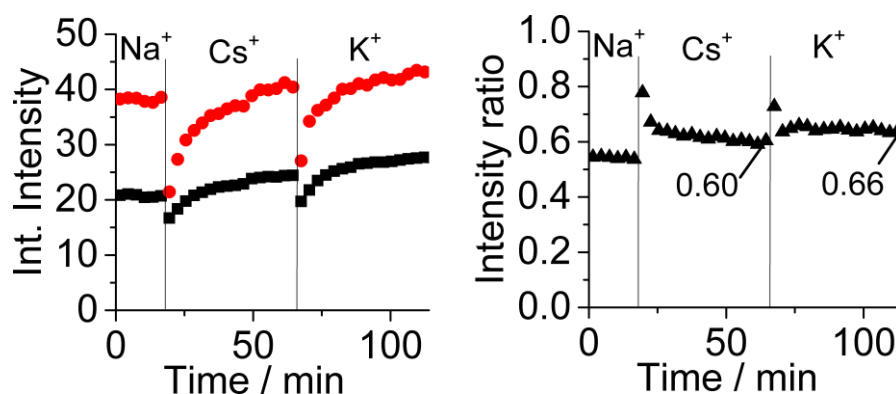


Figure 4.31. Kinetic representation of the SEIRA absorbance (mOD) of the CO (black dots) and amide I (red dots) bands against time (min) during the ion-exchange at 25° C (left graph). The graph on the right is a representation of the band ratio for each complex.

both exchange processes. Even though no structural information can be drawn from these observations, one plausible interpretation for this phenomenon is the migration of EB molecules to the membrane-solution interface in order to coordinate ions. This fact reflects the mobility of EB within the membrane and the great capability of the peptide to facilitate ion transport.

4.2.4. Conclusions

The SEIRA spectroscopy, kinetics and theoretical calculations results presented in this work provide novel insights into the structural understanding of the EB peptide. The interpretations made here attempt to bring more light into the controversial characterization of EB ion complexes, membrane interaction and mechanism of action. The main conclusions are summarized down below.

The peptide-membrane interaction of EB characterised by SEIRA spectroscopy using tBLM systems involves different binding processes, which depend on the peptide concentration and on the ion available. The findings presented here demonstrate the membrane incorporation of EB complexes into the lipid bilayer. The kinetics of this interaction is represented by the suggested binding mechanism, where multimer pre-adsorbed species are bound to the surface, followed by an auto-catalytic incorporation process. The Na⁺ ion complex successfully exemplified this mechanism, which showed to differ from the binding process observed for the K⁺ ion and thus, denoting the presence of different species. Additionally, the kinetics observed during the ion-exchange provided evidence for the EB capability to form ion-transport and travel through the membrane.

The ion affinity evaluation by the SEIRA spectroscopy showed a higher affinity of EB to K⁺ ion. However, the **ion selectivity** was significantly lower than what is suggested for the well-known Valinomycin or Beauvericin [61]. This was evident in the back reaction from K⁺ complex to Na⁺, denoting an interesting degree of reversibility between the two. The partial reversibility and affinity might have a great impact in the peptide mechanism of action, since in *in vivo* conditions the homeostasis between these two ions is essential for the cell. Thus, a deregulation in the concentration of these ions between the intra and extracellular space can lead to membrane permeability, and later, to cell apoptosis. This is a plausible hypothesis suggested for the antimicrobial activity of EB, which depends on the peptide concentration and ion availability, as explained in the kinetics analysis.

Complex stoichiometry has been one of the most debated features of EB. This study offers a new interpretation on EB ion complex formation. The SEIRA and IR spectroscopy combined with the DFT calculations revealed that EB is likely to form a 1:1 complex with Na⁺ and a 2:1 complex with K⁺ and Cs⁺. The DFT results, structure and spectra, showed the formation of the 2:1 EB: K⁺ complex in which the C=O ligands from the *N*-methyl-L-valine residues contribute predominantly to the coordination of the ion,

which is in agreement with the findings by Ovchinnikov et al. for a 2:1 stoichiometry [61]. The results for the Na⁺ and Cs⁺ ions were less clear, both showed same peptide bands in the SEIRA spectra with slight variance in intensity. However, the consistent shifts of the EB bands in SEIRA when exchanging the buffer solution containing K⁺, supports the assumption that these Na⁺ and Cs⁺ ions present a similar contribution of the C=O ligands that is distinctly different to the EB conformation adopted in the K⁺ complex. Consequently, taking into consideration the results provided, the present study suggests the following complex stoichiometry for the three ions evaluated:

1:1 for EB:Na⁺

2:1 for EB:K⁺

2:1 for EB:Cs⁺

mechanism of action interacting with tBLM systems. This work, combined with previous structural and functional studies of the peptide, opens new possibilities for the interpretation and prediction of EB complexes stoichiometry.

4.3. Antimicrobial peptide arenicin1

In this section, the POPC/POPG tBLM system was used as membrane-mimetic system to study the AMP arenicin1 (A1) by SEIRA spectroscopy. This cationic AMP contains features that are interesting for a spectroscopic evaluation. It is characterised by an antiparallel β -sheet conformation with nine intrabackbone hydrogen bonds (H-bonds). The high percentage of hydrophobic amino acids can explain the interaction with lipids in the membrane. The (6+) net charge is given by arginine (Arg) amino acids distributed along the peptide, achieving a high amphipathic surface. The disulphide bridge between the Cys in position 3 and 20 closes a loop of 18 residues. The A1 peptide has shown antimicrobial activity against gram-negative bacteria suggested to be a pore forming peptide, whose activity was increased at 4° C and 37° C [63]. The scarce literature presenting the peptide-membrane interaction leaves plenty of room for mechanistic investigations. Here, a series of vibrational spectroscopy experiments provided complementary structural information to the SEIRA study performed at three temperatures: 4° C, 25° C and 37° C. The preliminary results of the molecular dynamic (MD) simulations of A1 using a POPC/POPG membrane in similar conditions to the SEIRA experiments are presented at the end of the section. As a result, this investigation offers the foundation for a structure-function study of the peptide-membrane interaction of A1 under different conditions using the POPC/POPG tBLM system.

4.3.1. IR and Raman spectroscopy of arenicin 1

The IR and Raman experiments were performed to obtain an overview of the peptide features in solid and solution state without the membrane environment.

4.3.1.1. ATR-IR spectroscopy of solid arenicin 1

This measurement was done with a solid sample of A1, using a diamond-ATR-IR setup. The resulting spectrum is shown in figure 4.32. Here, the peptide is static, but distributed in a preferential direction within the powder. The powder is actually composed of crystals of A1, which in consequence gives a certain orientation. The bands assigned in the spectrum represent a β -sheet structure with a turn, as described in literature [19] [36]. It is possible to divide the spectrum in three regions: the high region from 3300 to 2700 cm^{-1} , the amide region from 1800 to 1500 cm^{-1} , and the lower region from 1400 to 500 cm^{-1} . In the high region there is a broad band at 3277 cm^{-1} representing the ν (NH) stretching mode, known as well as amide A band, which is part of a Fermi resonance doublet with the second component at ca. 3100 cm^{-1} [39]. Between 3000 and 2700 cm^{-1} there are weak bands corresponding to the symmetric and asymmetric ν (CH)_n stretching modes. It is important to notice the absence of the 2600 cm^{-1} band of the ν (SH) stretching mode, which indicates that all sulphur atoms are forming a disulphide bridge (S-S) closing the loop in the peptide.

The assignments for the bands below 1800 cm^{-1} are described in table 4.9. The amide region presents multiple bands due to coupling of the amide I and amide II vibrational modes. The amide I band appears to be split into two components, a strong band at ca. 1630 cm^{-1} and a weaker band at ca. 1695 cm^{-1} . The former having a main contribution from the out-of-phase ν (C=O) stretching mode [111]. The transition dipole moment of these bands presents a certain orientation in respect to the direction of propagation of the chain. The main absorption at 1630 cm^{-1} corresponds to the

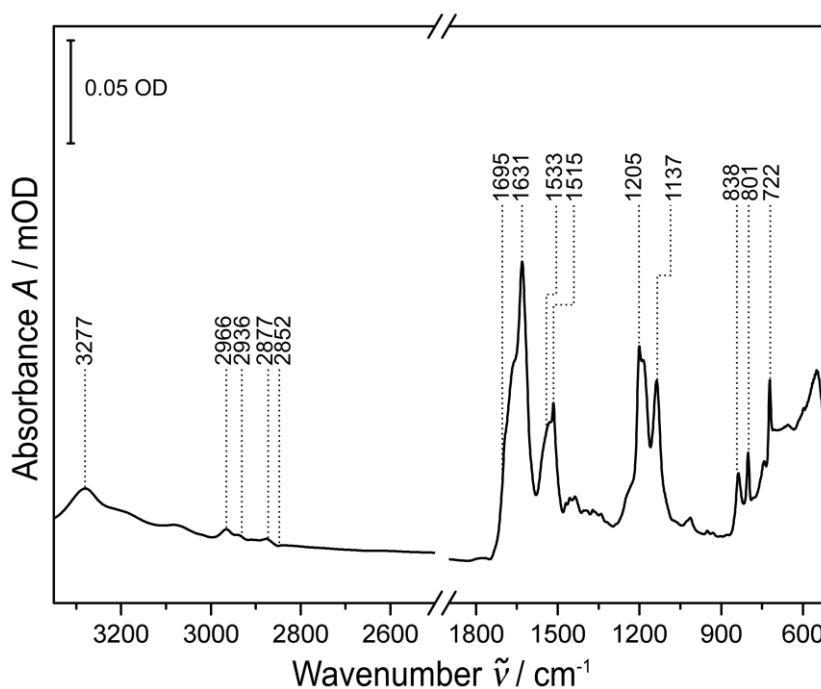


Figure 4.32. ATR-IR spectrum of the solid state of A1 peptide. The assignments of the corresponding vibrational modes are presented in table 4.9.

transition dipole moment perpendicular to the chain direction, and the weaker parallel to the chain [39]. The amide II band (in-phase ν (C-N) stretching and (N-H) bending modes) is split as well, with a strong band at ca. 1558 cm^{-1} and a weak broad band at 1533 cm^{-1} , corresponding to the parallel and perpendicular polarization of the transition dipole moment, respectively [21]. The sharp band at ca. 1515 cm^{-1} is assigned to the strong (C-C) ring vibrational mode from Tyr (tyrosine) [114].

Table 4.9. Band assignment for the A1 vibrational modes in the ATR-IR spectrum in figure 4.32. Band characteristic indicated in the position as: W, weak; B, broad; S, strong; M, medium [19] [38] [39] [112] [113].

Position (cm^{-1})	Description
1695 _W	Amide I (minor component)
1668 _B	B-turn
1653	Unordered structure
1631 _S	Amide I (major component)
1558	Amide II (major component)
1533	Amide I (minor component)
1515 _S	C-C aromatic ring breathing Tyr
1202 _S	Indole ring stretching Trp
1183 _S	COH deformation (sensitive to H-bonding)
1137 _S	NH indole deformation
838 801	Tyr Fermi doublet
722 _M	Rocking of adjacent in-phase CH_2 couple

In the lower region from 1500 cm^{-1} there are small bands corresponding to the $(\text{CH})_n$ bending and rocking vibrations, (NH) deformation, and other amino acid side-chain characteristic bands. The band marked at 1205 cm^{-1} has a left-shoulder, which indicates an overlap between the amide III ((CN) stretching and (NH) bending, usually 1220 cm^{-1}) and the strong vibration from the (C-C) indole ring from Trp (Tryptophan) at 1203 cm^{-1} [39]. The low-frequency shoulder of the latter band may overlap with modes including wagging and deformation coordinates of CH_2 and COH groups [39]. The band at 1137 cm^{-1} corresponds to a (NH) indole deformation mode. The bands at 838 and 801 cm^{-1} are assigned to the Fermi doublet of Tyr. The band at 722 cm^{-1} is assigned to the in-phase mode coupling of adjacent CH_2 groups from the side chains [39].

4.3.1.2. FT-Raman spectroscopy of solid arenicin 1

FT-Raman spectroscopy can offer a complementary analysis of the vibrational modes of the peptide. In that way, modes that are not IR active can be Raman active, and some modes can be active for both techniques. While the rule for IR active modes depends on the change on the transition dipole moment with a normal coordinate, Raman activity requires a change in the polarizability. The Raman spectrum of a solid sample of A1 is shown in figure 4.33. This spectrum shows the $\nu(\text{CH})_n$ stretching modes in the region from 3062 to 2713 cm^{-1} ; they are more intense in Raman than in IR due to the great change in polarizability of these groups. In the Raman spectrum of A1, there is absence of the SH vibrational mode (2550-2600 cm^{-1}) as shown as well in IR. The assignment of the bands in the region between 1700 and 500 cm^{-1} , are shown in table 4.10. There are important bands to be mentioned, like the $\nu(\text{C}=\text{O})$ stretching at 1671 cm^{-1} and the Fermi doublet at 836 cm^{-1} and 801 cm^{-1} , both characteristic modes of Tyr. The Trp characteristic bands appear at 1551 cm^{-1} (NH deformation) and 1011 cm^{-1} (indole ring breathing). The (C-S) and (S-S) modes of Cys and the disulphide bridge at 670 and 504 cm^{-1} , respectively. Combining both analysis, IR and Raman, it was possible to offer a detailed fingerprint of the A1 peptide composition.

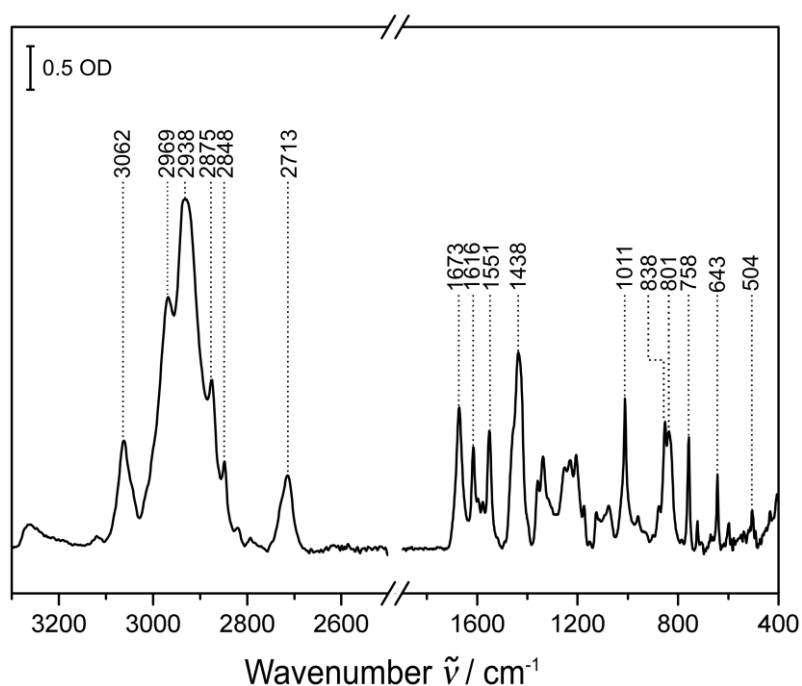


Figure 4.33. FT-Raman spectrum of solid state A1 peptide.

Table 4.10. Band assignment for the A1 vibrational modes in the Raman spectrum in figure 4.33. Band characteristic indicated in the position as: W, weak; B, broad; S, strong; M, medium [114] [115] [116].

Position (cm ⁻¹)	Description	Position (cm ⁻¹)	Description
1671 _s	Tyr C=O stretching (amide I)	1150	Ring deformation
1616 _s	Tyr Aromatic ring from	1126	Trp NH deformation indole
1597	CO asymmetric stretching	1075 _w	Trp C-H scissoring pyrrole ring
1578	COO ⁻ asymmetric stretching	1011 _s	Trp indole ring breathing (strong Van der Waals interactions)
1551 _s	Trp NH deformation	960	Trp C-H twisting benzene ring
1517 _w	Tyr Aromatic ring stretching	878	Trp C-H scissoring indole ring
1460	CH ² deformation		Trp C-H bending pyrrole ring ca. 849
1360		853	Tyr ring breathing
1438-1424	CH ² scissoring and Trp indole ring stretching	836 _B 801	Tyr Fermi doublet
1338-1360	Trp Fermi resonance doublet (in a hydrophilic environment)	758 _s	Trp indole ring breathing
1255	Trp C-H rocking of benzene	670 _w	Cys C-S stretching
1230	Amide III (β-sheet) and Tyr O-C ring stretching	643 _s	Tyr ring deformation
1205	Tyr C ring stretching p-substituted benzene	599	Trp pyrrole ring deformation
1174 _M	CH deformation indole ring Trp	504 _w	S-S stretching

4.3.1.3. FT-IR transmission of arenicin1 in solution

A sandwich FT-IR transmission setup was used to measure a saturated solution of A1 in NaCl-BTP buffer. The resulting spectrum is shown in figure 4.34. The spectrum shows similar features in the amide region as for the solid state, but with broader bands. As in the solid state IR, A1 exhibits a β-sheet structure, which reflects the high instability of the peptide in the different conditions [63]. The assignment of the main bands appearing in the amide region is shown in table 4.11. The amide II region appears like a big broad band, but actually it is an overlap of at least three bands at 1561 cm⁻¹, 1532 cm⁻¹, and the more defined band at ca. 1516 cm⁻¹ for the Tyr ring. Unfortunately, it is more difficult to discriminate the bands in the lower region in the solution spectrum, which is due to the lower concentration of A1 as well as the broadening of bands sensitive to H-bonding. The A1 solution spectrum gives a closer idea of what can be expected in the SEIRA spectra.

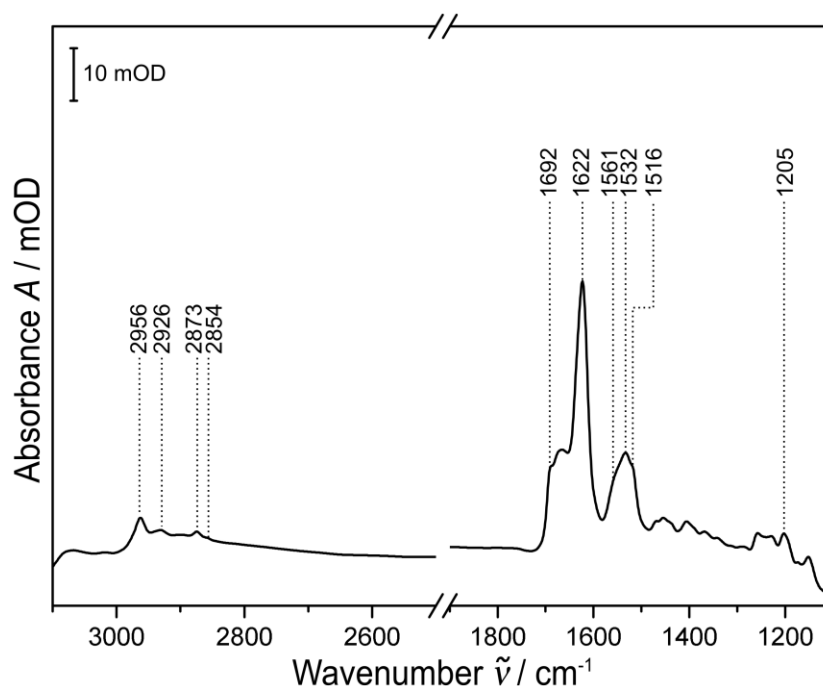


Figure 4.34 FT-IR transmission difference spectrum of the saturated solution of A1 in 100 mM NaCl 20 mM BTP pH 7.4 buffer at room temperature.

Table 4.11. Band assignment for the A1 vibrational modes in the FT-IR transmission spectrum in figure 4.34. The symbols // and \perp indicate a parallel or perpendicular direction, respectively.

β -sheet amide bands (cm^{-1})		
1692	main Amide I	// to sheet direction
1680	β -turn	
1622	minor Amide I	\perp to sheet direction
1561	minor Amide II	\perp to sheet direction
1532	main Amide II	// to sheet direction

Summary

The analysis of the A1 powder by ATR-IR and Raman spectroscopy, offered a fundamental description of the peptide structure and composition. The information collected revealed a β -sheet conformation of A1, and vibrational modes of distinctive amino acid side chains. The bands corresponding to Trp and Tyr amino acids can be used for the interpretation of intra-strand interactions, for example the 1011 cm^{-1} band of Trp in the Raman spectrum representing strong van-der-Waals interactions. On the other hand, the FT-IR transmission spectrum in solution shows the hydrophilic character of the peptide reflected in the broadening of the main amide bands due to interaction with the solution. Overall, this section offered a complete analysis of the A1 peptide structure as a starting point for the SEIRA study.

4.3.2. SEIRA and EIS study of the POPC/POPG membrane systems

The construction of the tBLM with POPC/POPG lipids was done following the same steps as for the pure POPC system, aiming a 80:20 ratio of lipid molecules. The main difference is the mix of POPC with the negatively charged POPG lipids, which required the addition of a polar solvent to the preparation. The resulting SEIRA difference spectrum of the 80:20 POPC/POPG tBLM at 25° C is shown in figure 4.35 (black spectrum). Both lipids have the same aliphatic chains composition (same melting point transition temperature, - 2° C), which results in equivalent band positions and shape as for the pure POPC tBLM. Due to the temperature requirements during the study of A1 peptide, the tBLM system was evaluated at three temperatures: 4° C, 25° C and 37° C, as shown in figure 4.35. The POPC/POPG tBLM system spectrum is conserved in the regions of interest for the three temperatures, allowing for the analysis of the peptide bands at each condition. However, it was possible to observe temperature effects on the silicon prism in the low frequency region below ca. 1500 cm⁻¹ (see appendix figure A.7 for full spectra), where bands appear like a mirror effect, positive at 37° C and negative at 4° C.

POPC/POPG tHLM membrane systems

The lipid monolayer was built in the same way as for the POPC tHLM system presented in section 5.2.1. First, a pure WK3SH SAM was assembled on the Au-film. Afterwards, the POPC/POPG lipid vesicles were added. The SEIRA difference spectrum of the

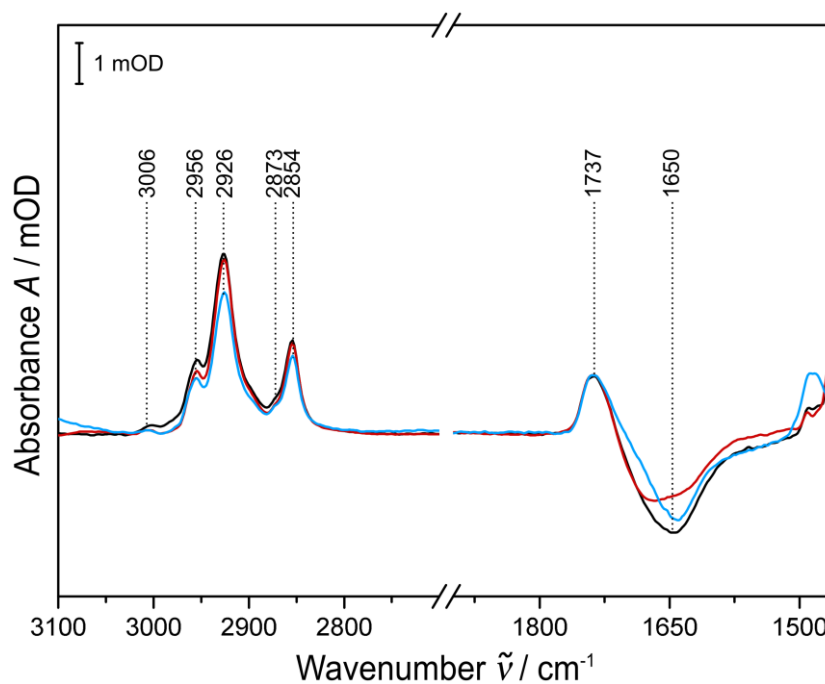


Figure 4.35. SEIRA difference spectra of the POPC/POPG tBLM at 4° C (blue), 25° C (black) and 37° C (red), using the SAM spectra as reference.

POPC/POPG tHLM system resembles the one for bilayers, but with slight lower intensities (data not shown).

EIS of the POPC/POPG tBLM and tHLM systems

The impedance data and its representation were treated in the same way as for the POPC systems. Figure 4.36 shows the comparison of EIS spectra of both tBLM systems. The values obtained from the fitting of the Cole-Cole plots of the POPC/POPG systems are presented in table 4.12. The high percentage of POPC lipids in the mix and the similarity of the two lipids are reflected by similar capacitance values of the bilayer and the total system, C_{bilayer} and C_{system} respectively, for both tBLM and tHLM. The capacitance of the system for the POPC/POPG tBLM was $(0.61 \pm 0.02) \mu\text{F cm}^{-2}$, which is in the range of the pure POPC tBLM $(0.62 \pm 0.03) \mu\text{F cm}^{-2}$. The tHLM capacitance was slightly lower than for the pure POPC, $(0.66 \pm 0.08) \mu\text{F cm}^{-2}$ instead of $(0.70 \pm 0.06) \mu\text{F cm}^{-2}$, but still consistent considering the errors. These results are coherent since the only difference in the system is the negatively charged POPG lipid.

Table 4.12. Results from the EIS analysis obtained by the fitting of the spectra to the equivalent circuit described for the POPC/POPG tBLM and tHLM systems.

	R_{Solvent} Ω	R_{bilayer} $\text{K}\Omega \text{ cm}^2$	C_{bilayer} $\mu\text{F cm}^{-2}$	R_{spacer} $\text{K}\Omega \text{ cm}^2$	C_{spacer} $\mu\text{F cm}^{-2}$	Q $\mu\text{F s}^{\alpha-1} \text{ cm}^{-2}$	α	C_{system} $\mu\text{F cm}^{-2}$
tBLM	337.2	2.00	1.81	325.6	4.81	6.04	0.82	0.61
tHLM	190.4	2.09	3.00	414.1	5.07	9.58	0.78	0.66

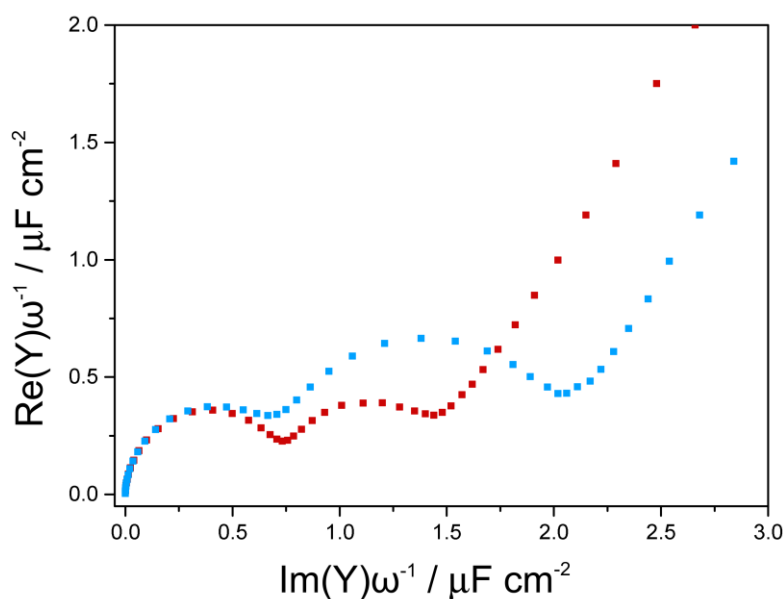


Figure 4.36. Impedance spectra represented in a Cole-Cole plot for the POPC/POPG tBLM (light blue) and the POPC tBLM (red).

4.3.3. Peptide-membrane interaction study by SEIRA

4.3.3.1. Arenicin1 interaction with POPC/POPG tHLM system.

As initial approach, A1 was incubated at 37° C with the POPC/POPG tHLM system to test the peptide interaction with a lipid monolayer. The SEIRA difference spectrum is shown in figure 4.37. For the first time, it was possible to observe the A1 β -sheet structure in SEIRA spectroscopy using a tHLM system. Interestingly, the amide region of the spectrum resembles quite well the spectrum obtained by the FT-IR transmission experiments of the solution sample of A1. The changes in the position of some of the bands are attributed to the interaction of the peptide with the membrane. The main absorption of the amide I mode appears at 1630 cm^{-1} and the weaker absorption at 1691 cm^{-1} . In between these two bands there is a broad band at ca. 1677 cm^{-1} assigned to the β -turn conformation. The two components corresponding to the amide II mode are at ca. 1562 cm^{-1} (strong band) and at 1532 cm^{-1} (weaker band). The band at 1516 cm^{-1} corresponds to the stretching mode of the aromatic ring of Tyr, as shown in the solid and solution spectra, this band is a marker for this residue. On the high-energy side of the spectrum, the $(\text{CH})_n$ vibrational modes appear as negative bands, which may indicate changes in the lipid orientation due to the interaction with A1. The region below 1400 cm^{-1} seems to be conserved compared to the FT-IR transmission spectrum. These preliminary results show the capability of A1 to interact with a lipid monolayer and to disturb the system (after 5 hours incubation).

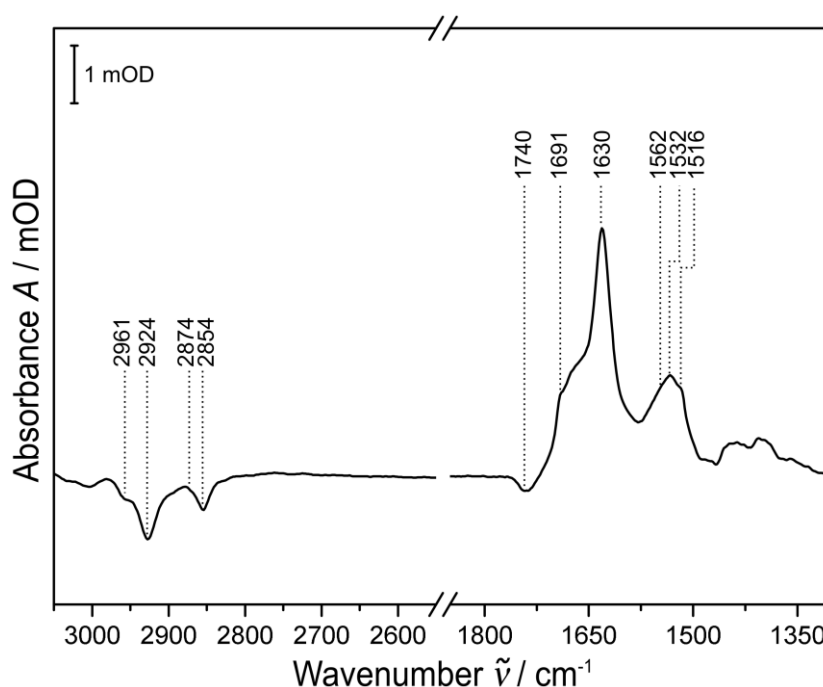


Figure 4.37. SEIRA spectrum of the A1 peptide interacting with POPC/POPG lipid monolayer, using the tHLM spectrum as reference.

4.3.3.2. SEIRA spectroscopy of arenicin1 interaction with POPC/POPG tBLM system: temperature dependence

As explained in the beginning of the section, this study aimed to evaluate the behaviour of A1 in presence of the POPC/POPG tBLM at three temperatures, 4° C, 25° C, and 37° C. The SEIRA difference spectra of the independent incubation of A1 at each temperature, after 3 hours, are presented in figure 4.38. The second derivatives of the spectra revealed that the bands appear in the same amide band position for the three temperatures. In none of the cases there is a band for the (SH) mode, which means all Cys residues are connected closing the peptide loop. Contrary to what was observed above for the tHLM system, the lipid bands at ca. 1737 cm⁻¹ (doublet for the COO⁻ of the lipids) and those in the (CH)_n region are positive in this case. In both membrane systems A1 causes changes in the lipid organisation as a result of the

interaction. It is possible to identify lipid changes in the high region due to the difference in band shape; For the lipids the bands corresponding to the asymmetric and symmetric stretching mode of the CH₂ groups are of higher intensity, while the peptide (amino acid side-chains) shows higher intensities for the asymmetric and symmetric modes of the CH₃ groups. Although the differences between the three temperatures were less pronounced than expected, the SEIRA spectra suggest that A1 activity increases with the temperature.

Even if, at first glance, the amide region of the spectra might look different than for the tHLM, the band position matches to the characteristic bands for the β -sheet structure

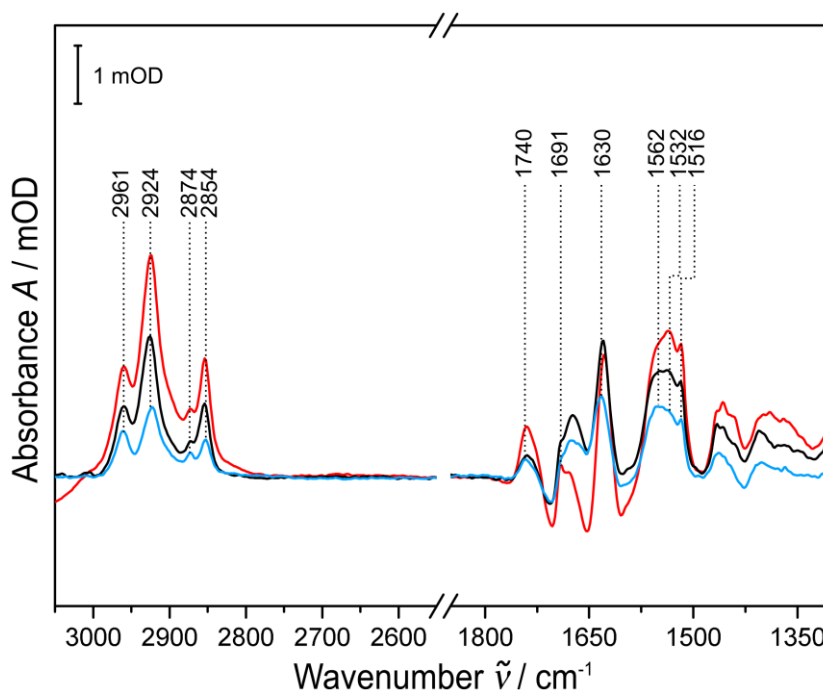


Figure 4.38. SEIRA spectra of the A1 peptide binding to the lipid bilayer, tBLM spectrum was used as reference. The experiment was performed at three different temperatures: 4° C (blue), 25° C (black), and 37° C (red).

described in the monolayer evaluation (second derivative assignment). The interference of water is the likely reason for the variation of the baseline in the amide region. The water interference along with the lipid band changes indicates the ability of A1 to disturb the membrane in a deeper manner than for the tHLM system. In other words, due to the interaction of A1 with the lipid bilayer water leaks through the membrane, which is reinforced by the water overlapping in the amide region and the positive band of the OH stretching at ca. 3450 cm^{-1} (data not shown). As suggested by Andrä et al. (2008) [63], these alterations can be considered as partial lesions in the membrane integrity. Additionally, the interaction of A1 with the lipids is practically spontaneous showing changes in the lipid bands of the SEIRA spectrum after just three minutes of incubation. This observation indicates that A1 is likely to induce membrane permeabilisation by a toroidal pore formation [117] or by a carpet model mechanism as suggested in [63], where accumulated membrane lesions of the affected cells *in vitro* resulted in the realising of cytoplasmic material. On the other hand, the results presented here offer an evaluation of A1 in different states and conditions, and it was demonstrated that A1 is highly stable and conserves its β -sheet structure in solid, solution and lipid environment, which disagrees with the observations by Andrä et al. (2008) [63].

Potential dependence study of arenicin1

The aim of the potential-dependence analysis was to evaluate the changes induced by potentials applied to the system containing A1. The resulting SEIRA difference spectra at 25°C using the $+400\text{ mV}$ spectrum as reference are shown in figure 4.39. The red spectrum depicts minimal changes in the amide region at $+300\text{ mV}$. However, when applying lower potentials the changes in the amide I band increase, most marked at 1630 cm^{-1} . The high frequency region shows practically no change, as well as in the low region below 1600 cm^{-1} . The changes induced by negative potentials were not reversible as shown by the spectrum measured after applying $+400\text{ mV}$ again. The changes were visible even after hours under open circuit conditions. It is possible to conclude that these changes originate from the peptide and not from the background by comparing the data to the potential control experiment shown in figure 4.40. The solution beneath the lipids in the tBLM increases by applying negative potentials, as described in Kozuch, Jacek PhD dissertation [21]. This is observed in the increase of the intensity of the (OH) stretching and bending modes from water during the application of negative potentials.

In the next step, the same experiment was performed at 37°C . The SEIRA difference spectra are shown in figure 4.41, using the $+400\text{ mV}$ spectrum as reference. This time changes were significantly pronounced, not only in the amide region, but also in the $\nu(\text{CH})_n$ stretching frequency region. The bands in the high region represent a strong perturbation of the lipid bilayer arrangement, reflected as well in the raise of the $\nu(\text{CO})$ stretching band at 1737 cm^{-1} . In this case, the changes of the amide I band are negative indicating an apparent re-orientation of A1 in the membrane. The increasing $\nu(\text{OH})$ stretching band from water adds evidence to the permeabilisation of the

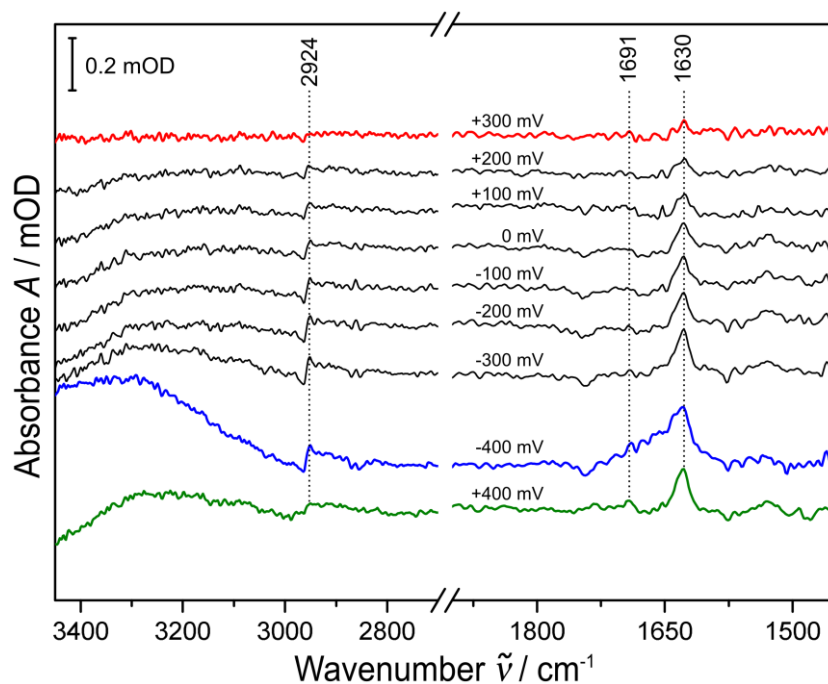


Figure 4.39. SEIRA spectra of the A1 peptide after applying potentials from +400 mV to -400 mV (blue) in 100 mV steps, using the POPC/POPG tBLM system, measured at 25° C as reference. The +400 mV (green) potential was applied again as a last step. All difference spectra are calculated using the first +400 mV spectrum as reference.

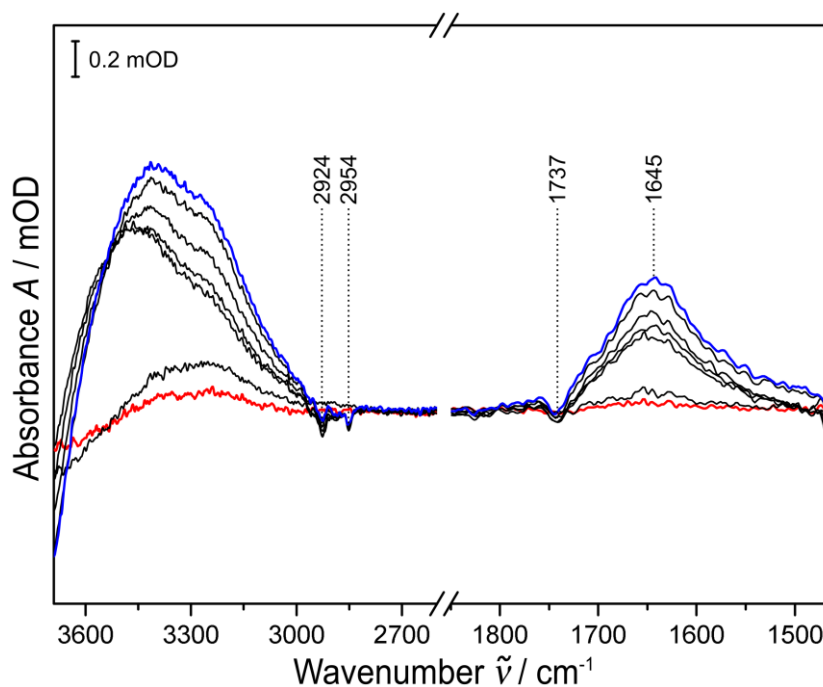


Figure 4.40. SEIRA spectra of the tBLM potential control experiment. Potentials were applied from +400 mV to -400 mV (blue) in 100 mV steps. All difference spectra are calculated using the first +400 mV spectrum as reference, and measured at 25° C.

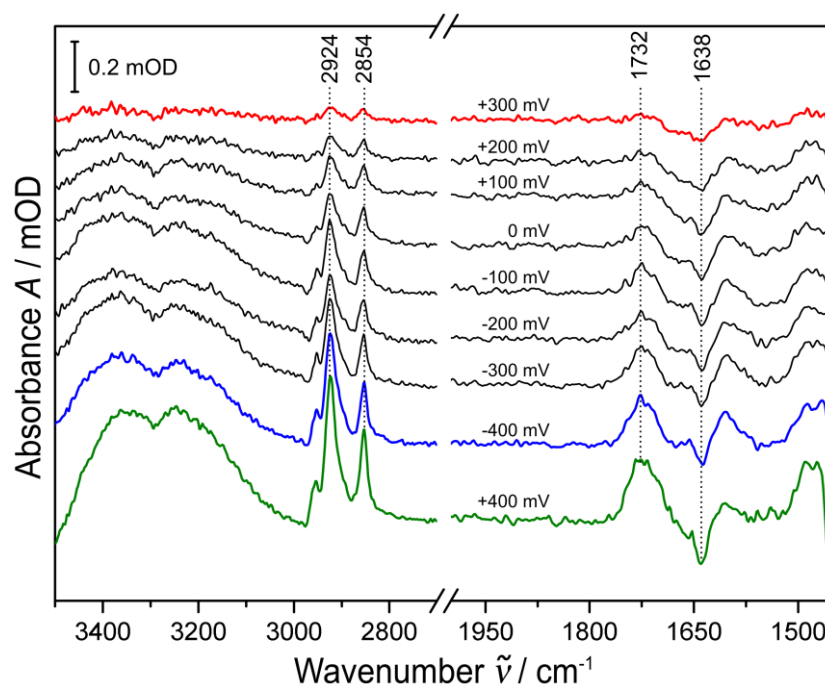


Figure 4.41. SEIRA spectra of the A1 peptide after applying potentials from +400 mV to -400 mV (blue) in 100 mV steps, using the POPC/POPG tBLM system, measured at 37° C. The +400 mV (green) potential was applied again as a last step. All difference spectra are calculated using the first +400 mV spectrum as reference.

membrane. As shown at 25° C, the changes induced upon the application of negative potentials were irreversible and the variations continued after two hours. As overall observation, applying negative potentials enhanced the membrane perturbation activity of A1, which was more evident at 37° C than at 25° C.

4.3.4. Molecular dynamics simulation of arenicin1

In order to provide atomistic details regarding the behaviour of A1 in solution together with the interaction pathway in a lipid environment, all-atom MD simulations of the peptide (pdb-code 2JSB [63]) employing CHARMM force field were performed. The investigation was mainly focus on: i) comparative conformational study of the natural peptide and an analogue without S-S bridge, ii) evaluation of possible dimerization, and iii) peptide-membrane interaction.

The trajectories showed that both A1 monomers, natural and analogue, adopt an antiparallel β -sheet with β -turn secondary structure (see figure 4.42). There was not significant difference between the trajectories of both A1 monomers. Interestingly, inter-strand H-bonds and non-covalent interactions, like the π -interaction between Arg16 and Tyr5, are responsible for the overall stabilisation of the structure of both A1 monomers throughout the 300 ns of simulation. This great stability of A1 is in line with the

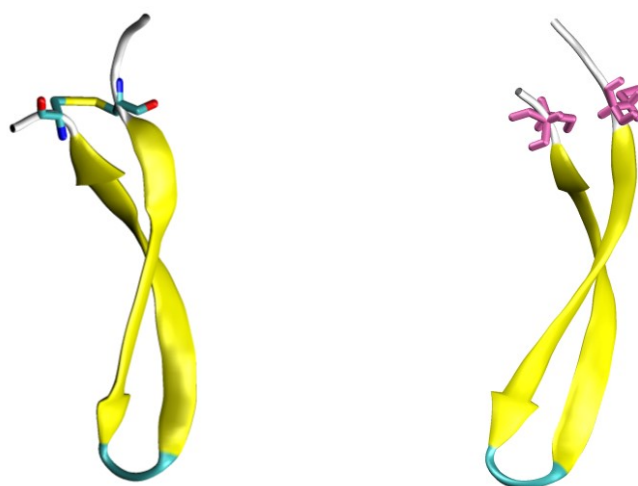


Figure 5.42. snapshots of 3D representation of the cationic AMP A1 (left) and its analogue without cys S-S bridge (right). Yellow colour denotes the antiparallel β -sheet conformation while the β -turn is depicted in turquoise. The N- and C-terminal regions are unstructured represented in white colour. The disulphide bond between Cys3 and Cys20 is shown in yellow forming a loop in the peptide. The Cys 3 and 20 are depicted in mauve colour in the analogue peptide.

spectroscopic results obtained from the solid, solution and tBLM experiments presented here.

The dimerization of the natural A1 (S-S bridge) in solution takes place during the first 60 ns of the MD simulation (see figure 4.43). The main interactions between the two monomers were observed as π -interactions (at distance $< 3 \text{ \AA}$) between Trp2-Val15 and Trp21-Val10 (turn), as well as interactions involving residues Val4, Tyr5, Tyr7 and Arg19 of one monomer and Val13, Tyr17 and Tyr7 of the other monomer. Dimerization was not observed for the peptide without the disulphide bridge, although there appeared random interaction (at distance $< 3 \text{ \AA}$) towards the end of the simulation, between the ring of Trp21 and Arg1 (shown in appendix figure A.8).

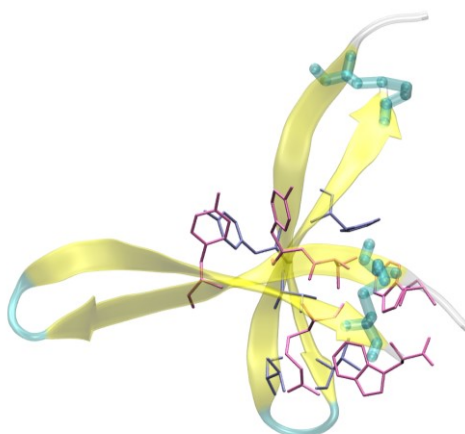


Figure 5.43. Snapshot of a 3D representation of the cationic AMP A1 dimer in solution. The secondary structure is shown in similar colour-code as the natural monomer in figure 4.42, but in a more transparent manner to emphasise the side chain of the aromatic residues involved in the dimerization process. The side chain of Trp and Tyr are depicted in mauve and violet colour, respectively.

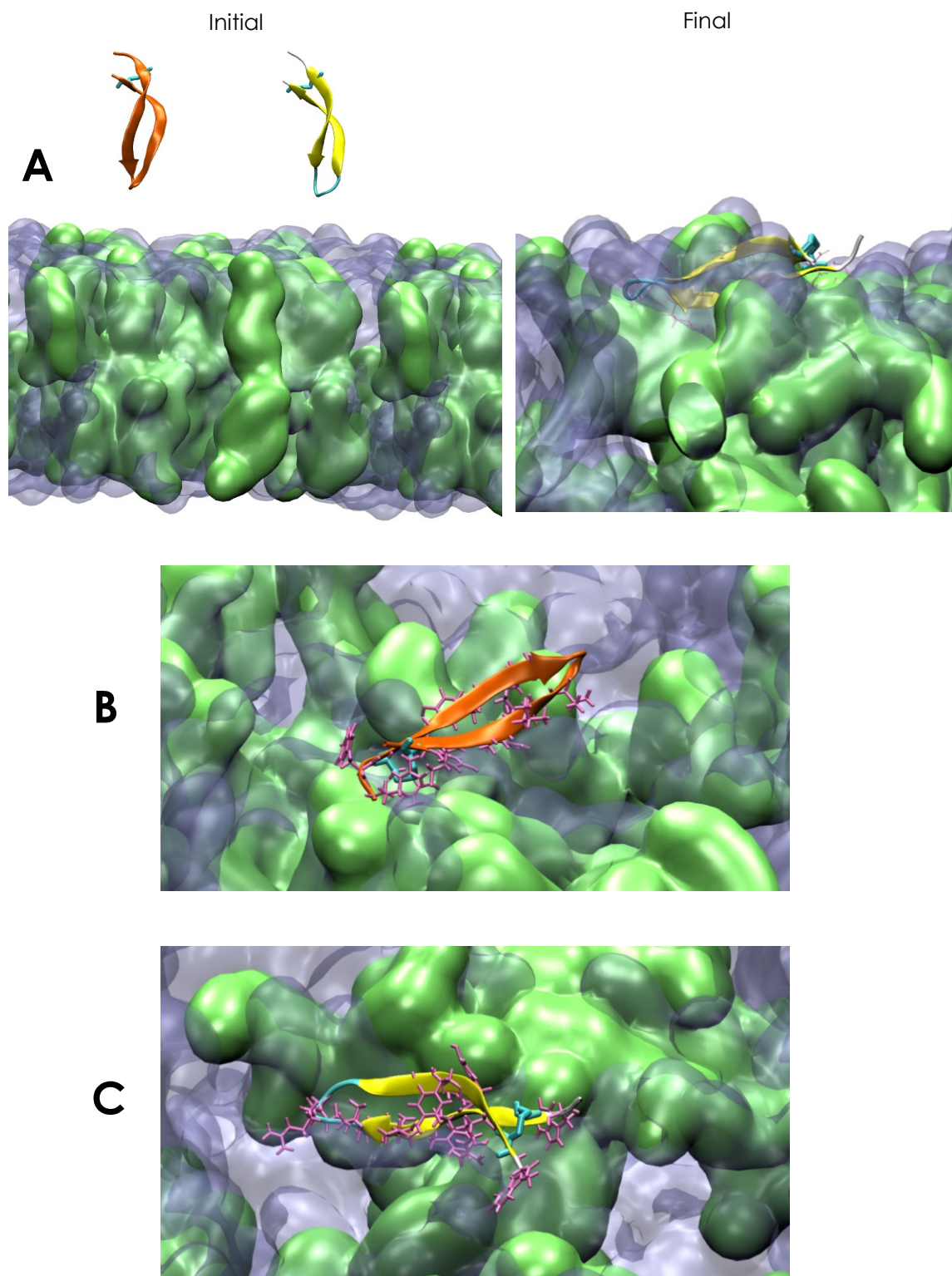


Figure 5.44. Snapshots of 3D representations of the simulation of two natural cationic AMP A1 monomers with a POPC/POPG 80:20 membrane. **A**: The initial (left) and final (right) stages of the simulation. Below **A** there are images of the top view of the final step for each monomer. The side-chain of the residues interacting with the membrane are depicted in mauve colour. In image **B** the residues involved in the interaction are: 1, 2, 3, 5, 7, 9, 13, 14, 15, 16 and 18, while in image **C** shows the residues 2, 5, 6, 7, 8, 9, 10, 11, 12, 16, 17, 19 and 21. The POPC and POPG lipids are depicted in blue and green colour, respectively.

According to the initial goal, two natural A1 monomers were used for the theoretical study in a POPC/POPG 80:20 membrane, mimicking the experimental conditions used in the SEIRA experiments. The results showed a rapid and strong interaction of A1 with the membrane in the ns scale. The snapshots from the initial and final stage of the simulation are shown in figure 4.44. The peptide conserves its antiparallel β -sheet conformation during the course of the simulation. The images of the final stage show that the peptide is partially incorporated into the lipid bilayer (top leaflet), and it prevails in an orientation perpendicular to the normal of the membrane surface. Moreover, the perturbation of the lipid bilayer structure was produced by the strong interaction of Arg residues with the negatively charged POPG lipid head groups. This interaction was accompanied by a disorder of the membrane induced by the interaction of hydrophobic side-chain groups of A1 with the acyl chains of the lipids (interacting side-chain groups are shown in mauve colour). In the course of 300 ns of simulation no dimerization was observed.

To conclude, the results of the trajectories demonstrated the stability of A1 secondary structure in solution and in presence of the POPC/POPG membrane, as well as the importance of Arg and aromatic residues for the peptide perturbation of the lipid bilayer. The important role of Arg residues was also shown by Cho and Lee (2011), where a modified peptide characterised by reduced net charge exhibited weaker interaction with the negatively charged membrane and consequently, lower antimicrobial activity [78]. The perturbation of the membrane provoked by the interaction of Arg residues with the POPG head groups and subsequent pore formation, may support a disordered toroidal pore mechanism of action due to the disorganisation of the lipids, or a carpet model as suggested by Ändra et al (2008) [63]. These mechanisms differ from the proposed toroidal pore formation by dimers of the arenicin 2 [118]. Nonetheless, this is the beginning of the investigation of A1 peptide with membranes, and the analysis of further MD simulation scenarios may afford a comprehensive understanding of the peptide behaviour.

4.3.5. Conclusions.

This work presents a study of the structure and peptide-membrane interaction of the AMP A1, combining vibrational spectroscopy and membrane model systems. The results of all the vibrational spectroscopic techniques used here, ATR-IR, FT-Raman, FT-IR transmission and SEIRA, revealed that A1 adopts a β -sheet with a turn secondary structure in solid, solution and membrane-like environments. SEIRA experiments showed that A1 interaction with the lipids is practically spontaneous, which was supported by the preliminary results from the MD simulations of the system. In this case, the incubation of A1 at different temperatures (4° C, 25° C and 37° C) showed fewer variations than expected, though the most pronounced changes in the membrane were observed at 37° C. Additionally, initial results from the potential-dependence evaluation showed

that negative potentials below -100 mV provoke irreversible perturbation of the lipid bilayer, which is significantly increased at 37° C.

The results presented here may be considered as a starting point for further investigation of A1 in membrane models to evaluate its binding process to artificial membranes and modes of action. Investigation on different peptide concentrations, ion strengths of the solution, temperatures, ions and potentials could provide more insights into A1 mechanism of action, though so far it looks like A1 induces a disorganization of the lipid bilayer supporting the carpet or disordered toroidal models.

5. Conclusions

A nanodisc system was successfully immobilised on a functionalised nanostructured Au-film for the characterisation of the slow-mutant C128S of the ChR II membrane protein. The quality of the SAMs was evaluated by EIS and SEIRA spectroscopy. The pure NTA monolayer showed the most robust results and better reproducibility, contrary to the defects in the mixed SAM with the 3MP molecule. The ChR II protein embedded in the nanodisc was bound to the NTA SAM through a His-tag linker in the MSP. Excitingly, here is shown for the first time the transition of the ChR II C128S mutant from the DA to the P390 state observed by SEIRA spectroscopy using nanodisc systems. This transition was induced by illumination of the DA sample with 468 nm (blue) light, showing changes in the amide I region at $(-)$ 1664 cm^{-1} and $(+)$ 1653 cm^{-1} assigned to the structural changes of the retinal protein. Further transitions were investigated by UV-vis and FT-IR transmission spectroscopy. In all cases, the changes observed matched the changes of the ChR II C128S mutant in absence of the nanodisc system, denoting the conservation of protein structure and function after incorporation into the membrane system. These results validate the use of nanodisc systems to study membrane proteins, even though further optimisation of the system, as well as the illumination procedure in the case of ChR II is still necessary.

Tethered bilayer lipid membrane systems have proved to be an excellent platform for the study of membrane-active AMPs. Here, two tBLM systems were described and successfully constructed onto a functionalised Au-film with a mixed SAM composed of hydrophobic WK3SH tethered molecule and hydrophilic 6MH. Both tBLMs were characterised by SEIRA and EIS. The optimum ratio of these two SAM molecules (80:20, WK3SH:6MH) provided the appropriate platform for the formation of lipid bilayer islands and a reproducible system.

The membrane interaction of the hydrophobic peptide EB and its complex formation with monovalent ion were studied by SEIRA spectroscopy using POPC tBLM systems. The results obtained here, represent a comprehensive study of EB by vibrational spectroscopy, together with exciting preliminary results of EB:ion complexes by DFT calculations. The FT-IR, SEIRA and DFT results indicated marked changes between the EB: Na^+ and EB: K^+ species, which implies the formation of complexes of different stoichiometry. These findings suggest a 1:1 and 2:1 ratio for the Na^+ and K^+ complexes, respectively, which is in conflict with previously proposed ratios for Na^+ ion [61]. Another controversial result is the suggested 2:1 ratio for the EB: Cs^+ complex, which neither matches the predictions by Ovchinnikov nor the proposed 1:1 stoichiometry by Makrlík (DFT calculations) [119]. On the other hand, the low Na^+/K^+ selectivity and ion affinity are in line with the gradient suggested in literature. Thus, the combined study presented here can be considered as a starting point for a more detailed investigation of EB and similar depsipeptides such as Beauvericin and valinomycin.

The POPC/POPG tBLM was employed to investigate the cationic AMP A1. Secondary structure analysis by means of ATR-IR, FT-Raman, FT-IR, SEIRA spectroscopy and also, preliminary results achieved by MD simulations proved the antiparallel β -sheet conformation with a turn in solid and solution, as well as in contact with the membrane system. This work aimed to offer more insight into the A1 behaviour, since the conservation of its β -sheet conformation when interacting with membranes is on current debate. The SEIRA spectroscopy results showed a perturbation of the negative charged membrane by A1 at 4° C, 25° C, and 37° C. This perturbation was increased after applying negative potentials. These changes were not reversible and appeared to be aggravated at 37° C. The MD simulation results of the peptide with a POPC/POPG membrane support the interpretation of the SEIRA measurements, providing additional atomistic information of A1 behaviour in solution and in the membrane environment. Though this is the initial stage, this work is of great relevance for a better understanding of the mode of action of this unique AMP. Future investigations will focus on a comprehensive analysis of this cationic AMP effects in contact with tBLM systems.

Outlook

This work showed the successful construction and application of membrane-mimetic systems for the study of membrane-interacting biomolecules by a spectroelectrochemical approach combining SEIRA and EIS spectroscopy. In case of the nanodisc system, there are a growing number of studies that supports the application and advances in this field applied to membrane proteins. The promising results shown here demonstrate the versatility and great potential of tBLM systems for the study of membrane-active AMPs. Improvements of conditions and a gradual increase of the complexity towards a more realistic model of cell membranes are some of the directions of future studies. Additional interest lies in further experiments concerning EB and A1, and perhaps their respective modified peptides such as the azido-modified EB for Stark effect analysis by measuring the shift of the strong azide band ($\sim 2160\text{-}2120\text{ cm}^{-1}$) to estimate complex stoichiometries; or A1 mutants to test the influence of amino acids such as Arg, Tyr, Trp or Cys that play a key role in the peptide's activity. In the case of A1, further investigation of salt gradient, temperature and potential dependence of A1 activity, as well as time and peptide concentration are some suggested experiments. In general, the extension of the study of AMPs with tBLM systems combined with the spectroelectrochemical approach and theoretical calculations to other potential targets is an attractive research field for the future.

Bibliography

- [1] Microbiology Society. (2017) MicrobiologyOnline. [Online].
<http://www.microbiologyonline.org.uk>
- [2] Manash Pratim Barkataki. (2015, September) Optogenetics. [Online].
<http://optogenetics.weebly.com>
- [3] Albert L Lehninger, David L Nelson, and Michael M Cox, *Lehninger principles of biochemistry*. New York: W.H. Freeman, 2005.
- [4] Nermina Malanovic and Karl Lohner, "Gram-positive bacterial cell envelopes: The impact on the activity of antimicrobial peptides," *Biochimica et Biophysica Acta (BBA) - Biomembranes*, vol. 1858, no. 5, pp. 915-917, May 2016, <https://doi.org/10.1016/j.bbamem.2016.03.005>.
- [5] S J Singer and Grath L Nicholson, "The Fluid Mosaic Model of the Structure of Cell Membranes," *Science*, vol. 175, no. 4023, pp. 720-731, Frebraury 1972, <https://doi.org/10.1126/science.175.4023.720>.
- [6] Jonathan D. Nickels et al., "The in vivo structure of biological membranes and evidence for lipid domains," *PLOS Biology*, pp. 1-22, May 2017, <https://doi.org/10.1371/journal.pbio.2002214>.
- [7] Paul Mueller, D O Rudin, H T Tien, and W C Wescott, "Reconstitution of cell membrane structure in vitro and its transformation into an excitable system," *Nature*, pp. 979-980, 1962.
- [8] David C Lee and Denis Chapman, "Infrared Spectroscopic Studies of Biomembranes and Model Membranes," *Bioscience Reports*, vol. 6, no. 3, pp. 235-256, 1986, Review.
- [9] Lars J. C. Jeuken et al., "Phase separation in mixed self-assembled monolayers and its effect on biomimetic membranes," *Sensors and Actuators B Chemical*, vol. 124, pp. 501-509, 2007.
- [10] Timothy H. Bayburt, Yelena V. Grinkova, and Stephen G. Sligar, "Self-Assembly of Discoidal Phospholipid Bilayer Nanoparticles with Membrane Scaffold Proteins," *NANO Letters*, vol. 2, no. 8, pp. 853-856, 2002.
- [11] Jacek Kozuch et al., "Voltage-dependent structural changes of the membrane-bound anion channel hVDAC1 probed by SEIRA and electrochemical impedance spectroscopy," *Physical Chemistry Chemical Physics*, vol. 16, no. 20, pp. 9546-9555, 2014.

- [12] Kenichi Ataka, Sven Timo Stripp, and Joachim Heberle, "Surface-enhanced infrared absorption spectroscopy (SEIRAS) to probe monolayers of membrane proteins," *Biochimica et Biophysica Acta*, vol. 1828, pp. 2283–2293, June 2013.
- [13] Sophie A Weiss, Richard J Bushby, Stephen D Evans, and Lars J. C. Jeuken, "A study of cytochrome bo3 in a tethered bilayer lipid membrane," *Biochimica et Biophysica Acta (BBA) - Bioenergetics*, vol. 1797, no. 12, pp. 1917–1923, December 2010, <https://doi.org/10.1016/j.bbabi.2010.01.012>.
- [14] Ekaterina Zaitseva, Marcia Saavedra, Sourabh Banerjee, Thomas P Sakmar, and Reiner Vogel, "SEIRA spectroscopy on a membrane receptor monolayer using lipoprotein particles as carriers.," *Biophysical Journal*, vol. 99, no. 7, pp. 2327–2335, October 2010, doi: 10.1016/j.bpj.2010.06.054.
- [15] Vera Jansen et al., "Controlling fertilization and cAMP signaling in sperm by optogenetics," *e-Life*, vol. 4:e05161, no., pp. 1–15, January 2015, DOI: 10.7554/eLife.05161.
- [16] Curtis W. Meuse, Gediminas Niaura, Mary L. Lew, and Anne L. Plant, "Assessing the Molecular Structure of Alkanethiol Monolayers in Hybrid Bilayer Membranes with Vibrational Spectroscopies," *Langmuir*, vol. 14, no. 7, pp. 1604–1611, February 1998, DOI: 10.1021/la9700679.
- [17] Diego Milla et al., "Characterization of hybrid bilayer membranes on silver electrodes as biocompatible SERS substrates to study membrane–protein interactions," *Colloids and Surfaces B: Biointerfaces*, vol. 81, no. 1, pp. 212–216, July 2010, <https://doi.org/10.1016/j.colsurfb.2010.07.010>.
- [18] Joel H. Collier and Phillip B. Messersmith, "Phospholipid strategies in biomineralization and biomaterials research," *Annu. Rev. Mater. Res.*, vol. 31, pp. 237–63, 2001.
- [19] Lukas K. Tamm and Suren A. Tatulian, "Infrared spectroscopy of proteins and peptides in lipid bilayers," *Quaternary Reviews of Biophysics*, vol. 30, no. 4, pp. 365–429, 1997.
- [20] M. Cortijo, A. Alonso, J. C. Gómez-Fernández, and D. Chapman, "Intrinsic protein-lipid interactions: Infrared spectroscopic studies of gramicidin A, bacteriorhodopsin and Ca²⁺-ATPase in biomembranes and reconstituted systems," *Journal of Molecular Biology*, vol. 157, no. 4, pp. 597–618, June 1982, [https://doi.org/10.1016/0022-2836\(82\)90501-0](https://doi.org/10.1016/0022-2836(82)90501-0).
- [21] Jacek Kozuch, *Structure-Function Relationships of Membrane Proteins - Spectroelectrochemical Investigation of Artificial Membranes*. Berlin, Germany: Technischen Universität Berlin, 2013.

- [22] Ilia G. Denisov and Stephen G. Sligar, "Nanodiscs in Membrane Biochemistry and Biophysics," *Chemical Reviews*, vol. 117, p. 4669–4713, February 2017, DOI: 10.1021/acs.chemrev.6b00690.
- [23] Andrew J. Leitz, Timothy H. Bayburt, Alexander N. Barnakov, Barry A. Springer, and Stephen G. Sligar, "Functional reconstitution of β 2-adrenergic receptors utilizing self-assembling Nanodisc technology," *BioTechniques*, vol. 40, no. 5, pp. 601–612, May 2006, DOI: 10.2144/000112169.
- [24] Zeting Zhang et al., "Ca²⁺ modulating α -synuclein membrane transient interactions revealed by solution NMR spectroscopy," *Biochimica et Biophysica Acta (BBA) - Biomembranes*, vol. 1838, no. 3, pp. 853–858, March 2014, <https://doi.org/10.1016/j.bbamem.2013.11.016>.
- [25] Chanjuan Wan et al., "Insights into the molecular recognition of the granuphilin C2A domain with PI(4,5)P₂," *Chemistry and Physics of Lipids*, vol. 186, pp. 61–67, February 2015, <https://doi.org/10.1016/j.chemphyslip.2015.01.003>.
- [26] Timothy H. Bayburt and Stephen G. Sligar, "Membrane Protein Assembly into Nanodiscs," *FEBS Letters*, vol. 584, no. 9, pp. 1721–1727, May 2010.
- [27] Nicolas Bocquet et al., "Real-time monitoring of binding events on a thermostabilized human A_{2A} receptor embedded in a lipid bilayer by surface plasmon resonance," *Biochimica et Biophysica Acta (BBA) - Biomembranes*, vol. 1848, no. 5, pp. 1224–1233, May 2015, <https://doi.org/10.1016/j.bbamem.2015.02.014>.
- [28] A. Das, J. Zhao, G. C. Schatz, S. G. Sligar, and R. P. Van Duyne, "Screening of type I and II drug binding to human cytochrome P450-3A4 in nanodiscs by localized surface plasmon resonance spectroscopy," *Analytical chemistry*, vol. 81, no. 10, pp. 3754–3759, 2009, DOI: 10.1021/ac802612z.
- [29] Swantje Wiebalck et al., "Monitoring the Transmembrane Proton Gradient Generated by Cytochrome bo 3 in Tethered Bilayer Lipid Membranes Using SEIRA Spectroscopy," *The Journal of Physical Chemistry B*, vol. 120, no. 9, pp. 2249–2256, 2016.
- [30] Jacqueline Knobloch, Daniel K. Suhendro, Julius L. Zieleniecki, Joseph G. Shapter, and Ingo Köper, "Membrane–drug interactions studied using model membrane systems," *Saudi Journal of Biological Sciences*, vol. 22, no. 6, pp. 714–718, November 2015, <https://doi.org/10.1016/j.sjbs.2015.03.007>.

- [31] Ali Adem Bahar and Dacheng Ren, "Antimicrobial Peptides," *Pharmaceuticals*, vol. 6, pp. 1543-1575, 2013, doi:10.3390/ph6121543.
- [32] Mariana Ruíz Villareal. (2007, -) Membrane transport protein. [Online]. https://en.wikipedia.org/wiki/membrane_transport_protein
- [33] Víctor A. Lórenz-Fonfría et al., "Transient protonation changes in channelrhodopsin-2 and their relevance to channel gating," *PNAS*, vol. 110, no. 14, pp. E1273–E1281, March 2013, DOI: 10.1073/pnas.1219502110.
- [34] Eglof Ritter, Patrick Piwowarski, Peter Hegemann, and Franz J. Bartl, "Channelrhodopsin C128T Mutant Light-dark Adaptation of," *The Journal of Biological Biophysics*, vol. 288, no. 15, pp. 10451–10458, 2013, DOI: 10.1074/jbc.M112.446427.
- [35] Zoe Cournia et al., "Membrane Protein Structure, Function and Dynamics: A Perspective from Experiments and Theory," *The Journal of Membrane Biology*, vol. 248, no. 4, pp. 611–640, 2015, doi:10.1007/s00232-015-9802-0.
- [36] Samuel Krimm and Jagdeesh Bandekar, "VIBRATIONAL SPECTROSCOPY AND CONFORMATION OF PEPTIDES. POLYPEPTIDES. AND PROTEINS," *ADVANCES IN PROTEIN CHEMISTRY*, vol. 38, pp. 181-364, 1986.
- [37] Friedrich Siebert and Peter Hildebrandt, *Vibrational Spectroscopy in Life Science.:* Wiley-VCH Verlag GmbH & Co. KGaA, 2008.
- [38] S. Yu. Venyaminov and N. N. Kalnin, "Quantitative IR spectrophotometry of peptide compounds in water (H₂O) solution. I. Spectral parameters of amino acid residue absorption bands," *Biopolymers*, vol. 30, pp. 1243-1257, 1990.
- [39] Andreas Barth, "Infrared spectroscopy of proteins," *Biochimica et Biophysica Acta*, vol. 1767, pp. 1073–1101, 2007, doi:10.1016/j.bbabbio.2007.06.004.
- [40] Víctor A. Lórenz-Fonfría and Joachim Heberle, "Channelrhodopsin unchained: Structure and mechanism of a light-gated cation channel," *Biochimica et Biophysica Acta (BBA) - Bioenergetics*, vol. 1837, no. 5, pp. 626-642, 2014, <https://doi.org/10.1016/j.bbabbio.2013.10.014>.
- [41] Christian Bamann, Ronnie Gueta, Sonja Kleinlogel, Georg Nagel, and Enrst Bamberg, "Structural guidance of the photocycle of channelrhodopsin-2 by an interhelical hydrogen bond," *biochemistry*, vol. 49, no. 2, pp. 267-278, 2010.
- [42] Sara Bruun et al., "Light–Dark Adaptation of Channelrhodopsin Involves Photoconversion between the all-trans and 13-cis Retinal Isomers," *Biochemistry*, vol. 54, pp. 5389-5400, 2015, DOI: 10.1021/acs.biochem.5b00597.

- [43] Georg Nagel et al., "Channelrhodopsin-2, a directly light-gated cation-selective membrane channel," *PNAS*, vol. 100, no. 24, pp. 13940–13945, 2003.
- [44] Sara Bruun et al., "The chromophore structure of the long-lived intermediate of the C128T channelrhodopsin-2 variant," *FEBS Letters*, vol. 585, pp. 3998–4001, 2011, doi:10.1016/j.febslet.2011.11.007.
- [45] Peter Hegemann and Georg Nagel, "From channelrhodopsins to optogenetics," *EMBO Molecular Medicine*, vol. 5, no. 2, pp. 173–176, February 2013, DOI: 10.1002/emmm.201202387.
- [46] Andre Berndt et al., "Structural foundations of optogenetics: Determinants of channelrhodopsin ion selectivity," *PNAS*, vol. 113, no. 4, pp. 822–829, November 2016, doi: 10.1073/pnas.1523341113.
- [47] Katja Stehfest, Eglof Ritter, André Berndt, Franz Bartl, and Peter Hegemann, "The Branched Photocycle of the Slow-Cycling Channelrhodopsin-2 Mutant C128T," *The Journal of Molecular Biology*, vol. 398, pp. 690–702, 2010, doi:10.1016/j.jmb.2010.03.031.
- [48] André Berndt, Ofer Yizhar, Lisa A. Gunaydin, Peter Hegemann, and Karl Deisseroth, "Bi-stable neural state switches," *nature neuroscience*, vol. 12, no. 2, pp. 229–234, 2009, doi:10.1038/nn.2247.
- [49] J. M. Ageitos, A. Sánchez-Pérez, P. Calo-Mata, and T. G. Villa, "Antimicrobial peptides (AMPs): Ancient compounds that represent novel weapons in the fight against bacteria," *Biochemical Pharmacology*, 2016, <http://dx.doi.org/10.1016/j.bcp.2016.09.018>.
- [50] Rollin D. Hotchkiss and René J. Dubos, "FRACTIONATION OF THE BACTERICIDAL AGENT FROM CULTURES OF A SOIL BACILLUS," *The Journal of Biological Chemistry*, vol. 132, pp. 791–792, 1940.
- [51] James G. Hirsch, "PHAGOCYTIN: A BACTERICIDAL SUBSTANCE FROM POLYMORPHONUCLEAR LEUCOCYTES," *The Journal of Experimental Medicine*, vol. 103, no. 5, pp. 589–611, 1956, DOI: 10.1084/jem.103.5.589.
- [52] René J. Dubos, "Studies on a bactericidal agent extracted from a soil bacillus," *The Journal of Experimental Medicine*, vol. 70, no. 1, pp. 1–10, 1939.
- [53] M. Stauss-Grabo, S. Atiye, T. Le, and M. Kretschmar, "Decade-long use of the antimicrobial peptide combination tyrothricin does not pose a major risk of acquired resistance with gram-positive bacteria and *Candida* spp.," *Pharmazie*, vol. 69, no. 11, pp. 838–841, November 2014, <http://dx.doi.org/10.1691/ph.2014.4686>.

- [54] David A. Phoenix, Sarah R. Dennison, and Frederick Harris, *Antimicrobial Peptides*, 1st ed.: Wiley-VCH Verlag GmbH & Co. KGaA, 2013.
- [55] J. Bradshaw, "Cationic antimicrobial peptides : issues for potential clinical use.," *BioDrugs Journal*, vol. 17, no. 4, pp. 233-240, 2013.
- [56] Kelly L. Brown and Robert E. W. Hancock, "Cationic host defense (antimicrobial) peptides," *Current Opinion in Immunology*, vol. 18, no. 1, pp. 24-30, 2006, <https://doi.org/10.1016/j.coi.2005.11.004>.
- [57] Xiaowei Zhao, Hongyu Wu, Hairong Lu, Guodong Li, and Qingshan Huang, "LAMP: A Database Linking Antimicrobial Peptides," *PLOS one*, vol. 8, no. 6, pp. e66557-e66557, 2013, <https://doi.org/10.1371/journal.pone.0066557>.
- [58] Guozhang Zou et al., "Toward understanding the cationicity of defensins. Arg and Lys versus their noncoded analogs," *The Journal of Biological Chemistry*, vol. 282, no. 27, pp. 19653–19665, 2007, DOI: 10.1074/jbc.M611003200.
- [59] Annett Rozek, Carol L. Friedrich, and Robert E. W. Hancock, "Structure of the Bovine Antimicrobial Peptide Indolicidin Bound to Dodecylphosphocholine and Sodium Dodecyl Sulfate Micelles," *Biochemistry*, vol. 39, no. 51, pp. 15765–15774, 2000, DOI: 10.1021/bi000714m.
- [60] Berton C. Pressman, "Biological applications of ionophores," *Annual Review of Biochemistry*, vol. 45, pp. 501-530, 1976, <https://doi.org/10.1146/annurev.bi.45.070176.002441>.
- [61] Yu A. Ovchinnikov et al., "The enniatin ionophores. Conformation and ion binding properties," *Int. J. Peptide Protein Res.*, vol. 6, pp. 465-498, 1974.
- [62] Leonard T. Nguyen, Evan F. Haney, and Hans J. Vogel, "The expanding scope of antimicrobial peptide structures and their modes of action," *Trends in Biotechnology*, vol. 29, no. 9, pp. 464-472, 2011, <https://doi.org/10.1016/j.tibtech.2011.05.001>.
- [63] Jörg Andrä et al., "Structure and mode of action of the antimicrobial peptide arenicin," *Biochemistry Journal*, vol. 410, pp. 113-122, 2008, doi:10.1042/BJ20071051.
- [64] Tatiana V. Ovchinnikova et al., "Purification and primary structure of two isoforms of arenicin, a novel antimicrobial peptide from marine polychaeta Arenicola marina," *FEBS Letters*, vol. 577, pp. 209-214, 2004, doi:10.1016/j.febslet.2004.10.012.
- [65] Brandon Findlay, George G. Zanel, and Frank Schweizer, "Cationic Amphiphiles, a New Generation of Antimicrobials Inspired by the Natural Antimicrobial Peptide Scaffold," *Antimicrobial Agents and Chemotherapy*, vol. 45, no. 10, pp. 4049-4058, 2010, doi: 10.1128/AAC.00530-10.

- [66] Lennart Richter et al., "Engineering of *Aspergillus niger* for the production of secondary metabolites," *Fungal Biology and Biotechnology*, vol. 1, no. 4, pp. 1-13, 2014.
- [67] E. Gaumann and O. Jaag, "Die physiologischen Grundlagen des parasitogenen Welkens," *Ber. Schweiz. Bot. Ges.*, vol. 57, pp. 3-34, 1947.
- [68] Ralene R. Mitschler, Ruth Welti, and Steve J. Opton, "A Comparative Study of Lipid Compositions of *Cryptosporidium parvum* (Apicomplexa) and Madin-Darby Bovine Kidney Cells," *The Journal of Eukaryotic Microbiology*, vol. 41, no. 1, pp. 8-12, 1994, DOI: 10.1111/j.1550-7408.1994.tb05927.x.
- [69] Michèle German-Fattal, "Fusafungine, an Antimicrobial with Anti-Inflammatory Properties in Respiratory Tract Infections," *Clinical Drug Investigation*, vol. 21, no. 9, pp. 653-670, 2001.
- [70] Arlene A. Sy-Cordero, Cedric J. Pearce, and Nicholas H. Oberlies, "Revisiting the enniatins: a review of their isolation, biosynthesis, structure determination, and biological activities," *J Antibiot*, vol. 65, no. 11, pp. 541-549, 2012, doi:10.1038/ja.2012.71.
- [71] G. Meca et al., "Antifungal effects of the bioactive compounds enniatins A, A1, B, B1," *Toxicon*, vol. 56, no. 3, pp. 480-485, 2010, <https://doi.org/10.1016/j.toxicon.2010.04.013>.
- [72] Rita Dornetshuber et al., "Enniatin Exerts p53-Dependent Cytostatic and p53-Independent Cytotoxic Activities against Human Cancer Cells," *Chem. Res. Toxicol.*, vol. 20, pp. 465-473, 2007.
- [73] Wim Wätjen et al., "Enniatins A1, B and B1 from an endophytic strain of *Fusarium tricinctum* induce apoptotic cell death in H4IIE hepatoma cells accompanied by inhibition of ERK phosphorylation," *Molecular nutrition & Food research*, vol. 53, no. 4, pp. 431-440, 2009, DOI: 10.1002/mnfr.200700428.
- [74] K. A. Mereish, R. Solow, D. L. Bunner, and A. B. Fajer, "Interaction of cyclic peptides and depsipeptides with calmodulin," *Pept. Res.*, vol. 3, no. 5, p. 233.237, 1990.
- [75] Claudia Behm, Gisela H. Degen, and Wolfram Föllmann, "The *Fusarium* toxin enniatin B exerts no genotoxic activity, but pronounced cytotoxicity in vitro," *Molecular Nutrition & Food research*, vol. 53, no. 4, pp. 423-430, 2009, DOI: 10.1002/mnfr.200800183.
- [76] Majidreza Kamyar, Pakiza Rawnduzi, Christian R. Studenik, Katerina Kouri, and Rosa Lemmens-Gruber, "Investigation of the electrophysiological properties of enniatins," *Archives of Biochemistry and Biophysics*, vol. 429, no. 2, pp. 215-223, 2004, <https://doi.org/10.1016/j.abb.2004.06.013>.

- [77] N. E. Zhukhlistova, "X-ray Crystal Structure of the Complex of Enniatin B with KNCS," *Crystallography Reports*, vol. 47, no. 3, pp. 478-487, 2002.
- [78] Jaeyong Cho and Dong Gun Lee, "The characteristic region of arenicin-1 involved with a bacterial membrane targeting mechanism," *Biochemical and Biophysical Research Communications*, vol. 405, pp. 422-427, 2011.
- [79] Oksana G. Tarvkova and Gerald Brezesinski, "Adsorption of the antimicrobial peptide arenicin and its linear derivative to model membranes – A maximum insertion pressure study," *Chemistry and Physics of Lipids*, vol. 167-168, pp. 43-50, 2013.
- [80] Cana Park and Dong Gun Lee, "Fungicidal effect of antimicrobial peptide arenicin-1," *Biochimica et Biophysica Acta*, vol. 1788, pp. 1790-1796, 2009.
- [81] Jaeyong Cho and Dong Gun Lee, "The antimicrobial peptide arenicin-1 promotes generation of reactive oxygen species and induction of apoptosis," *Biochimica et Biophysica Acta*, vol. 1810, pp. 1246-1251, 2011.
- [82] Radek Macháň, Martin Hof, Tatsiana Chernovets, Maxim N. Zhmak, and Tatiana V. Ovchinnikova, "Formation of arenicin-1 microdomains in bilayers and their specific lipid interaction revealed by Z-scan FCS," *Anal. Bioanal. chem.*, vol. 399, pp. 3547-3554, 2011.
- [83] Kunichi Ataka and Joachim Heberle, "Electrochemically Induced Surface-Enhanced Infrared Difference Absorption (SEIDA) Spectroscopy of a Protein Monolayer," *Journal of the American Chemical Society*, vol. 125, no. 13, pp. 4986-4987, 2003, DOI: 10.1021/ja0346532.
- [84] Erik Goormaghtigh, Vincent Raussens, and Jean-Marie Ruysschaert, "Attenuated total reflection infrared spectroscopy of proteins and lipids in biological membranes," *Biochimica et Biophysica Acta (BBA) - Reviews on Biomembranes*, vol. 1422, no. 2, pp. 105-185, 1999, [https://doi.org/10.1016/S0304-4157\(99\)00004-0](https://doi.org/10.1016/S0304-4157(99)00004-0).
- [85] A. Hartstein, J. R. Kirtley, and J. C. Tsang, "Enhancement of the Infrared Absorption from Molecular Monolayers with Thin Metal Overlayers," *Physical Reviews Letters*, vol. 45, no. 3, pp. 201-204, 1980.
- [86] Masatoshi Osawa, "Surface-enhanced infrared absorption spectroscopy," pp. 1-15, 2002.
- [87] Kenichi Ataka et al., "Oriented Attachment and Membrane Reconstitution of His-Tagged Cytochrome c Oxidase to a Gold Electrode: In Situ Monitoring by Surface-Enhanced Infrared Absorption Spectroscopy," *J. Am. Chem. Soc.*, vol. 126, no. 49, pp. 16199–16206, July 2004, DOI: 10.1021/ja045951h.

- [88] Nattawadee Wisitruangsakul et al., "Redox-linked protein dynamics of cytochrome c probed by time-resolved surface enhanced infrared absorption spectroscopy," *Phys. chem. chem. phys.*, vol. 10, no. 34, pp. 5276-5286, 2008.
- [89] Diego Millo, Peter Hildebrandt, Maria-Eirini Pandelia, Wolfgang Lubitz, and Ingo Zebger, "SEIRA Spectroscopy of the Electrochemical Activation of an Immobilized [NiFe] Hydrogenase under Turnover and Non-Turnover Conditions," *Angewandte Chemie-International Edition*, vol. 50, no. 11, pp. 2632-2634, 2011.
- [90] Masatoshi Osawa, Kenichi Ataka, Katsumasa Yoshii, and Yuji Nishikawa, "Surface-Enhanced Infrared Spectroscopy: The Origin of the Absorption Enhancement and Band Selection Rule in the Infrared Spectra of Molecules Adsorbed on Fine Metal Particles," *Applied Spectroscopy*, vol. 47, no. 9, pp. 1497-1502, 1993.
- [91] F. Lisdat and D. Schäfer, "The use of electrochemical impedance spectroscopy for biosensing," *Anal Bioanal Chem.*, vol. 391, no. 5, pp. 1555-1567, 2008.
- [92] James K. R. Kendall et al., "Effect of the Structure of Cholesterol-Based Tethered Bilayer Lipid Membranes on Ionophore Activity," *ChemPhysChem*, vol. 11, no. 10, pp. 2191-2198, May 2010, DOI: 10.1002/cphc.200900917.
- [93] V. F. Lvovich, *Impedance Spectroscopy: Applications to Electrochemical and Dielectric Phenomena.*: John Wiley & Sons, Inc., 2012.
- [94] Evgenij Barsoukov and J. Ross Macdonald, *Impedance Spectroscopy: Theory, Experiment, and Applications*, 2nd ed., 2005.
- [95] Gintaras Valincius, Tadas Meškauskas, and Feliksas Ivanauskas, "Electrochemical Impedance Spectroscopy of Tethered Bilayer Membranes," *Langmuir*, vol. 28, no. 1, pp. 977-990, 2012.
- [96] P. M. Gomadam and J. W. Weidner, "Analysis of electrochemical impedance spectroscopy in proton exchange membrane fuel cells," *International Journal of Energy research*, vol. 29, no. 12, pp. 1133-1151, 2005.
- [97] B. A. Boukamp, "A nonlinear least squares fit for analysis of immittance data of electrochemical systems," *Solid-state ionics*, vol. 20, pp. 31-40, 1986.
- [98] S. Ohki, "Properties of Lipid Bilayer Membranes. Membrane Thickness," *Journal of Theoretical Biology*, vol. 26, pp. 277-287, 1970.
- [99] H. G. Coster and J. R. Smith, "The molecular organisation of bimolecular lipid membranes. A study of the low frequency Maxwell-Wagner impedance dispersion," *Biochim Biophys Acta.*, vol. 373, no. 2, pp. 151-64, 1974.

- [100] V. D. Jovic and B. M. Jovic, "EIS and differential capacitance measurements onto single crystal faces in different solutions: Part I: Ag(111) in 0.01 M NaCl," *Journal of Electroanalytical Chemistry*, vol. 541, pp. 1-11, 2003.
- [101] Hiroto Miyake, Shen Ye, and Masatoshi Osawa, "Electroless deposition of gold thin films on silicon for surface-enhanced infrared spectroelectrochemistry," *Electrochemistry Communications*, vol. 4, no. 12, pp. 973-977, 2002, [https://doi.org/10.1016/S1388-2481\(02\)00510-6](https://doi.org/10.1016/S1388-2481(02)00510-6).
- [102] S. Trasatti and O. A. Petrii, "Real surface area measurements in electrochemistry," *Pure Appl. Chem.*, vol. 63, no. 5, pp. 711-734, 1991, <http://dx.doi.org/10.1351/pac199163050711>.
- [103] Francisco Javier Velázquez Escobar, *Vibrational spectroscopy of phytochromes and phytochrome-related photoreceptors*. Berlin, Germany: Technischen Universität Berlin, 2015.
- [104] Amit Vaish et al., "A generalized strategy for immobilizing uniformly oriented membrane proteins at solid interfaces," *Chemical Communications*, vol. 49, no. 26, pp. 2685-2687, 2013.
- [105] Marcel G. Friedrich et al., "Activity of Membrane Proteins Immobilized on Surfaces as a Function of Packing Density," *The Journal of physical chemistry B*, vol. 112, no. 10, pp. 3193-3201, 2008.
- [106] Emma M. Ericsson et al., "Site-Specific and Covalent Attachment of His-Tagged Proteins by Chelation Assisted Photoimmobilization: A Strategy for Microarraying of Protein Ligands," *Langmuir*, vol. 29, no. 37, pp. 11687-11694, 2013.
- [107] Jonas Schartner et al., "Universal Method for Protein Immobilization on Chemically Functionalized Germanium Investigated by ATR-FTIR Difference Spectroscopy," *Journal of the American Chemical Society*, vol. 135, p. 4079-4087, 2013.
- [108] Paul Mueller and Donald O. Rudin, "Development of K⁺ - Na⁺ discrimination in experimental bimolecular lipid membrane by macrocyclic antibiotic," *Biochemical and Biophysical research communications*, vol. 26, no. 4, pp. 398-404, 1967.
- [109] M. M. Shemyakin et al., "Cyclodepsipeptides as Chemical Tools for Studying Ionic Transport Through Membranes," *The Journal of Membrane Biology*, vol. 1, pp. 402-430, 1969.
- [110] Jan Palacky, Peter Mojzes, and Jirí Bork, "SVD-based method for intensity normalization, background correction and solvent subtraction in Raman spectroscopy exploiting the properties of water stretching vibrations," *The Journal of Raman Spectroscopy*, vol. 42, no. 7, pp. 1528-1539, 2011.

- [111] Jan Kubelka and Timothy A. Keiderling, "Differentiation of β -Sheet-Forming Structures: Ab Initio-Based Simulations of IR Absorption and Vibrational CD for Model Peptide and Protein beta-Sheets," *Journal of the American Chemical Society*, vol. 123, pp. 12048-12058, 2001.
- [112] Yu. N. Chirgadze, O. V. Fedorov, And N. P. Trushina, "Estimation of Amino Acid Residue Side-Chain Absorption in the Infrared Spectra of Protein Solutions in Heavy Water," *Biopolymers*, vol. 14, pp. 679-694, 1975.
- [113] Nurettin Demirdöven et al., "Two-Dimensional Infrared Spectroscopy of Antiparallel beta-Sheet Secondary Structure," *Journal of the American Chemical Society*, vol. 126, pp. 7981-7990, 2004.
- [114] Yong Xie, Dongmao Zhang, Gotam K. Jarori, V. Jo Davisson, and Dor Ben-Amotz, "The Raman detection of peptide tyrosine phosphorylation," *Analytical Biochemistry*, vol. 332, pp. 116-121, 2004.
- [115] A. E. Aliaga et al., "Surface-enhanced Raman scattering study of L-tryptophan," *Journal of Raman Spectroscopy*, vol. 40, pp. 164-169, 2009.
- [116] Guangyong Zhu, Xian Zhu, Qi Fan, and Xueliang Wan, "Raman spectra of amino acids and their aqueous solutions," *Spectrochimica Acta Part A: Molecular and Biomolecular Spectroscopy*, vol. 78, pp. 1187-1195, 2011.
- [117] Evgeniy S. Salnikov et al., "Structure and Alignment of the Membrane-Associated Antimicrobial Peptide Arenicin by Oriented Solid-State NMR Spectroscopy," *Biochemistry*, vol. 50, pp. 3784-3795, 2011.
- [118] Zakhar O. Shenkarev et al., "Molecular Mechanism of Action of β -Hairpin Antimicrobial Peptide Arenicin: Oligomeric Structure in Dodecylphosphocholine Micelles and Pore Formation in Planar Lipid Bilayers," *Biochemistry*, vol. 50, no. 28, pp. 6255-6265, 2011.
- [119] Emanuel Makrlík, Stanislav Böhm, Petr Vanura, and Ivan Raich, "Extraction and DFT study on interaction of the cesium cation with enniatin B," *Journal of Molecular Structure*, vol. 1076, pp. 564-567, 2014.

Acknowledgements

Once a wiseman told me that all the experiences from my past will prepare me to live in the present. Throughout all these experiences, what has encouraged me to grow and keep walking were the people I encountered along the way. Therefore, I would like to thank to each and all of you for forming part of my life.

I would like to express my profound gratitude to Prof. Peter Hildebrandt, for the great opportunity you have given me. I am forever grateful for your support, encouragement and guidance during these years, not only in professional but also in personal matters.

I would like to thank to the School of Analytical Science Adlershof (SALSA) for the founding of my studies, as well as for the international environment, training and get-together evenings. It was a valued experience to form part of such a great school.

Special thanks to Dr. Kozuch, for introducing me to the spectroscopic world and for your contagious enthusiasm for science; and to Dr. Velázquez Escobar for the push when it was needed, the self-value (common sense) reminders, as well as for the scientific support and critical point of view.

Big thanks to my personal cheerleaders Alejandra De Miguel and Enrico Forbrig for your unconditional support, the uncountable moments of laughter and unforgettable moments during these years. Many stories shared and many more to come. The conferences will miss us!

I thank to María Fernández, Dr. Kielb and Johannes Salewski for the never-ending talks, 'coffee'-breaks, and the laughter together.

I would also like to show my appreciation to all the members of the Physical Chemistry / Biophysical Chemistry and Biomolecular Modelling teams that enriched the day-by-day work with smiles and good vibes.

Gracias a mi mejor amiga Luky, por tu Amistad incondicional y por recordarme que la vida es mucho más que trabajo y responsabilidades. Mil gracias por estar ahí siempre sin importar las distancias. Tus abrazos y sonrisa están siempre conmigo.

Moltes gracies a tu Arnau, per mantenir contacte després d'aquests anys, per inspirarme i demostrar que mai es tard per fer el que un vol. Ara et toca a tu!

I also want to thank to Anja, Alma, Nikolaj and Frederik for the universal revelations and the never boring life together no matter where.

My deepest and special thanks to Rasmus for showing me possibilities in this crazy world we live in. Thank you for the good food we share, for holding my hand when I felt down and showing me light when I could not see. More importantly, thanks for the loving, peaceful, kind and wonderful person you are. I am happy to walk this life by your side.

Gracias a mi Bernusqui, estos años no hubiesen sido lo mismo sin vos. Gracias por los largos paseos, por elegirme a mí para compartir tu vida y por enseñarme sobre el perdón. Estarás por siempre en mi corazón.

Y un gracias monumental al tesoro más valioso que el universo me ha concedido, mi familia. El amor, esfuerzo y sacrificios que mis padres han hecho para darles a sus hijos un futuro mejor, no tiene medida. Los valores con que nos criaron nos han hecho las increíbles personas que somos hoy. Gracias mamá y papá. Por supuesto, mil gracias a mi 'sis' y a mi 'bro' por la hermosa relación que tenemos y por las batallas que combatimos juntos, estoy muy orgullosa de nosotros. Gracias también a mis abuelos y familiares. Se extrañan los domingos en familia, pero se que vuestro amor está siempre conmigo. Y un gracias especial a vos abu, se que donde sea que estés ahora cuidas de mí. Los amo familia.

Appendix

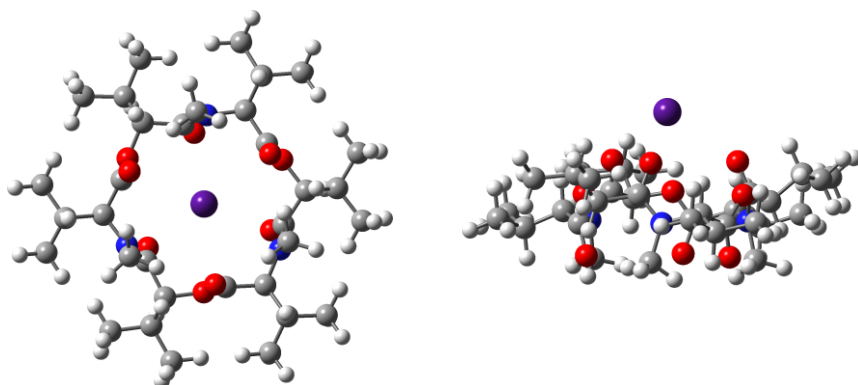


Figure A.1. Images of the top and side view of the EB structures obtained from the DFT calculation of the 1:1 complex with Cs^+ ion, also called "open-faced-sandwich". Oxygen atoms are in red, nitrogen in blue, carbon in grey, hydrogen in white, and metal ion in purple.

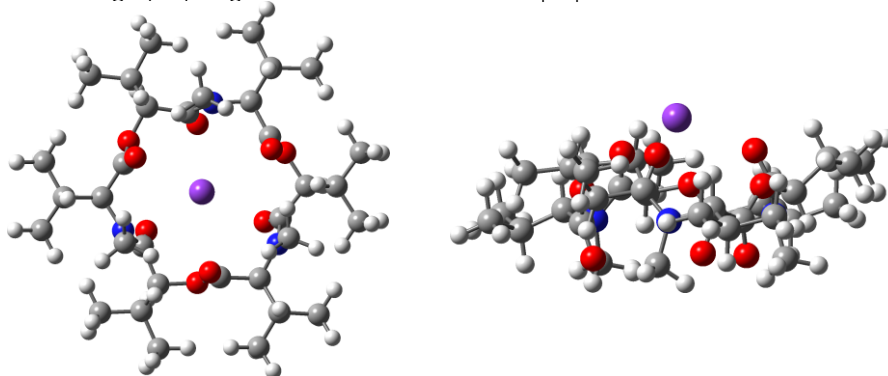


Figure A.2. Images of the top and side view of the EB structures obtained from the DFT calculation of the 1:1 complex with K^+ ion, also called "open-faced-sandwich". Oxygen atoms are in red, nitrogen in blue, carbon in grey, hydrogen in white, and metal ion in purple.

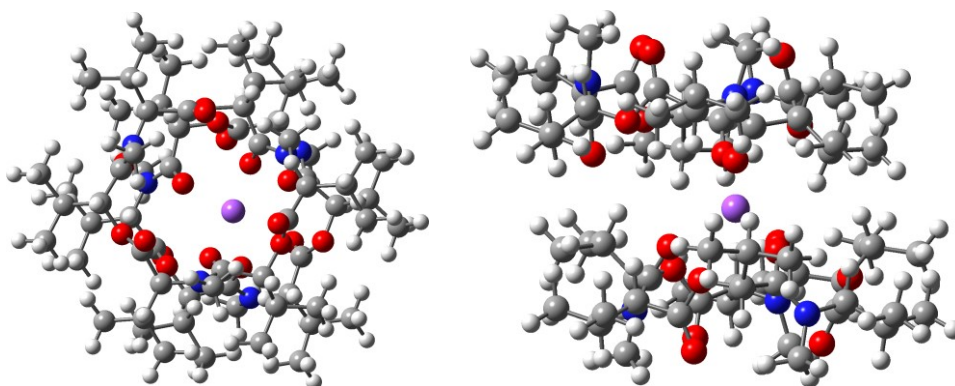


Figure A.3. Images of the top and side view of the EB structures obtained from the DFT calculation of the 2:1 complex with Na^+ ion. Oxygen atoms are in red, nitrogen in blue, carbon in grey, hydrogen in white, and metal ion in purple.

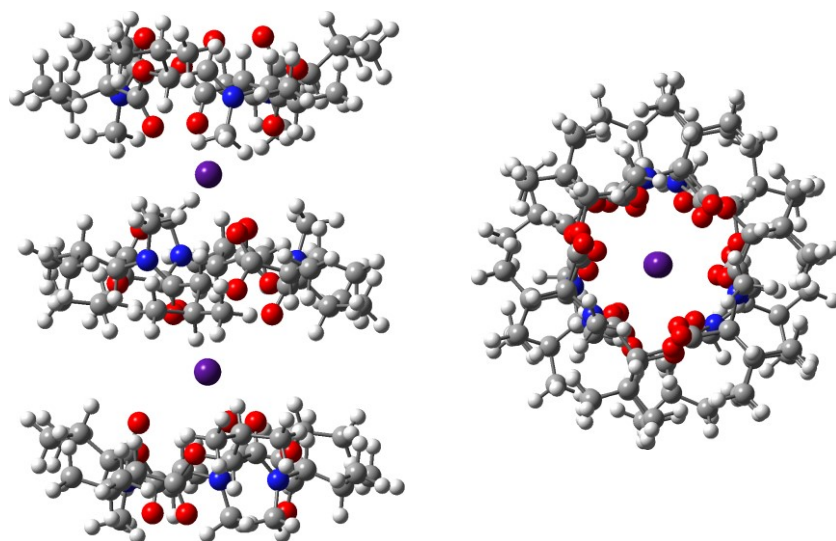


Figure A.4. Images of the top and side view of the EB structures obtained from the DFT calculation of the 3:2-AAEA complex with Cs^+ ion. Oxygen atoms are in red, nitrogen in blue, carbon in grey, hydrogen in white, and metal ion in purple.

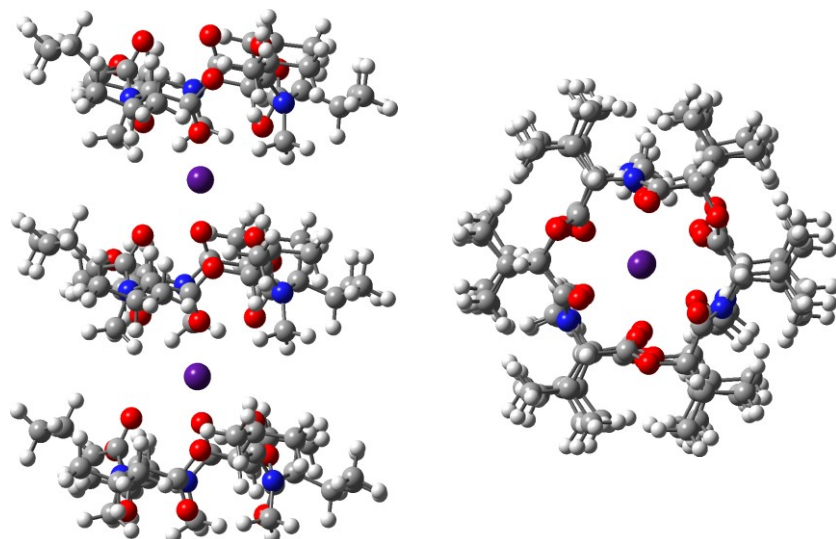


Figure A.5. Images of the top and side view of the EB structures obtained from the DFT calculation of the 3:2-AAEE complex with Cs^+ ion. Oxygen atoms are in red, nitrogen in blue, carbon in grey, hydrogen in white, and metal ion in purple.

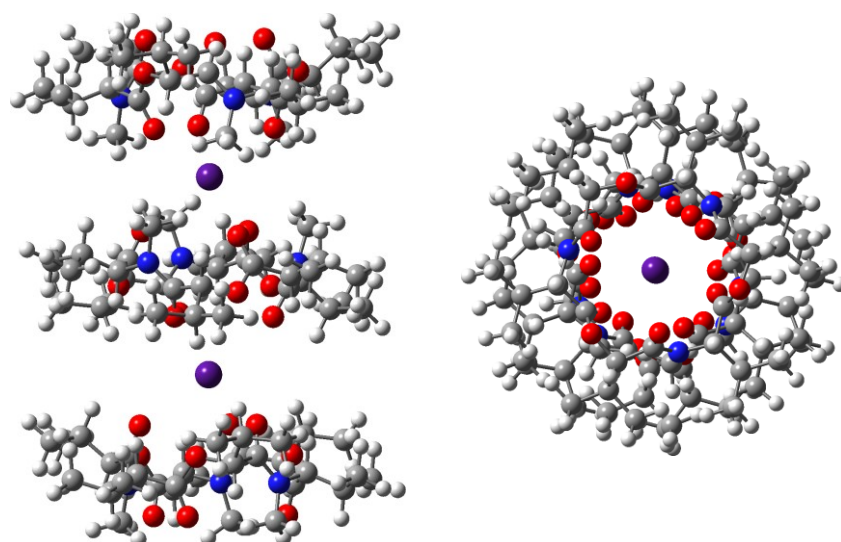


Figure A.6. Images of the top and side view of the EB structures obtained from the DFT calculation of the 3:2-AEAE complex with Cs^+ ion. Oxygen atoms are in red, nitrogen in blue, carbon in grey, hydrogen in white, and metal ion in purple.

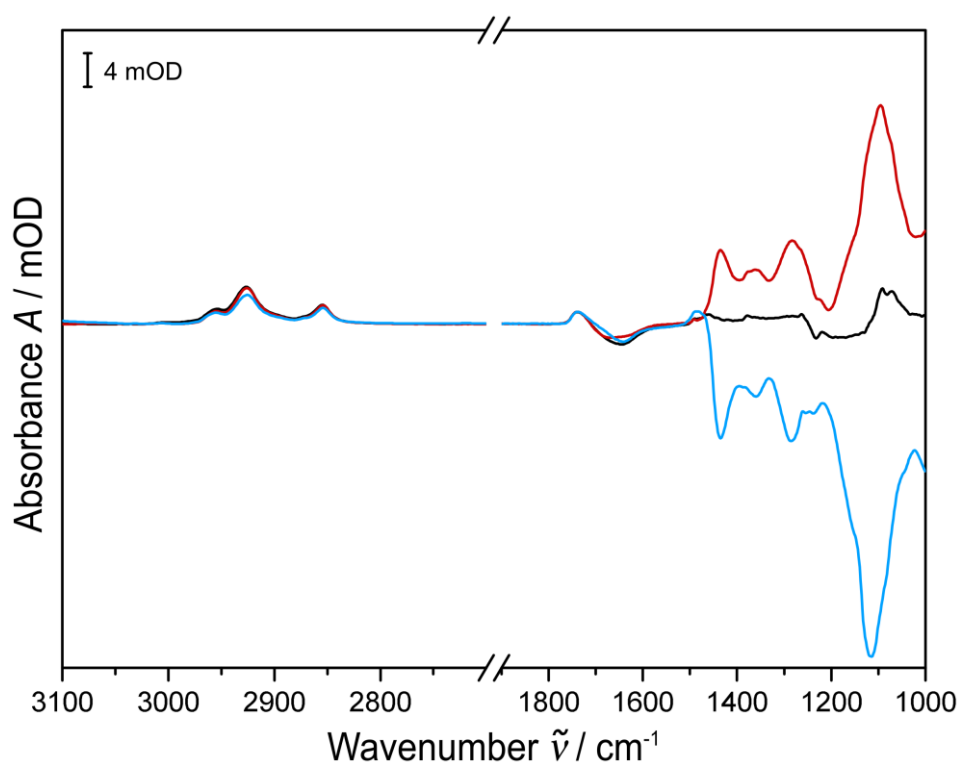


Figure A.7. SEIRA difference spectra of the POPC/POPG tBLM incubation at 4° C (blue), 25° C (black) and 37° C (red). The blue and red spectra depict the mirror temperature effect described in section 4.3.3.2.

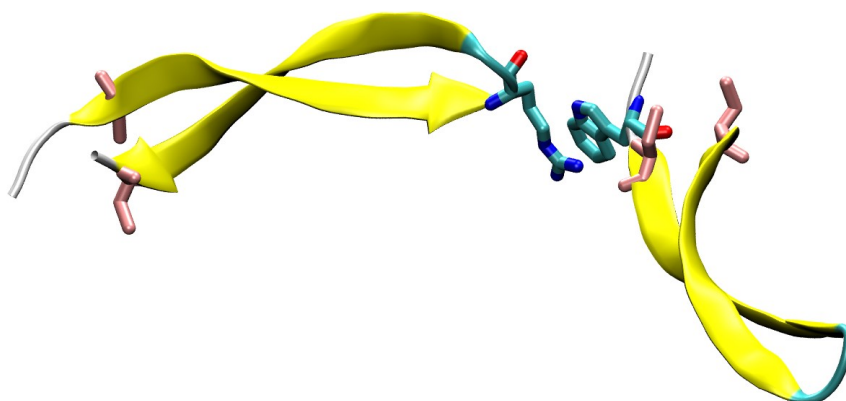


Figure A.8. Snapshot of 3D representation of two A1-analogue monomers after 300 ns of the dimerization MD simulation in solution. Yellow colour denotes the antiparallel β -sheet conformation while the β -turn is depicted in turquoise. The N- and C- terminal regions are unstructured represented in white colour. The Cys 3 and 20 are depicted in mauve colour. The random interaction between the Arg1 of one monomers and Trp21 of the other is depicted as well, where oxygen atoms are shown in red, nitrogen in blue and carbon in cyan colour. For matter of simplification, hydrogen atoms were omitted.

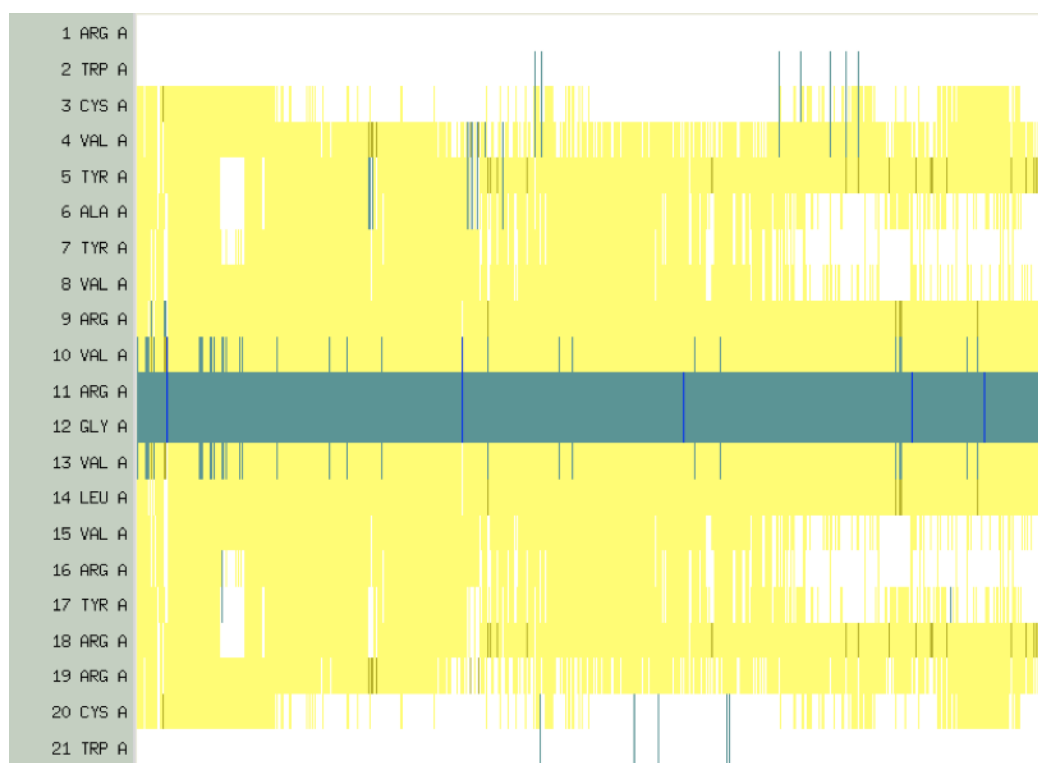


Figure A.9. Monitoring secondary structure plot of chain A (yellow A1 peptide in figure 4.44, section 4.3.4) of two A1 monomers interacting with the POPC/POPG membrane. Yellow colour denotes the antiparallel β -sheet conformation, while the β -turn is depicted in green and the coil in white. On the left side of the graph there is the amino acid sequence of A1 from the N- to the C-terminal, from top to bottom respectively.

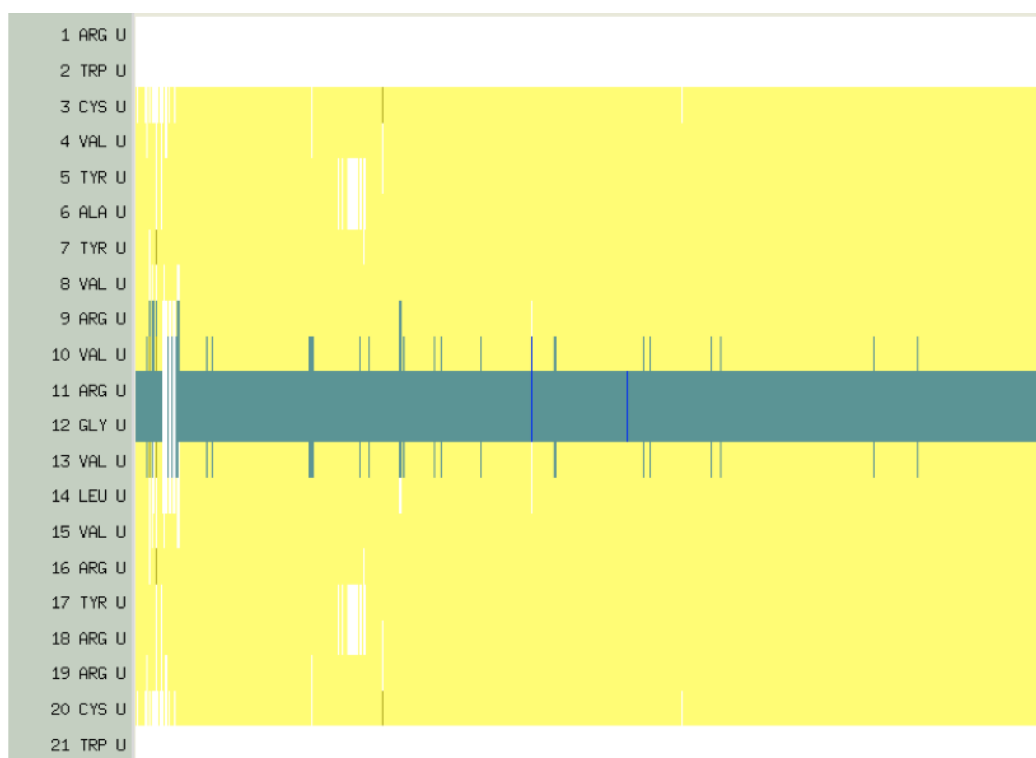


Figure A.10. Monitoring secondary structure plot of chain U (yellow A1 peptide in figure 4.44, section 4.3.4) of two A1 monomers interacting with the POPC/POPG membrane. Yellow colour denotes the antiparallel β -sheet conformation, while the β -turn is depicted in green and the coil in white. On the left side of the graph there is the amino acid sequence of A1 from the N- to the C-terminal, from top to bottom respectively.

Statement of Authorship

I hereby declare that I am the sole author of this doctoral thesis and I have not used any sources other than those listed in the bibliography and identified as references. I further declare that I have not submitted this thesis to any other institution in order to obtain a degree.

Barbara Daiana Gonzalez

Berlin, 31.07.2017

